POLITECNICO DI MILANO

Facoltà di Ingegneria Industriale

Corso di Laurea in
Ingegneria Energetica

EXPERIMENTAL AND NUMERICAL ANALYSIS OF CONFINED PARALLEL JETS

Relatore: Prof. Fabio INZOLI

Co-relatore: Ing. Riccardo MEREU

Tesi di Laurea di:

Samuele VIARO Matr. 724845

Anno Accademico 2011 - 2012.

"Thus I have explained to you
the most confidential of all knowledge.
Deliberate on this fully, and then
do what you wish to do."
Bhagavad-gita

Aknowledgments

When you are working in an environment surrounded by incredibly nice and collaborative people, as well as very talented, you can’t help but think that these few words will not suffice to express your appreciation to them.
I'd like to express my sincere gratitude to prof. F.Inzoli and prof. E.Colombo for the time they dedicated to me and the opportunity of being part of their research group. Out of all the brilliant members of their laboratory Ing. R.Mereu, who has been an amazing advisor, and Ing. P.Lampitella, a well-prepared doctoral student, deserve special thanks for their impeccable presence and the many things I learned from them.
Many thanks to prof. A.Coghe and prof. L.Araneo for their help and advice in the development of the experimental campaign.
During the time I spent at Tokyo Institute of Technology, prof. H.Ninokata and Ing. M.Pellegrini had been extremely nice to me, and for this I want to say thank you.

This thesis is dedicated to the people that mean the most to me in life: my Mother, Father, and Sister. To them I owe everything.

Index

List of Figures

List of Tables

Sommario

Accurate ricerche in campo fluidodinamico trovano sbocco in diversi settori scientifici e industriali che includono processi energetici ad efficienza migliorata, trasmissione del calore, combustione, problemi ambientali, sviluppi in medicina e studi della turbolenza. Quest'ultimo campo è di particolare interesse, in quanto miglioramenti nella conoscenza della sua fenomenologia hanno riscontri anche negli altri settori industriali e scientifici. Partendo da queste considerazioni, questa tesi si concentra nello studio di getti paralleli confinati, le cui applicazioni rientrano nei processi di ricerca sopra elencati, analizzando il campo fluidodinamico e i fenomeni di miscelamento attraverso una campagna sperimentale e uno studio numerico. L'apparato sperimentale utilizzato è stato sviluppato e realizzato al Politecnico di Milano ed è costituito da 5 tubi paralleli (diametro interno $D = 0.0212$ m) che si inseriscono in un plenum rettangolare (LxHxW: 0.545x0.05x0.165 m). Il fluido di lavoro è acqua a temperatura ambiente e il numero di Reynolds basato sul diametro interno dei tubi è $Re_D = 10^4$. Simulazioni numeriche tramite le Unsteady Reynolds Averaged Navier Stokes (URANS) e Large Eddy Simulation (LES) sono state realizzate con il software ANSYS FLUENT 12.1.2 con lo scopo di analizzare il fenomeno di miscelamento e identificare modelli di turbolenza appropriati per riprodurre correttamente il comportamento dei getti.
Un confronto tra le prove sperimentali (LDV) e i risultati numerici (URANS e LES) è stato effetuato per validare i modelli numerici e valutare le limitazioni dell'approccio URANS rispetto alla LES, la quale richiede risorse computazionali maggiori. Profili medi di velocità e sforzi turbolenti sono stati analizzati in differenti sezioni del plenum per avere un adeguato dettaglio utile a comprendere lo sviluppo di questo fenomeno e validare i modelli numerici.
Risultati sperimentali mostrano come il comportamento dei getti nella configurazione qui analizzata includa una serie di fenomeni che sono comuni nelle diverse trattazioni dei getti, attribuibili alle diverse forze in gioco presenti durante le interazioni getto-getto e getto-parete. Tra i risultati numerici, che in generale mostrano una sottostima dei profili di velocità e turbolenza, quelli che sono riusciti a predirre meglio il campo di moto sono i modelli non lineari. La LES invece, ha mostrato invece diverse inaccuratezze sia nei profili di velocità media che turbolenti, che verranno analizzate in studi futuri.

Parole chiave: Turbolenza, getti paralleli, URANS, LES, LDV.

Introduzione

Ricerche in campo fluidodinamico sono sfruttate in diversi settori scientifici. Nel campo stesso della fluidodinamica, la turbolenza si trova a tutt'oggi con domande ancora in cerca di spiegazioni concrete. Questi studi trovano sbocchi anche nella termofluidodinamica, dove gli scambi di calore convettivi sono associati alla natura del campo di moto, in fenomeni di combustione, tramite l'opportuno miscelamento di combustibile e comburente in bruciatori, processi chimici, distribuzione di particelle in un flusso, e altri sistemi energetici e non. La ricerca nell'ambito dei getti turbolenti trova applicazioni in un ampio campo di settori industriali, tra i quali ci sono quelli sopra citati. Le configurazioni esistenti sono ampiamente variabili: si parla di getti liberi o confinati, singoli o multipli, interazione getto-parete, influenza dei diversi parametri geometrici e fluidodinamici tra cui il numero di Reynolds (che nel caso di getti multipli può essere diverso da getto a getto), diametro idraulico dei getti e la loro distanza reciproca. Per un'analisi dettagliata dei vari parametri in gioco, approcci numerici e sperimentali vengono usati per colmare i relativi limiti. Risultati numerici possono essere estratti in qualunque punto del dominio analizzato, cosa che sarebbe improponibile fare con una facility sperimentale. Dall'altro lato, modelli numerici semplificati si appoggiano alla validazione sperimentale per essere considerati accurati. Basandosi su queste considerazioni, l'obbiettivo di questo lavoro di tesi comprende lo studio fluidodinamico, sperimentale e numerico, del comportamento di cinque getti paralleli confinati che interagiscono in un plenum rettangolare. Inoltre, i modelli numerici usati verranno analizzati per la loro validazione, utile per applicazioni ingegneristiche. La struttura sperimentale, progettata e montata nel laboratorio di combustione del Politecnico di Milano, viene usata per le misurazioni del campo di moto nel plenum tramite la tecnica Laser Doppler Velocimetry (LDV). Il dominio usato per l'analisi sperimentale, è stato poi discretizzato attraverso il software Gambit 2.4.6 e successivamente analizzato tramite il codice a volumi finiti ANSYS Fluent 12.1.2.

La turbolenza

La turbolenza è un fenomeno fluidodinamico interessato da fenomeni diffusivi e dissipativi con comportamento instazionario, casuale e tridimensionale. Rispetto al moto laminare, il moto turbolento è caratterizzato da fluttuazioni delle granzezze fisiche che causano un aumento dei fenomeni di miscelamento, scambio termico e dissipazione. Un fenomeno turbolento può essere distinto da un qualsiasi altro fenomeno casuale per la distribuzione di energia lungo

strutture coerenti di diverse dimensioni. Questa suddivisione in scale turbolente viene riassunta nella teoria di Kolmogorov: le grandi scale (scale integrali), aventi la dimensione caratteristica l_0 confrontabile con la dimensione della geometria considerata, ricevono energia dal campo di moto, la quale viene trasferita a scale intermedie (scale inerziali) fino a dissiparsi nelle piccole scale η (scale dissipative). Questa cascata di energia è riassunta nella Fig.(i.1).

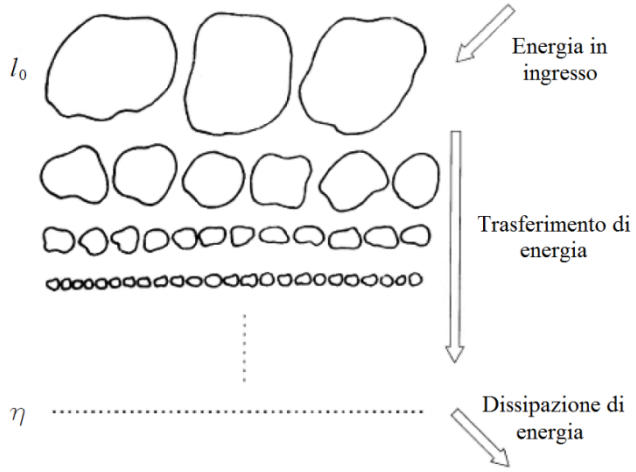

Figura i.1. Rappresentazione qualitativa della cascata energetica.

Un moto turbolento così rappresentato viene descritto dalle stesse equazioni che governano i flussi laminari, ovvero le equazioni di Navier-Stokes. Questo sistema di equazioni è costituito dalla conservazione della massa, quantità di moto e energia. Nel caso qui considerato, nel quale la trattazione è puramente fluidodinamica a densità costante, massa e quantità di moto, disaccoppiate dall'energia, vengono così espresse:

$$\frac{\partial u_j}{\partial x_j} = 0, \tag{i.1}$$

$$\rho\left(\frac{\partial u_i}{\partial t} + u_j \frac{\partial u_i}{\partial x_j}\right) = -\frac{\partial p}{\partial x_i} + \frac{\partial T_{ij}}{\partial x_j} \tag{i.2}$$

dove $u_i(\boldsymbol{x}, t)$ è a i-esima componente istantanea della velocità, $p(\boldsymbol{x}, t)$ la pressione statica e $T_{ij}(\boldsymbol{x}, t)$ il tensore degli sforzi viscosi.

Lo studio di grandezze casuali, quali quelle presenti in un flusso turbolento, trova una semplificazione nell'analisi statistica in cui media e varianza vengono calcolate. Usando la decomposizione di Reynolds, una generica variabile

istantanea può essere espressa in termini di una componente media A, e una fluttuante intorno alla media a':

$$a = A + a', \tag{i.3}$$

dove a rappresenta la generica variabile istantanea. Queste considerazioni vengono utilizzate sia in campo sperimentale che numerico, con il risultato di avere profili medi di velocità e varianza confrontabili tra loro.

Per quanto riguarda l'analisi sperimentale, lo strumento usato in questa tesi, LDV, è caratterizzato da un sistema non intrusivo per la misurazione puntuale della velocità in un campo di moto. Microparticelle costituite da una superficie riflessiva e con una densità prossima a quella del fluido di lavoro, vengono disseminate nel circuito. Una sorgente laser crea due fasci monocromatici aventi una certa lunghezza d'onda che intersecandosi danno origine ad un volume di controllo costituito da frange di interferenza (Fig.(i.2)).

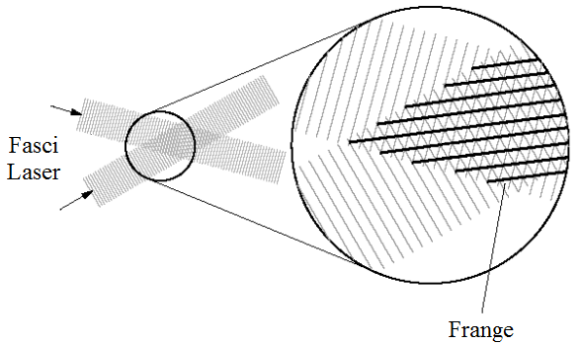

Figura i.2. Volume di controllo del sistema LDV.

Quando una paricella attraversa queste frange, trasmette una luce diffusa che viene catturata da un ricevitore ottico e trasformata in un segnale elettrico elaborabile da un calcolatore. Questo segnale contiene una frequenza f_D proporzionale alla velocità della particella tramite la relazione:

$$f_D = \frac{V}{\delta_f}, \tag{i.4}$$

dove V è la velocità della particella perpendicolare alle frange, e δ_f è la distanza tra le frange stesse. Le particelle campionate in un punto danno un'informazione sulla velocità istantanea che viene poi elaborata tramite l'analisi statistica precedentemente introdotta.

Nel caso invece dell'approccio numerico per uno studio fluidodinamico, è necessario risolvere le equazioni di Navier-Stokes. Se dovessimo discretizzare il

dominio cercando di catturare tutte le scale turbolente derivanti dalla teoria di Kolmogorov, ci vorrebbero un numero di punti nella griglia in quantità proporzionale a Re_L^3. Questo è quello che succede nella Direct Numerical Simulation (DNS) ma, intuitivamente, questo approccio è limitato a bassi numeri di Reynolds. Per ovviare a questo problema, sono stati creati dei modelli numerici con lo scopo di ridurre le risorse computazionali e i tempi di calcolo a livelli accettabili per applicazioni industriali. Una prima riduzione, viene introdotta con l'uso della Large Eddy Simulation (LES), un approccio numerico che invece di simulare direttamente tutte le scale della turbolenza, simula solo quelle a più alto contenuto energetico, e usa dei modelli per valutare l'influenza delle piccole scale, ritenute isotrope. La suddivisione delle scale viene fatta attraverso un'operazione di filtraggio delle variabili, che consente di separare la generica grandezza a nel seguente modo:

$$a = \bar{a} + a^*, \tag{i.5}$$

dove $\bar{a}$ è la grandezza filtrata attraverso opportune funzioni, e a^* è la grandezza residua. Applicando l'Eq.(i.5) alle Eq.(i.1) e Eq.(i.2) otteniamo un sistema di equazioni filtrate:

$$\frac{\partial \bar{u}_i}{\partial x_i} = 0 \tag{i.6}$$

$$\frac{\partial \bar{u}_i}{\partial t} + \bar{u}_j \frac{\partial \bar{u}_i}{\partial x_j} = -\frac{1}{\rho}\frac{\partial \bar{p}}{\partial x_i} + \nu \frac{\partial}{\partial x_j}\left(\frac{\partial \bar{u}_i}{\partial x_j} + \frac{\partial \bar{u}_j}{\partial x_i}\right) - \frac{\partial \tau_{ij}^R}{\partial x_j} \tag{i.7}$$

Con questo approccio, sono possibili analisi di tipo statistico del campo di moto e quindi uno studio non solo dei parametri medi ma anche istantanei.
Volendo ulteriormente ridurre i tempi di calcolo, si passa all'approccio Unsteady Reynolds Average Navier Stokes (URANS), con il quale la turbolenza viene interamente modellizzata. Questo viene fatto applicando Eq.(i.3) alle Eq.(i.1) e Eq.(i.2), e risolvendo il sistema di variabili mediate che ne segue:

$$\frac{\partial U_j}{\partial x_j} = 0, \tag{i.8}$$

$$\rho\left(\frac{\partial U_i}{\partial t} + U_j \frac{\partial U_i}{\partial x_j}\right) = -\frac{\partial P}{\partial x_i} + \frac{\partial}{\partial x_j}\left(\mu \frac{\partial U_i}{\partial x_j} - \rho\langle u_i' u_j' \rangle\right). \tag{i.9}$$

In questo caso però, solo le grandezze medie sono derivabili, e i tempi di calcolo molto ridotti, rendendo le URANS molto promettenti dal punto di vista ingegneristico. Questi ultimi due approcci, LES e URANS, sono quelli usati in questa tesi per lo studio dei getti e validazione dei modelli turbolenti. In particolare, nel caso LES le piccole scale vengono modellate tramite il modello Smagorinsky, mentre nel caso URANS vengono usati i seguenti modelli presenti nel codice commerciale in uso: $k\varepsilon$ Standard, $k\varepsilon$ RNG, $k\varepsilon$ Realizable, $k\omega$ SST, e RSM. Inoltre un modello non lineare implementato dal CFDLab del Politecnico di Milano, è stato usato.

Apparato sperimentale e dominio numerico

Il dominio analizzato è costituito da una configurazione di cinque getti paralleli molto vicini tra loro, che espandono in un plenum rettangolare. La geometria selezionata per questo studio è stata ideata per un'analisi di getti paralleli nei quali le loro interazioni reciproche non portano ad una deformazione dei getti stessi. L'idea è quella di bilanciare le varie forze che potrebbero far deviare i getti, ovvero mutua interazione e presenza di una parete, per fare in modo che i tre getti centrali, o per lo meno il getto centrale, possano essere studiati come se idealmente fossero in una configurazione infinita di getti. Questo tipo di configurazione può essere applicata in situazioni in cui getti paralleli espandono in un dominio anulare. Il disegno CAD mostrato in Fig.(i.3) riassume i dettagli della sezione di indagine, con l'origine degli assi posizionata all'ingresso del plenum sull'asse del condotto centrale, e misure espresse in metri.

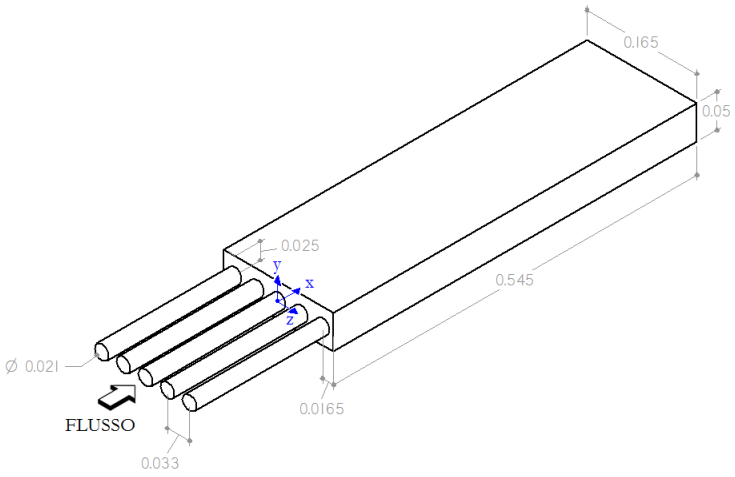

Figura i.3. Dettagli geometrici del plenum e condotti circolari.

Lo stesso dominio è stato poi discretizzato e usato per le simulazioni numeriche. La mesh usata per le simulazioni URANS deriva da un'analisi dell'Indice di Convergenza della Griglia (GCI) valutato su griglie con tre diversi infittimenti, riportati in Tab.(i.1).

Griglia	***Indice***	***Numero celle***
Fine	1	$2.27\ 10^5$
Media	2	$1.27\ 10^5$
Lasca	3	$7.07\ 10^4$

Tabella i.1. Parametri relativi alle griglie usate per l'analisi GCI.

Confermato che la soluzione rientra nel range asintotico di convergenza, la griglia media è stata selezionata per le prove numeriche URANS. Per quanto riguarda la griglia usata per la LES, sono stati usati dei parametri, mostrati nella Tab.(i.2), considerati accurati per rappresentare diverse configurazioni.

Parametri adimensionalizzati	***Formula***	***Valore Limite***
Δx^+	$\frac{\Delta x}{D} Re_\tau$	$< 50 \div 100$
$\Delta \vartheta^+$	$\frac{\pi}{N} Re_\tau$	$< 15 \div 45$
Δy^+	$\frac{u_\tau (D/2 - r)}{D} Re_\tau$	< 1

Tabella i.2. Parametri relativi alla griglia LES.

Questi parametri, calcolati per i tubi, sono stati rispettati in tutto il dominio, con un lieve infittimento nella zona di interazione dei getti. L'obbiettivo della validazione dei modelli numerici è quello di poter riuscire a sfruttarli in seguito per analizzare configurazioni di getti simili per le quali le prove sperimentali sarebbero troppo complicate, come nel caso del dominio anulare.

Per concludere con la descrizione delle prove e simulazioni fatte, viene riportata di seguito una tabella indicante i dati fisici durante le prove sperimentali.

Proprietà	***Valore***	***Unità [SI]***
Re_D	10^4	$[-]$
p	101325	[Pa]

T	293,15	[K]
ρ	998	[kg m^{-3}]
μ	0.00101	[Pa s]

Tabella i.3. Caratteristiche del flusso considerato.

Questi dati sono stati poi riportati nel codice per le simulazioni numeriche.

Risultati ottenuti

Dall'analisi dei profili sperimentali risulta che la geometria studiata si avvicini molto ad un caso in cui i getti espandono senza eccessivi spostamenti. É da notare però che una leggera deviazione dei getti è presente: i tre getti centrali tendono ad avvicinarsi, mentre i due vicini alle pareti laterali rimangono separati dagli altri. La Fig.(i.4) mostra i profili della velocità U_x lungo l'asse z adimensionalizzato per la larghezza del plenum W (sinistra) e l'ungo l'asse y adimensionalizzato per l'altezza del plenum H (destra).

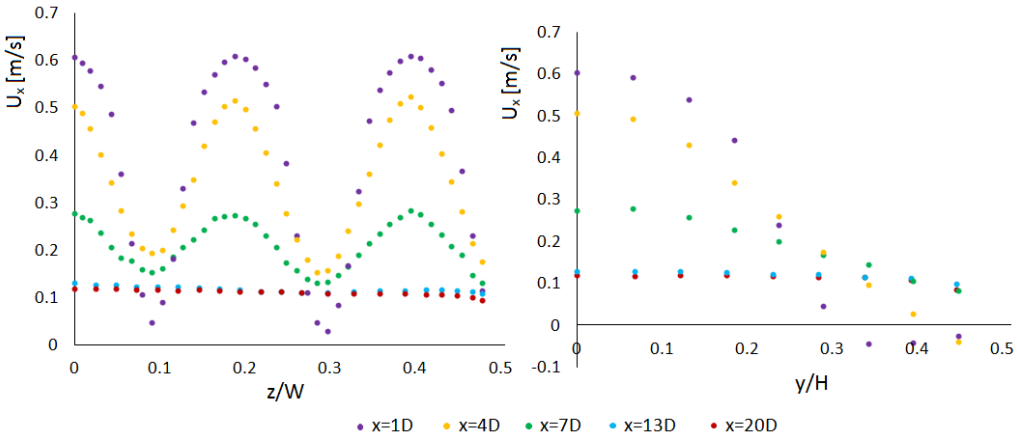

Figura i.4. Profili sperimentali della velocità media U_x lungo l'asse z e y.

Si nota dai risultati come i getti siano talmente ravvivinati che a $x = 1D$ le zone di ricircolo tra uno e l'altro, se in questo piano esistessero, sarebbero confinate molto vicine alla sezione d'ingresso. Zone di ricircolo, causate dal fenomeno dell' entrainment, sono invece presenti lungo l'asse y e il conseguente vortice formato si estingue a $x \approx 6D$. Da notare come una volta terminata l'influenza del vortice, i getti espandono velocemente con una forte riduzione dei picchi di velocità.

Nella predizione di questo tipo di geometria, la Large Eddy Simulation si è rivelata inconsistente in certe zone con i risultati sperimenali. Per quanto riguarda i profili di velocità media, queste zone sono limitate nell'intorno della regione $x = 7D$, dove avviene la maggior espansione dei getti. La turbolenza invece, se è rivelata essere di accuratezza decrescente andando dall'ingresso dei getti, dove troviamo una buona affinità con i dati sperimentali, fino all'ultima sezione analizzata. In generale i risultati LES dimostrano avere un comportamento di sottostima, e quindi una maggiore diffusione.

I risultati numerici URANS sono ovviamente dipendenti dal tipo di modello turbolento usato. Nel caso della famiglia di modelli $k\varepsilon$ i risultati mostrano una generale sottostima dei profili medi di velocità per il Realizable e Standard, soprattutto nella zona principale di espansione ($x = 4D, x = 7D$), mentre con l'RNG nascono delle instabilità nel campo di moto ritenute non fisiche. Dall'altro lato, il modello $k\omega$ SST, dimostrato essere il più accurato per la riproduzione del campo di moto nei tubi circolari, mostra una generale sovrastima dei risultati. Risutlati migliori si ottengono con modelli meno restrittivi dal punto di vista delle semplificazioni numeriche. In particolare il modello non lineare, con una particolare funzione di damping, è risultato essere il migliore nel predirre l'interazione dei getti. Nel caso invece del modello RSM, anche se in generale migliore dei modelli lineari e con buoni risultati nei profili turbolenti, l'accuratezza nella predizione dei profili medi di velocità risulta essere inferiore al modello non lineare. Un riscontro negativo nell'uso del modello non lineare per la predizione di geometrie simili viene trovato nell'aumento dei tempi di calcolo, fino a 10 volte maggiori, rispetto agli altri modelli.

Abstract

Fluid dynamics is an interdisciplinary field whose researches touch several scientific and industrial sectors including high-efficiency energetic processes, heat transfer, combustion, environmental problems, health, and turbulence. This last field is of particular interest, since improvements in the knowledge of its phenomenology are indeed useful in the other fields of study.
Starting from these considerations, the present thesis is focused on the study of parallel confined jets, whose applications encompass the research projects mentioned above, in order to analyze the flow field and mixing phenomena via an experimental campaign and numerical studies. The experimental facility, designed and assembled at Politecnico di Milano, is composed of 5 parallel pipes (internal diameter $D = 0.0212$ m) issuing into a rectangular plenum (LxHxW: 0.545x0.05x0.165 m). The working fluid is water and the Reynolds number based on the internal pipe diameter is $Re_D = 10^4$. Numerical simulations via Unsteady Reynolds Averaged Navier Stokes (URANS) and Large Eddy Simulation (LES) were performed with the software ANSYS FLUENT 12.1.2 in order to analyze the mixing phenomenon and identify appropriate turbulence models for a correct reproduction of the parallel confined jets behavior. A comparison between experimental measurements (LDV) and numerical data (URANS and LES) was executed to validate the numerical results as well as evaluate the limitations of the URANS approach with respect to the more computationally expensive LES method. Mean velocity profiles and turbulence properties are analyzed at different locations of the plenum in order to have enough details to truly comprehend the development of this phenomenon and validate the numerical models.
Experimental results show a series of common phenomena found in other jets configurations, attributable to the forces deriving from the jet-to-jet and jet-to-wall interactions. Among the numerical results, that globally show an underestimation of mean velocity and turbulence profiles, the non linear models were found to better represent the flow field under study. Inaccuracies in both mean velocity and turbulence profiles are also present when LES was used for the prediction of the flow, and further studies are being conducted for the analysis of this behavior.

Keywords: Turbulence, Parallel jets, URANS, LES, LDV.

Introduction

The practical relevance of jets in engineering is spread in many fields ranging from energy to medical applications. Examples may be found in temperature, fuel dilution and stability analysis of a furnace burners [1], annular configuration of a nuclear reactor downcomer [2], cooling systems [3, 4], heat transfer [5] or even in cardiovascular studies of blood flows [6, 7]. Giving the variety of geometrical configurations that might arise from the design of engineering components and the requirement of different fluid dynamic conditions, computational, experimental and analytical researches regarding turbulent jets are still important to perform. Computational Fluid Dynamics (CFD) and experimental approaches, in particular, are often used together to investigate the behavior and physics of fluids in a broad variety of situations, parallel confined jets being one of them. Test facilities cannot be easily reproduced for every case, and measurements are sometimes not possible to obtain in areas hardly accessible to the instruments. The advantage of numerics is this sense, is the possibility to analyze complex geometries in every region of the domain. On the other hand, numerical analyses are often carried on using simplified, yet accurate, models that reduce the computational resources necessary for the simulations. These simplifications, tested in specific configurations, are validated with the help of experimental data. The continuous advancement of technology has improved the range of applicability, accuracy and efficiency in both cases, especially in computational analysis where the exponential advancement of computer capabilities allows the use of more sophisticated models with improved predicting capabilities.

Despite their wide usage in industrial applications, parallel confined jets have not been studied as much as, for example, singular jets. The mixing and interaction of jets along with the presence of a confinement, increase the complexity of the phenomenon and therefore a thorough investigation requires both experimental and numerical data. Several works have been realized during the last years, giving us an insight about confinement and interaction of jets. The analysis of the behavior of jets begins from the simplest case of one jet. Let us consider its basic principles [8]. A jet of fluid is defined as free if it both issues into a reservoir of the same fluid without any wall influence and has a cross-sectional area one-fifth of the confinement, otherwise it is a confined jet. We can see in Fig.(I.1) the two main regions that characterize a jet: the core, or potential core, and the shear layer. Into the core, the velocity remains unchanged with a value of U_0. Moving away from the orifice, the turbulent shear layer consumes the core in the same manner that a boundary layer shrinks the inviscid flow region in the case of a fluid entering a duct with uniform velocity. The total consumption distance of the core, the initial length, can be estimated

approximately to five diameters, a number that can change as a function of the turbulent shear layer intensity.

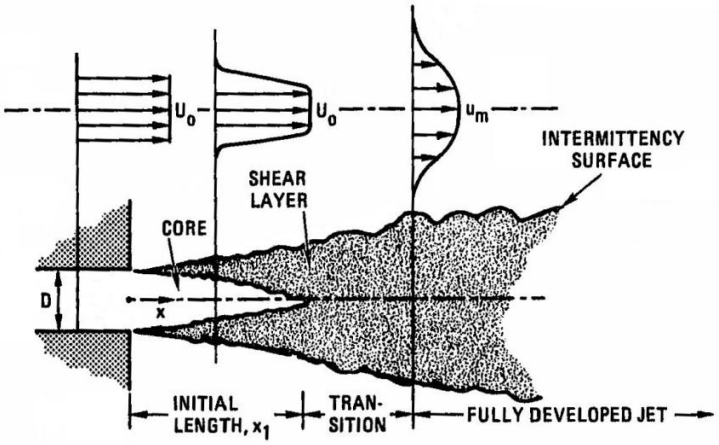

Figure I.1. Schematics of a turbulent jet [9].

As a jet flows away from a slot it draws in fluid from the surrounding mass, causing the mass of fluid carried along by the jet to increase, a phenomenon called entrainment, Fig.(I.2).

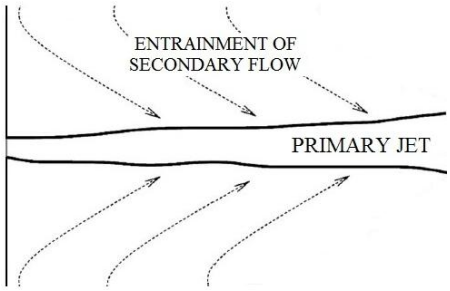

Figure I.2. Entrainment effect.

Viscous effects are the source of this phenomenon, and the result is that since the centerline velocity passed the core region decreases, and the mass of the jet increases, there is a conservation of axial momentum, hence pressure remains constant.

In the case of two parallel jets, entrainment plays a major role. When the jets expand, they are both trying to carry along particles from the area between them, and by doing so they create a subatmospheric pressure region that sucks the jets in and makes them combine after a certain length from the origin [10]. The results of this is the creation of two counter rotating vortexes in what it is named: recirculation zone, Fig.(I.3). The interaction between jets was

experimentally proved to act as a booster of instabilities which were found to be a function of jet spacing and momentum ratio [11]. In particular, the periodic flapping of the jets peaks when they have the same momentum, and stability is shown if one of the two jets has a momentum at least thrice as high as the other, in which case the stronger jet entrains the weaker. In addition, comparing the results of two experiments [11, 12] it is possible to assume that a maximum frequency and minimum amplitude of the oscillations is reached for $s/a \approx 4$, where s is the distance between jets centerlines and a is the jet's width. Jet spacing and momentum are the two parameters that could be used to increase or reduce the mixing of the jets, whereas the Reynolds number was proven to be uninfluential [13].

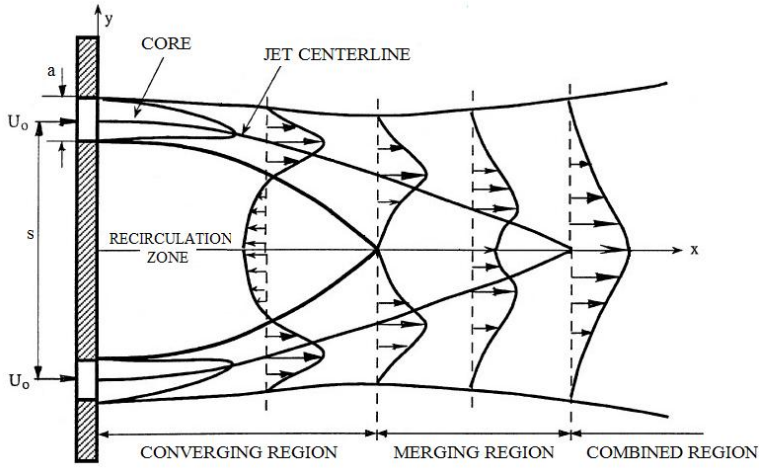

Figure I.3. Schematics of two parallel turbulent free jets [14].

As for the case of a single free jet, the development of two parallel free jets can be distinguished in regions (Fig.(I.3)) that indeed experience different characteristics as we move along the *x* axis [14, 15]. First, the converging region experiences a subatmospheric pressure (recirculation zone), negative streamwise velocities and low turbulence. Once the merging region is reached, the interaction of the inner shear layers causes a pressure increase to superatmospheric values, streamwise velocities becomes positive and turbulence peaks. Finally, after the mixing has occurred in the merging region, the jets start to resemble the behavior of a single jet, with wider but lower velocity profiles, at the beginning of the combined region.

As previously stated, two jets having the same momentum create an instable, fluctuating flow field. If one more jet, with the same flow properties as the others, is introduced in the recirculation region, its influence prevents the instabilities from happening [16]. More precisely, when $0.707 < U_{os}/U_{oc} <$

1.1 results show that the central jet is entrained by the lateral jets as depicted in Fig.(I.4b). With velocity ratios lower than 0.707 the configuration is still stable, but in this case the central jet is more energetic and entrains the others. On the other hand, increasing the momentum of the lateral jets leads to an asymmetric flow pattern which is governed by the lateral jets themselves. Instabilities were found even in this configuration of three parallel jets in the range of $U_{os}/U_{oc} \approx 1.15$, with alternative motion of the flow and high noise.

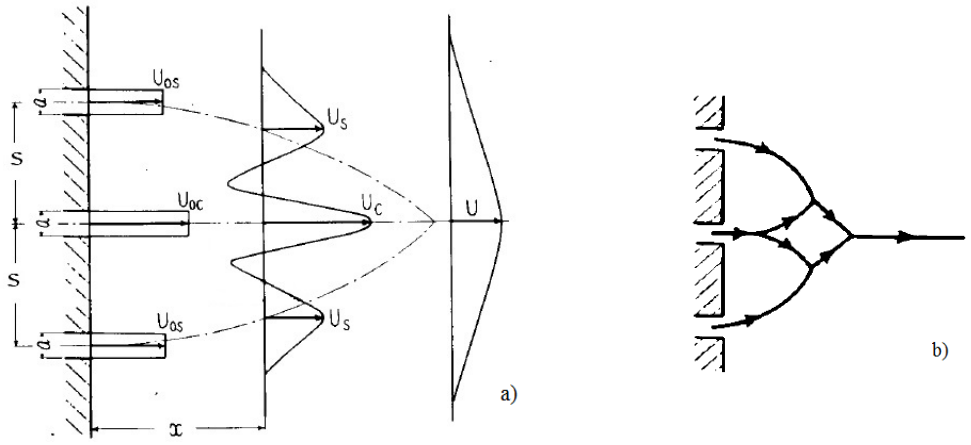

Figure I.4 Schematics of three parallel turbulent free jets [16].

Considering the case of similar momentum of the jets, Fig.(I.4a) shows qualitatively that we can still find recirculation regions between the jets and, at a far enough distance from the inlet, the three jets merge and form a velocity profile that once again resembles the one free jet configuration.

Before proceeding to the case of confined parallel jets, it is worth spending few words in regard of the interference of a fluid with a confining wall. Let us consider the case of one jet. As in the case of an undisturbed reservoir, jets tend to expand moderately, and unless there is a gradual constriction that follows their growth, recirculation occurs undoubtedly before the flow reconstitutes downstream of the reattachment (Fig.(I.5)). The reasons of this behavior are mainly two. Among the particles that enter the confinement, there are several of them, the ones present in the center of the jet, that can make it through the adverse pressure gradient and continue their trajectory without being strongly influenced; however, particles coming from the region near the walls, are much less energetic and forced by the pressure gradient to move backwards into a low-pressure vortex region. The cause of this low-pressure area can, once again, be attributable to entrainment of fluid particles present between the jet and the confining wall.

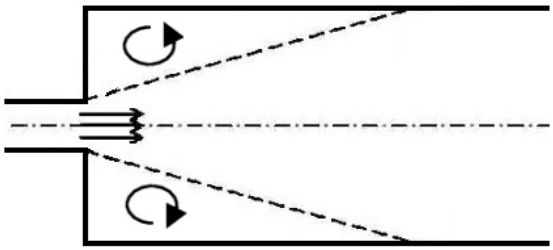

Figure I.5. Schematics of a confined turbulent jet.

If only one wall is present when a jet expands, the decrease of pressure near the wall can cause the jet to stick to the wall, an effect known as Coanda effect (Fig.(I.6)). Experiments demonstrate that, the further away the wall is from the jet entrance, the bigger the vortex near the wall and the longer the reattachment length are [17].

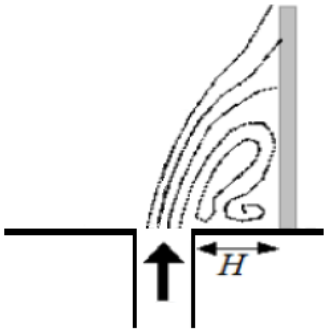

Figure I.6. Coanda effect.

The physical characteristics of jets that were previously discussed are a useful basic knowledge when investigating configurations with multiple jets interacting both with each other and also with the walls of the confinement in which they expand. These interactions are globally studied via experimental data. In addition, numerical models that can accurately predict the behavior of turbulent jets are also important when studying these phenomena, especially considering that not all the regions of an experimental facility can be analyzed

A first class of modelling approach that is widely used in industrial applications due to its low computational requirement, stability and accuracy in a variety of situations is the Reynolds Averaged Navier Stokes (RANS) approach, whose dependence on constants for the closure of the equations influences its general applicability. In this matter, the two-equation k-ε model was proved to possess an anomaly in representing the behavior of one free jet when compared with experimental data. In particular, numerical results are opposite to experimental ones when analyzing both the spreading difference

between plane and round jets [18], and the effect of initial conditions for round jets [19]. In the multiple jets configurations, several models were also studied. Qualitative agreement of the results were reached when investigating the frequency, velocity profiles and Schlieren images [20] in one case, and the merging length, decay rate and spreading rate in another case [14] for a two plane jets configurations using the Unsteady Reynolds Averaged Navier Stokes (URANS) approach. However, results lack in quantitative agreement, especially for the latter case, in which discrepancies for turbulent quantities are up to 50 percent. When jets are confined, the symmetry of the geometry does not imply that symmetric boundary conditions could lead to accurate results. In a study of five confined jets, two-equation models underpredicted the spreading ratio when only one fourth of the jet was numerically investigated with three planes of symmetry [21]. The same case analyzed with one jet bounded with lateral periodic conditions was able to improve the results in the spreading ratio and velocity profiles [20]. In the same study, due to the non stationary nature of the flow, results are shown to improve using the URANS instead of the RANS approach.

The next step toward an increase of accuracy and, as a backfire, computational expense is represented by the Large Eddy Simulation (LES). The fact that only the small scales of motion are modelled, helps in the prediction of the rapid transverse mixing, anisotropic behavior and presence of secondary flows that is typical of parallel jet domains. A proof of this statement lies with an good agreement with the results, when the five confined jets mentioned earlier were investigated via LES [22]. In addition, even when temperature fluctuations, along with the fluid dynamics, were studied in a three-jet configuration, LES demonstrated its ability in predicting these flows, when compared to experimental data [23].

Finally, by solving all the scales of motion through a Direct Numerical Simulation (DNS) of the governing equations, a thorough comprehension of the physics of jets, such as the entrainment phenomenon [24], is possible. However, this approach is limited to low Reynolds number flows, due to its high requirement in terms of computational needs.

Motivation

When multiple parallel jets expand into a confinement, their mutual interaction and the wall influence generate a complex fluid dynamics characterized by secondary motions, anisotropy, pressure gradients, fluid separation and recirculation. As previously mentioned, the multitude of engineering applications that rely on the characteristics of this kind of flows is what motivated researchers to a better understanding of these phenomena on one side,

and the implementation of numerical models that could accurately predict them on the other. Based on these considerations, the purposes of this thesis are focused on the:

- Experimental and numerical investigation of the behavior of parallel confined jets;
- Validation of numerical models.

In order to properly achieve these two objectives, the design and construction of an experimental facility was realized in the combustion laboratory at Politecnico di Milano. Five parallel jets issuing into a rectangular plenum are analyzed with the Laser Doppler Velocimetry (LDV) approach, a non intrusive technique that can punctually measure the instantaneous velocities of a flow field. This technique is widely used for its precision in fluid dynamics and validation of numerical methods via comparison of mean velocity and Root Mean Squared (RMS) turbulent profiles.

The domain investigated experimentally, is then reproduced using the Gambit 2.4.6 mesh generator and subsequently analyzed with the commercial finite volume code ANSYS Fluent 12.1.2. The numerical models tested can be mainly categorized as follows:

- Unsteady Reynolds Averaged Navier Stokes (URANS)
  - Linear Eddy Viscosity Models (LEVM)
  - Non Linear Eddy Viscosity Models (NLEVM)
- Large Eddy Simulation (LES)

The first kind of models is the most common for industrial purposes due to their numerical stability, fair accuracy and minimum computational requirements for a variety of applications. Even though limitations of the LEVM for complex flows are well recognized, knowing how well they predict parallel confined jets and if they can fairly represent at least mean quantities, which is usually the requirement for the design and implementation of industrial projects, is important in terms of time saving and as a first analysis of the domain under investigation. Moving to the NLEVM is a step forward to an improvement of accuracy. The non linear formulation of the Reynolds stress tensor can better capture the secondary structures of flows with a relatively small increment of the computational expenses. The models used for this matter were implemented by the CFDLab at Politecnico di Milano. The use of LES for certain industrial applications might be excessive in several occasions due to its higher computational need with respect to the URANS models. However, it is surely required when the phenomena are to be analyzed in depth since the most influential scales of motion are modelled, hence higher degree of accuracy with

respect of the models previously discussed. It is also worth mentioning that the exponential increase of computer speed renders LES a more and more available tool even for industries. The validation of the LES is then an essential part of this thesis for both industrial purposes and a more accurate analysis of the behavior of parallel jets.

Thesis Structure

The present work is structured in four main parts that focus on the parameters mentioned earlier.
Chapter One, is a brief introduction of the turbulence phenomenology, pointing out its nature, equations and how to analyze it.
Chapter Two describes the experimental facility, along with the instrumentation used for the fluid dynamics investigation.
Chapter Three specifies the numerical methodology. Mesh properties and numerical settings for each numerical model are here present.
Chapter Four illustrates and compares experimental and numerical results.
Finally, conclusions on the results are drawn and future investigations discussed.

Chapter 1

Analyzing Turbulence

Working hypothesis. This is the term used by professor William K. George [25] to describe our real knowledge about this intricate subject. We live in a renaissance age for turbulence, in which technology is playing a big role in helping untapping the true physics behind this phenomenon. Engineeringly speaking, we have to make the best out of our current knowledge in order to fulfill the demands of societies: drag reduction for vehicles, cleaner combustion processes, efficient heat exchangers, and so on. This chapter briefly summarizes what are the basic "tools" for studying turbulence, and applying it to industrial problems.

1.1 Turbulence in a nutshell

Nature is characterized by a variety of phenomena that have triggered humans' attention since the classical era, where natural philosophers started to investigate its innate qualities. Turbulence is certainly one of them, with its boundless variety of artistic forms ranging from the water in a cascade to the wingtip vortexes of an airplane.

Figure 1.1. Leonardo Da Vinci's observation of turbulent flows.

The first man to investigate these phenomena can be dated back to the 16th century, when Leonardo Da Vinci drew, with impressive details (Fig.(1.1)), several sketches of flow situations that provide the earliest reference of vortexes, eddies of different sizes and random motion. Great minds have studied this subject and stunning progresses have been made but 600 years after that first drawing, turbulence still remains one of the unsolved mysteries of nature.

Observing a waterfall, one can immediately notice the obvious unpredictable motion of the droplets and eddies characterizing the flow. This stochastic, chaotic and three dimensional behavior, that leads to an irregular time and space dependent velocity field, is what lies behind turbulence. For a better understanding, let us take a look at Fig.(1.2) which can be recognized as the Reynolds experiment.

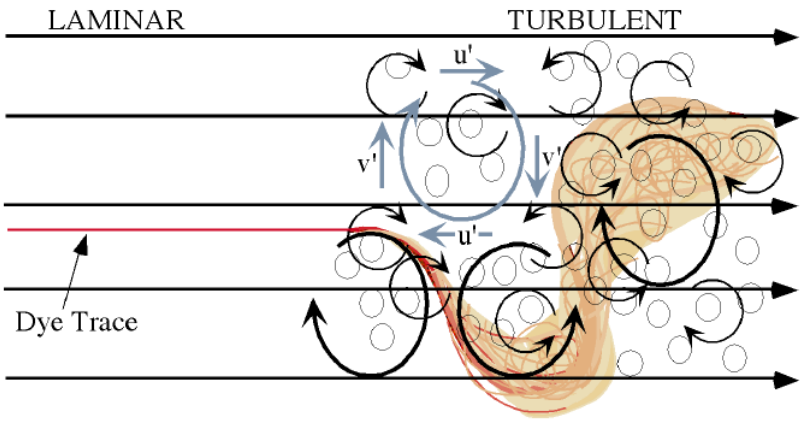

Figure 1.2. Trace transport in laminar and turbulent flow .

The above figure plainly highlights how eddies play a major role in moving around fluid particles that in a laminar flow would simply follow the streamlines as the red dye trace does. Large eddies are responsible for carrying the dye trace laterally across streamlines, while small ones create smaller scale stirring that cause the filament to diffuse. As a result, random fluctuations of the velocity field are present, causing an increase of energy dissipation as well as mixing and heat transfer enhancement.

1.1.1 Decomposing turbulence

Let us consider a simple experiment. If we want to drink a *caffè macchiato*, we add cream, grab a spoon and stir. The vortexes that we create by moving the spoon, easily noticeable, break down in to smaller and smaller vortexes that

enhance mixing and disperse the milk into the coffee, much as the red dye does when "entering" the turbulent zone in Fig.(1.2). This simple picture, plainly depicts Richardson's view of the energy cascade (1922): energy, stirring, from the large scales of motion, vortexes from the spoon, is transferred to smaller and smaller scales until finally it transforms into internal energy. The instability of the large scales is the cause of their subsequent shuttering into smaller structures that, once stable, are easily dissipated by viscosity.

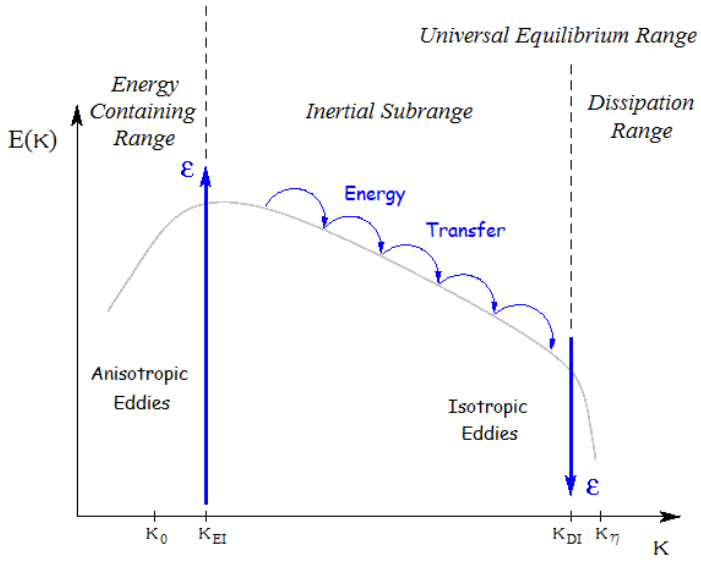

Figure 1.3. Energy flow along the turbulent scales.

This energy cascade notion was later improved by Kolmogorov in 1941, whose hypotheses, based under the assumption of a very high Reynolds flow, can be summarized by looking at the turbulent energy spectrum of Fig.(1.3), in which the wavenumber is defined as $\kappa = \frac{2\pi}{l}$. In a turbulent flow with characteristic velocity V and length L, eddies of various characteristic sizes l, velocity u_l, and timescale τ_l are present. These turbulence scales, based on energy terms, possess the following properties [26]:

- *Energy Containing Range* ($\kappa < \kappa_{EI}$): large scales are anisotropic and characterized by a size $l_0 \approx L$ and velocity $u_0 \approx V$, which is on the same order of the root mean square of turbulence intensity.
- *Inertial Subrange* ($\kappa_{EI} < \kappa < \kappa_{DI}$): through the scale reduction process, the direction bias is lost and eddies become statistically isotropic. Viscous effects are negligible and the energy spectrum is a function of

the energy transfer rate ε only, which remains constant through the entre range.

- *Dissipation Range* ($\kappa > \kappa_{DI}$): when the size of the scales is small enough, so that their Reynolds number approaches unity, viscous effects transform kinetic energy into internal energy.

The scale reduction process also causes the information about the geometry to be lost, leaving the *Universal Equilibrium Range* a function of ε and ν only. By these considerations the small scales, or Kolmogorov's small scales, are defined as:

$$\eta \equiv \left(\frac{\nu^3}{\varepsilon}\right)^{1/4}; \qquad u_\eta \equiv (\varepsilon\nu)^{1/4}; \qquad \tau_\eta \equiv \sqrt{\frac{\nu}{\varepsilon}}. \qquad (1.1)$$

From the characteristic velocity and length scale of the eddies, the rate at which energy is transferred is proportional to:

$$\varepsilon \sim \frac{u_0^3}{l_0}. \qquad (1.2)$$

Eq.(1.1) and Eq.(1.2) lead to a definition of the small scales of turbulence as a function of the Reynolds number of the flow considered:

$$\frac{\eta}{l_0} \approx Re^{-3/4}; \qquad \frac{u_\eta}{u_0} \approx Re^{-1/4}; \qquad \frac{\tau_\eta}{\tau_0} \approx Re^{-1/2}. \qquad (1.3)$$

At high Reynolds numbers, which is the case for many industrial applications, the ratio between small and large scales is quite large, which means that the small scales of motion are very small compared to the characteristic dimension of the geometry.

Even though Kolmogorov hypotheses complete the picture of the turbulent scales, it is important to remember that thus far, there hasn't been the possibility to prove these theories neither experimentally nor numerically.

1.1.2 Governing equations

When only macroscopic properties are at interest, the fluid can be treated as a continuum. Under this assumption, and for Newtonian fluids, a flow system is governed by the Navier Stokes Equations (NSE). By solving this mathematical model of unsteady equations, all the space-time scales of a real phenomenon are taken into consideration. Limiting our analysis to a density constant fluid, which

is the case studied in this thesis, these conservation equations are expressed as follows:

$$\frac{\partial u_j}{\partial x_j} = 0, \tag{1.4}$$

$$\rho\left(\frac{\partial u_i}{\partial t} + u_j \frac{\partial u_i}{\partial x_j}\right) = -\frac{\partial p}{\partial x_i} + \frac{\partial T_{ij}}{\partial x_j} \tag{1.5}$$

where $u_i(\boldsymbol{x}, t)$ is the *i*-th instantaneous velocity component, $p(\boldsymbol{x}, t)$ is the static pressure and ν the kinematic viscosity. For a Newtonian, constant-properties fluid, the viscous stresses tensor $T_{ij}(\boldsymbol{x}, t)$ can be defined as:

$$T_{ij} = \mu\left(\frac{\partial u_i}{\partial x_j} + \frac{\partial u_j}{\partial x_i}\right); \tag{1.6}$$

by substituting this into Eq.(1.5) we obtain:

$$\frac{\partial u_i}{\partial t} + u_j \frac{\partial u_i}{\partial x_j} = -\frac{1}{\rho}\frac{\partial p}{\partial x_i} + \nu \frac{\partial^2 u_i}{\partial x_j^2}, \tag{1.7}$$

In light of the fact that in this thesis only the fluid dynamics of a constant density fluid is investigated, the energy equation is decoupled from the momentum equation, therefore it will not be considered in our analysis.

1.1.3 Wall bounded turbulence

If we non-dimensionalize the momentum equation with the characteristic velocity V and length scale L, we end up with:

$$\frac{\partial \tilde{u}_i}{\partial \tilde{t}} + \tilde{u}_j \frac{\partial \tilde{u}_i}{\partial \tilde{x}_j} = -\frac{\partial \tilde{p}}{\partial \tilde{x}_i} + \frac{1}{Re}\frac{\partial^2 \tilde{u}_i}{\partial \tilde{x}_j^2}, \tag{1.8}$$

where the tilde symbol is representative of the dimensionless properties and the viscous effects are included in the Reynolds number. The presence of a wall in a flow implies two obvious boundary conditions:

- *Kinematic*: no fluid through the surface, hence normal velocity equal to zero;

- *No-Slip*: the tangential velocity of the fluid at the wall must equalize the tangential velocity of the wall itself.

As a consequence of these two points, velocities near a wall are damped, making the turbulent flow anisotropic, and increasing the production of turbulence because of the shearing mechanism. While for the kinematic boundary condition viscosity is not important, it is necessary for the no-slip condition to be satisfied. If the Reynolds number approaches infinity in Eq.(1.8), viscous effects disappear and with them the no-slip condition, sending us back to the D'Alambert paradox. At the beginning of the 20th century, Prandtl ingeniously solved this problem by introducing an additional length scale normal to the wall and a velocity scale that could keep at least one viscous stress term "alive". For a turbulent boundary layer, the friction velocity is the appropriate scale velocity, defined as:

$$u_\tau \equiv \sqrt{\frac{\tau_w}{\rho}}, \tag{1.9}$$

where τ_w is the wall shear stress. From Eq.(1.9), the near-wall length scale is defined as:

$$\eta = \frac{\nu}{u_\tau}, \tag{1.10}$$

not to be confused with the Kolmogorov's small scale. It is easily noticeable that the Reynolds number based on these newly defined wall-scales is equal to unit, meaning that the viscous forces are comparable with inertial forces. Using Eq.(1.10), we can define a dimensionless wall distance as:

$$y^+ \equiv \frac{y}{\eta} = \frac{yu_\tau}{\nu}, \tag{1.11}$$

where y is the normal distance from the wall. A very useful outcome is that, results from different experiments or simulations, at the same Reynolds number, can be compared using the dimensionless wall distance and velocity profiles, when the latter are non-dimensionalized by the friction velocity.

The turbulent boundary layer can be divided into regions based on dimensionless wall distance, as displayed in Fig.(1.4). The inner boundery layer is the part of the turbulent boundary layer in which the scales previously defined are introduced. Viscosity plays a role in its relative sublayer whereas it is neglected in the region with $y^+ > 30$. In the outer boundary layer the characteristic length and velocity scale are also redefined to solve the problem

of neglecting viscous effect from the equations. They are the boundary layer thickness δ, defined as the normal distance from the wall at which the mean velocity in the boundary layer is 99% of the free stream velocity, and the velocity U_∞ of the free stream, respectively.

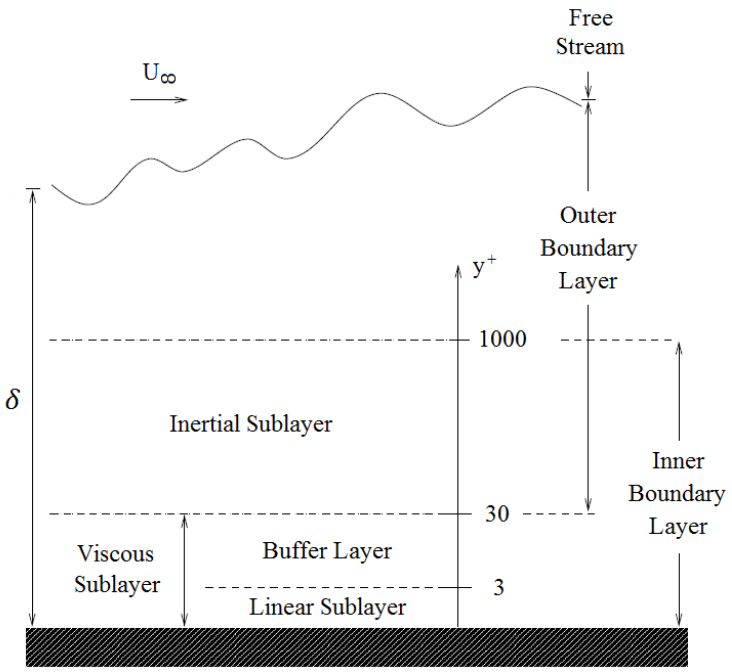

Figure 1.4. Turbulent boundary layer.

When a free flow develops into a confinement, the boundary layers of the walls merge at a certain distance from the inlet, after which the flow reaches the fully developed condition, as in the case of a pipe or channel flow.

The linear and inertial sublayer can be described by equations using the dimensionless variables:

$$LINEAR\ SUBLAYER \qquad U^+ = y^+, \tag{1.12}$$

$$INERTIAL\ SUBLAYER \qquad U^+ = \frac{1}{\kappa}\ln y^+ + B, \tag{1.13}$$

where κ and B are constant derived from experiments, and $U^+$is the streamwise velocity nondimensionalized by the friction velocity. Figure (1.5) shows an example of the linear and logaritmic approximations for a channel flow.

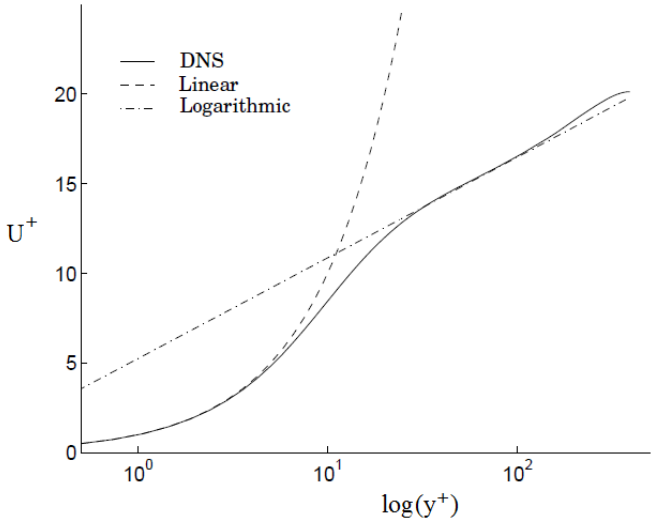

Figure 1.5. Dimensionless velocity profile example of a channel flow.

1.2 Statistical analysis

The instantaneous changes of physical properties are complicated, and data from experiments and simulations are abundant. Statistial analysis accomplishes a simplification of the the way we look at turbulence by breaking down stochastic variables into moments.

The first moment, also called mean value, is defined through the ensamble average as:

$$\langle a(\boldsymbol{x},t)\rangle = A(\boldsymbol{x},t) \equiv \lim_{N\to\infty}\frac{1}{N}\sum_{n=1}^{N} a^{(n)}(\boldsymbol{x},t), \qquad (1.14)$$

where $a(\boldsymbol{x},t)$ is a generic random variable and N is the number of independent realizations. Now that we have defined a mean value, an instantaneous variable can be viewd as the sum of its mean $A(\boldsymbol{x},t)$ and fluctuation $a'(\boldsymbol{x},t)$ around the mean. Omitting the dependence on space and time for the sake of clarity we can write:

$$a = A + a', \qquad (1.15)$$

which is known as the Reynolds decomposition.

A random variable is further described by the evaluation of its distribution around the mean, which is achieved through the second moment, or variance, calculated as:

$$var[a] \equiv \langle (a')^2 \rangle = \lim_{N\to\infty} \frac{1}{N} \sum_{n=1}^{N} (a_n - A)^2. \qquad (1.16)$$

From this statistical quantity we can define the root mean square of a random variable, $a_{RMS} = \sqrt{\langle (a')^2 \rangle}$, which is more widely used in the fluid dynamics community. In Fig.(1.6) the statistical properties mentioned so far are summarized by plotting an istantaneous velocity as a function of time.

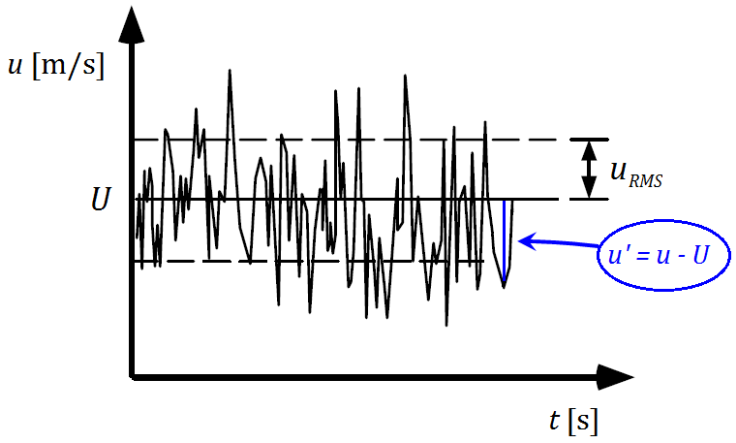

Figure 1.6. Reynolds decomposition and statistical quantities.

For stationary random processes, in which the statistical properties are independend of time, the ensamble average is the same as the time average:

$$\langle a(\boldsymbol{x}, t) \rangle = A(\boldsymbol{x}, t) \equiv \lim_{T\to\infty} \frac{1}{T} \int_0^T a^{(n)}(\boldsymbol{x}, t) dt. \qquad (1.17)$$

The generic random variable $a(\boldsymbol{x}, t)$ used in this section to define the statistical quantities, can be any of the physical quantities that describe the flow, e.g. velocity vector.

It is worth mentioning that, even though only the first and second moment are here introduced, the description of a stochastic process such as turbulence can be enriched by looking at the higher moments of a random variable.

1.3 Experimental analysis

Fluid experiments performed today with state-of-the-art facilities are sophisticated to the point that we can clearly see the structures present in a flow field, vortexes shedding from a cylinder, shock waves and so on. Most importantly we can quantify all this information in terms of instantaneous velocities, pressure and temperature that, with appropriate algorithms, can be interpreted as mean and fluctuating quantities. These can be subsequently used to analyze the physics behind flow conditions, such as turbulence, obtain data for engineering applications or validate numerical models.

The two most widely recognized techniques used to obtain velocity measurements of a flow field are the Laser Doppler Velocietry (LDV) and the Particle Image Velocimetry (PIV). Both of them are non-intrusive, meaning that the measures are performed without disturbing the natural flow motion. The main difference is that, LDV is punctual in its measurements and useful to compare mean velocity and root mean squared (RMS) turbulence profiles, while the PIV provides velocity vectors in a cross-section of the flow and, as a consequence, is a good tool for the visualization of the flow structures.

In this work, the LDV is used and therefore only its details are here introduced.

1.3.1 Laser Doppler Velocimetry

Laser light is famous for being higly coherent in space and time, meaning that its narrow beams can focus on tiny spots with parallel wavefronts at a single frequency and in phase. According to the fringe model [25], if we split a monochromatic laser beam into two arms and subsequently intersect them, a small measuring volume, the probe volume, emerges (Fig.(1.7)). The interference of the two arms forms a pattern of parallel planes of high intensity light, named fringes. The distance between fringes is known from calibration, and calculated as:

$$\delta_f = \frac{\lambda}{2\sin\left(\theta/2\right)} \tag{1.18}$$

where λ is the wavelength and θ is the angle between the two laser beams. The probe volume can be seen as a region of luminous and dark planes. When particles seeded into the moving fluid travel through fringes, they scatter light whose intensity is proportional to the local light intensity, and frequency linearly dependent on the relative particle velocity through the Doppler effect. This fluctuating light intensity is collected by the photomultiplier and then

converted into an electrical sinusoidal signal, called Doppler burst (or Doppler signal). After being filtered and amplified, this signal is used to determine the Doppler frequency f_D, which multiplied by Eq.(1.18) yields:

$$V = f_D \delta_f \tag{1.19}$$

where V is the velocity of the particle perpendicular to the fringe planes.

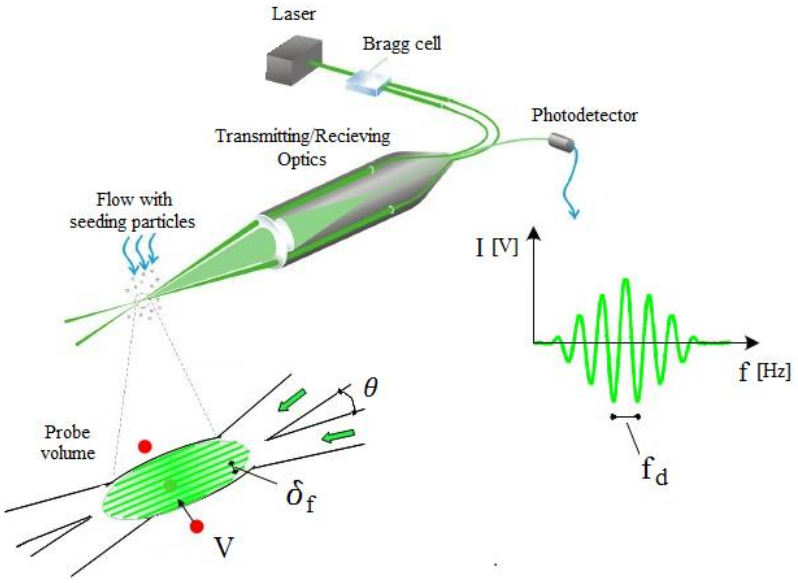

Figure 1.7. LDV schematics.

The procedure described is valid for evaluating one component of the velocity. Second and third components can be acquired in the same way by adding one or two pair of laser beams at different wavelenghts.

In order to better understand how laser light is converted from its origin to the velocity components signals that are quantitatively percievable, it is appropriate to follow the laser through its "path", from the origin to the transformation into electrical signal, subsequently converted in velocity components.

Laser source

Argon ion lasers have become the most extensively used lasers sources for a variety of applications, including scientific researches. Ultra-pure, low-pressure argon gas, sealed into a plasma tube, is used as the gain medium, the source of optical gain of the laser. In order to achieve this functionality, a high direct

current of several tens of ampers, applied at several hundreds volts, is run throguh the gas, keeping it in a high-tempreature plasma state. The continuous wave of beam generated can include several wavelenghts among which $\lambda = 488\,\text{nm}$ and $\lambda = 514.5\,\text{nm}$, corresponding to the blu and green colors of the electromagnetic spectrum, respectively, are the most commonly used. Its reliability make it suitable in research laboratoris, but they have a price to be paid. Operating this kind of lasers requires a large power electrical source, special materials for the construction of the plasma tube and an efficient cooling system for the prevention of overheating.

Transmitting optics

The laser beam coming from the plasma tube enters a series of optical devices aimed at manipulating and managing the laser for the creation of the optimal measuring conditions. A schematics representation of these components is given in Fig.(1.8).

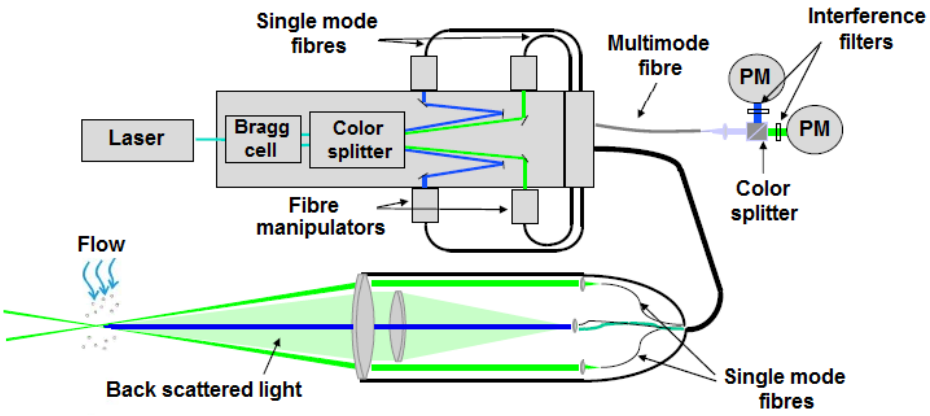

Figure 1.8. Schematics of the 2D transmitting optics.

First, the laser beam generated enters the Bragg cell, an acousto-optic modulator used for two important processes:

- *Beam splitting*: The beam of light is splitted into two arms, which are later intersected to form the probe volume. This is an important component because if we had two beams with the same wavelenghts coming from different sources, their peaks would not align to form fringes, and therefore we could not originate the sinusoidal electric signal used to detect particles velocity.

- *Frequency shifting*: once separated, the frequency of one of the arms of the monochromatic laser beam is shifted, typically by $f_s = 40$ MHz, with respect to the other, causing the fringes to move in space. LDV systems without this frequency shift would not be able to distinguish neither flow direction nor zero velocities.

The two beams are then splitted in two colors, resulting in four different arms that allow measurements of two velocity components. Before reaching the laser probe via optical fibres, laser beams must be calibrated with fibre manipulators to get rid of the small deviations from the nominal fringe spacing gained during the laser's path in order to limit systematic errors on the measured velocities.

Once the beams reach the laser probe, they are redirected through a beam expander aimed to increase beam separation. This last component, shown in Fig.(1.9) for a single laser wavelength, consents to reduce the size of the probe volume and increase its power density.

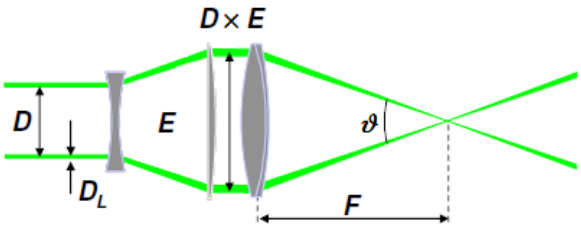

Figure 1.9. Detail of a monochromatic beam expander.

Even though the laser beam seems straight, in reality it does diminish its cross section. Optimal performance of the LDV equipment is reached when measurements take place at the intersection of the beam waists, defined as the smallest cross sections of the laser beam. Here, the Gaussian intensity distribution in the beams is responsable for the formation of an ellipsoidal probe volume, as depicted in Fig.(1.10).

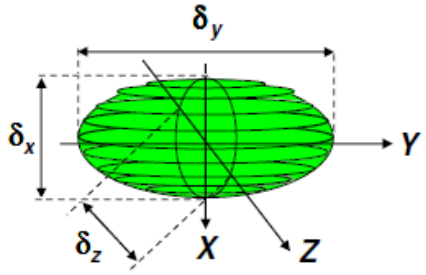

Figure 1.10. Probe volume from the intersection of the beam waists.

From the parameters indicated in Fig.(1.10) we can define the three dimensions representing the probe volume in a cartesian coordinate system as:

$$\delta_x = \frac{4F\lambda}{\pi E D_L \cos\left(\theta/2\right)}, \quad \delta_z = \frac{4F\lambda}{\pi E D_L}, \quad \delta_y = \frac{4F\lambda}{\pi E D_L \sin\left(\theta/2\right)}, \quad (1.20)$$

where F is the lens' focal length, E is beam expansion and D_L is the inital beam thickness.

Light scattered from the fringes is then captured in the laser probe, color splitted and sent to a photomultiplier (PM), one for each wavelength. Here is where light ends its path. Simply put, photons are channeled to the photo-cathode, a photosensitive surface from which electrons are easily released. Each electron, subjected to an applied electrostatic field, accellerates toward an electrode called dynode where, upon impact, releases more electrons. Accellerated electrons impacting through a cascade of dynodes increase exponentially until their number is enough to generate a detectable current pulse at the anode.

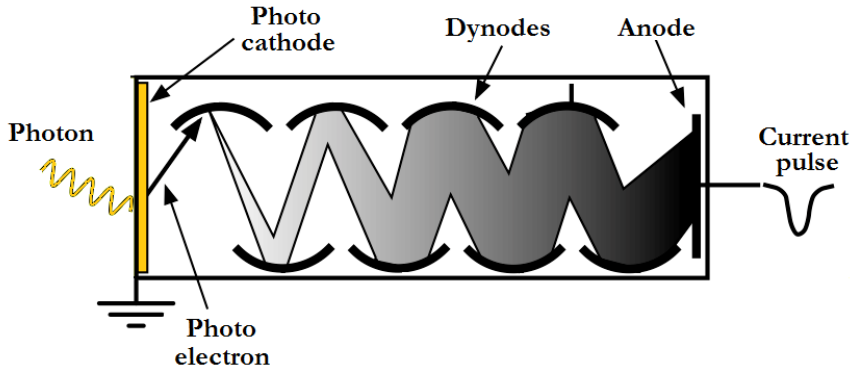

Figure 1.11. Schematic view of a photomultiplier.

Even though light ends its path in the PM, the information that it carries is still present in the current pulse.

Signal Processing

Both the green and blue signals must now be processed with Burst Spectrum Analyzers (BSA). The current pulse, called the Doppler signal (burst), goes through band-pass filters for maximizing the signal-to-noise ratio, as shown in Fig. (1.12), where the pedestal represents the DC-part removed by a high-pass

filter. The filtered signal, usually monitored by an oscilloscope, contains the Doppler frequency which must be extracted for the evaluation of the particles velocity. This requirement is achieved by means of a spectrum analysis of the entire Doppler signal performed with a Discrete Fourier Transform of the time signal. The peak of the calculated discrete spectrum represents the Doppler frequency.

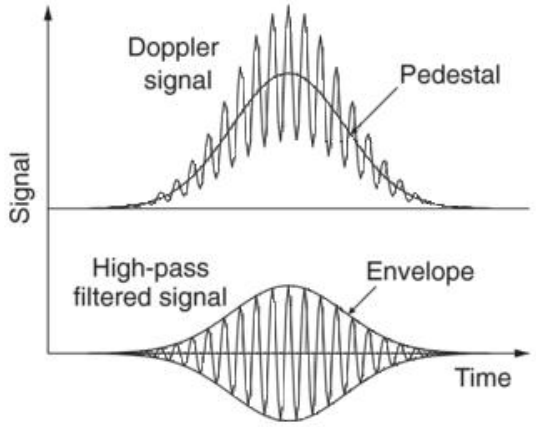

Figure 1.12. Filtered Doppler signal.

The casual distribution of particles through the fluid, their size and trajectory contribute to a random occurrence and variation of the bursts in time [28]. The detection of a time series of Doppler signals (Fig.(1.13)) is achieved by setting a low detection threshold level above which the signals are detected and, if validated by the BSA [29], stored. Lowering this limit would cause an increase of the data rate accompanied with an introduction of noise and viceversa. In addition, a higher threshold could be set to reject eccessively high-amplitude signals.

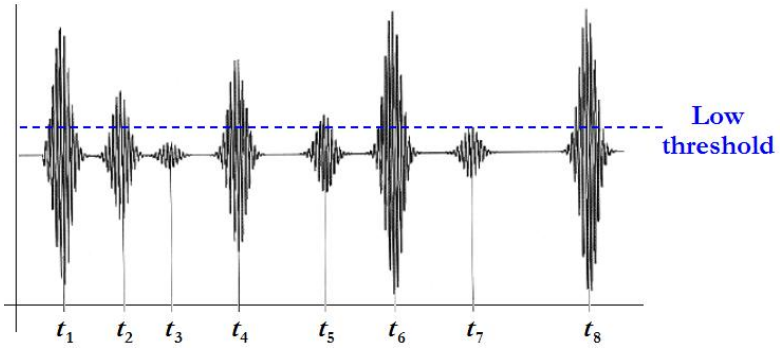

Figure 1.13. Time series of Doppler signals.

The pedestal and the envelope of the signal are the parameters used for the detection and validation of a burst for both the low and high detection limits.

1.4 Numerical analysis

The Navier Stokes equations represent a system of partial differential equations (PDEs) that cannot be solved analytically without simplifications. Among the several numerical methods used for solving the PDEs, namely finite difference method, finite elements method and finite volume method, the last one has been extensively used in several engineering fields. The domain is discretized in cells, called control volumes, on which the equations are locally solved, with the advantage of satisfying the integral conservation over each control volume. Given this characteristic, this robust scheme, used with both structured and unstructured meshes, is particularly attracting when the modellization of fluxes is important, such as in the case of fluid mechanics. The solver used for the simulations in this thesis adopts the finite volume method for the solution of the equations of fluid motion.

The solution of the NSE can find its applications in both the fundamental study of turbulence and engineering problems, which basically differ on the level of description and accuracy of the numerical data. As we noted from Kolmogorov's theory, energy is distributed among various frequencies, with a gap between large and small scales depending on the Reynolds number of the main flow. Figure (1.14) shows how different numerical approaches can interpret the energy spectrum based on their approximation level of the exact continuous solution of the Navier-Stokes equations.

If we want to predict a flow field with the maximum quality, we surely need to capture the whole range of scales of the real solution with a Direct Numerical Simulation (DNS). This is achieved by discretizing the space and time domain into steps that are smaller than the characteristic length and time associated with the smallest scale (η, τ_η). Practically, this is the simplest of all numerical approaches, but it requires a minimum number of grid points proportional to Re_L^3. Nowadays, computers are nowhere powerful enough to perform such calculations at high Reynolds numbers, therefore DNS is reserved for fundamental studies of turbulence and model validation due to its high level of accuracy.

We need approximations in order to investigate a broader selection of applications and decrease the computational time as well. Next in line in terms of accuracy of the results is the Large Eddy Simulation (LES). Solely certain low-frequency modes are calculated directly through a local time-space separation of the scales of motion, which are the ones containing most energy. The remaining high frequency modes, assumed to be isotropic and more

universal, i.e. independent of the application, are modelled (Fig.(1.14)). Foundamental turbulence could still be studied due to the possibility of getting both high order statistics and some detailed structures of the flow. In addition, due to the exponential increase of computer power, applications in industries are becoming more and more common, but still limited to reltively low Reynolds number.

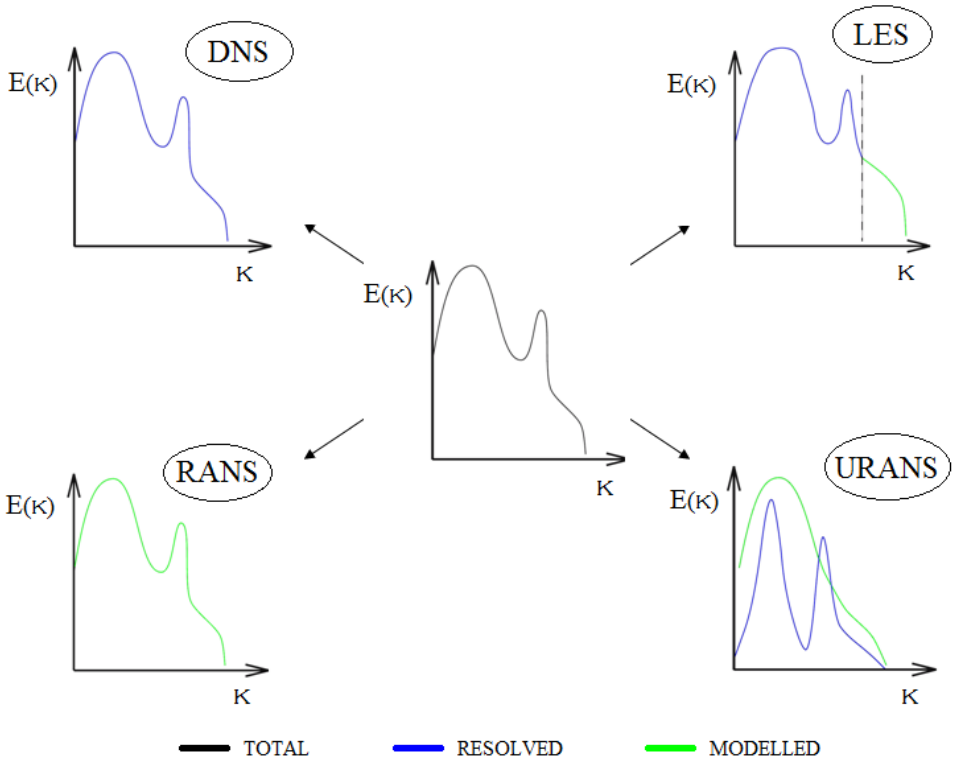

Figure 1.14. Energy spectrum approximation of the numerical approaches.

When we are in need of diminishing the computational time even more, and our attention is limited to the general characteristics of a flow, we are required to reduce the volume of information significantly. This is the case of engineering applications in which only the mean properties are necessary and the statistical details are not important. Proceeding toward a decrease of accuracy, we find the Unsteady Reynolds Averaged Navier Stokes (URANS) approach. Considering that only certain low-frequency modes are directly calculated, while the majority is modelled, this algorithm is suited for applications involving unsteady flows. Since not all the frequencies are averaged, the ensemble average technique must be used for the evaluation of the mean values. On the other hand, the time average is adopted when the flow is statistically stationary, which is the case of the Reynolds Averaged Navier Stokes (RANS) approach. Here, all the

frequencies of the energy spectrum are modelled, as shown in Fig.(1.14). In these last two cases, in which a statistical average is performed on the NSE, fluctuations are indirectly represented through turbulence models that need to effectively reflect their presence in order to be considered as a valid tool for the prediction flow fields.

Since LES and URANS are the two level of approximations used for the numerical analysis in this thesis, they will be further discussed subsequently.

1.4.1 URANS approach

The process of averaging the NSE consists in applying the Reynolds decomposition, Eq.(1.15), to the mass and momentum equations, Eq.(1.4) and Eq.(1.7) respectively. The result is:

$$\frac{\partial U_j}{\partial x_j} = 0, \tag{1.21}$$

$$\rho\left(\frac{\partial U_i}{\partial t} + U_j\frac{\partial U_i}{\partial x_j}\right) = -\frac{\partial P}{\partial x_i} + \frac{\partial}{\partial x_j}\left(\mu\frac{\partial U_i}{\partial x_j} - \rho\langle u_i' u_j'\rangle\right). \tag{1.22}$$

Comparing the averaged with the instantaneous equations, it is noticeable that while the continuity equation preservs its form, the momentum equation does not. The reason lies in the non-linearity of the momentum equation. In fact, when averaging the non-linear term on the left-hand side of Eq.(1.7), and combining it with Eq.(1.4), we obtain:

$$\langle u_j\frac{\partial u_i}{\partial x_j}\rangle + 0 = \langle u_j\frac{\partial u_i}{\partial x_j}\rangle + \langle u_i\frac{\partial u_j}{\partial x_j}\rangle = \frac{\partial}{\partial x_j}\langle u_i u_j\rangle. \tag{1.23}$$

Remembering that $\langle a'\rangle = 0$, $\langle a'A\rangle = 0$ and $\langle A\rangle = A$, we can write:

$$\langle u_i u_j\rangle = U_i U_j + \langle u_i' u_j'\rangle, \tag{1.24}$$

in which the additional term of the momentum equation here appears. If we take a look at the parentheses on the right-hand side of Eq.(1.22), we can come to realize that the dimension of the two terms inside is of a stress. While the first one, named viscous stress, was already part of the NSE, the newly entered term, named Reynolds stress, even though is not a stress at all, acts as if it were, at least as far as the mean motion is concearned. The issue, referred to as the turbulence closure problem, is that now we ended up with more unknowns than

equations, and we need to relate them to the mean motion if we want to solve the equations.

A similar problem arose when the continuum hypothesis was introduced. Molecular characteristic length and velocity scales were averaged, the viscous stress arose as a consequence, and there was the need to link it to the fluid motion. This linkage, or closure, was easily achieved through constitutive equations (e.g., Eq.(1.6)) that depended solely on the properties of the fluid material because the averaged scales were much smaller than those required for our purposes, the macroscopic behavior of the fluid. Now, if we try to simplify this macroscopic domain by averaging over its own scales, which are the ones we are actually interested in, the resultant Reynold stress will be directly related to the flow itself, and its closure is much tougher to achieve. Turbulence is indeed a property of the flow, not the fluid.

The closure problem is not an easy one because it requires a deep knowledge of the turbulence behavior. It is worth mentioning that since all the turbulence scales need to be modelled, when we exceed the range of applications for which the correlations for the closure problem were tested, serious inaccurancy and unphysical results could be generated. Therefore, it is theoretically impossible to define a "universal" model that is suitable for all the flows.

Hereafter, a brief introduction of the turbulent models for the closure problem used in this thesis is presented.

Reynolds stress model

The Reynolds Stress Model (RSM) approach starts with the assumption of rearranging the equations governing the fluctuations to seek new equations for the nine unknowns derived from averaging the NSE. Subtracting Eq.(1.22) from Eq.(1.7), multiplying the resultant equation by u_k' and averaging, yields:

$$\rho\left[\langle u_k'\frac{\partial u_i'}{\partial t}\rangle + U_j\,\langle u_k'\frac{\partial u_i'}{\partial x_j}\rangle\right] = -\langle u_k'\frac{\partial p'}{\partial x_i}\rangle + \langle u_k'\frac{\partial \tau_{ij}'}{\partial x_j}\rangle - \rho\left[\langle u_k'u_j'\rangle\frac{\partial U_i}{\partial x_j}\right] - \rho\left[\langle u_k'u_j'\frac{\partial u_i'}{\partial x_j}\rangle\right] \quad (1.25)$$

being both i and k free indeces, they can be interchanged to form a second equation. Adding it to Eq.(1.25) and rearranging some terms [25], yields to the Reynolds stress transport equations:

$$
\begin{aligned}
&\textit{CONVECTIVE} && \frac{\partial}{\partial t}\langle u_i' u_k' \rangle + U_j \frac{\partial}{\partial x_j}\langle u_i' u_k' \rangle = \\
&\textit{PRESSURE STRAIN} && + \langle \frac{p'}{\rho}\left[\frac{\partial u_i'}{\partial x_k} + \frac{\partial u_k'}{\partial x_i}\right] \rangle \\
&\textit{PRESSURE DIFFUSION} && - \frac{\partial}{\partial x_j}\left\{\frac{1}{\rho}\left[\langle p' u_k' \rangle \delta_{ij} + \langle p' u_i' \rangle \delta_{kj}\right]\right\} \\
&\textit{TURBULENT DIFFUSION} && - \frac{\partial}{\partial x_j}\langle u_i' u_k' u_j' \rangle \\
&\textit{VISCOUS DIFFUSION} && - \frac{\partial}{\partial x_j}\left[\nu \frac{\partial}{\partial x_k}\langle u_i' u_j' \rangle\right] \\
&\textit{STRESS PRODUCTION} && + \left[\langle u_i' u_j' \rangle \frac{\partial U_k}{\partial x_j} + \langle u_k' u_j' \rangle \frac{\partial U_i}{\partial x_j}\right] \\
&\textit{DISSIPATION RATE} && -2\nu \langle \frac{\partial u_i'}{\partial x_j}\frac{\partial u_k'}{\partial x_j} \rangle
\end{aligned}
\qquad (1.26)
$$

Now that we have related the Reynolds stresses with the mean motion, we ended up with even more unknowns than before. Closure is achieved by modelling the turbulence diffusion, pressure-strain and dissipation terms of Eq.(1.26) through a large number of correlations and coefficients based on experiments or DNS. Since the terms that require modelling are tensors, closure approximations are very elaborate. More information is available in literature [26, 30].

The RSM is the most complex of turbulence models, but on the bright side, the nature of this approach makes it possible to provide physically realistic results for complex flows that experience rapid changes in the mean strain rate, secondary motions, three-dimensionality and separation.

Turbulent viscosity models

In 1877 Boussinesq proposed an hypothesis for the evaluation of the Reynolds stress tensor that is mathematically analogous to the Newtonian model for the viscous stress in a fluid. Through the introduction of a fictitious viscosity the Reynolds stress looks like:

$$\rho\langle u_i' u_j' \rangle - \frac{1}{3}\rho\langle u_i' u_i' \rangle = -\frac{1}{2}\mu_t\left(\frac{\partial U_i}{\partial x_j} + \frac{\partial U_j}{\partial x_i}\right), \qquad (1.27)$$

meaning that the anisotropy tensor on the left hand-side of the equation is proportional to the mean rate-of-strain tensor through the turbulent or eddy viscosity μ_t. A major distinction between the physical viscosity μ and the turbulent viscosity μ_t is that the latter entirely depends on the motion, whereas the former depends only on the fluid.

If we accept the Boussinesq hypothesis, the problem is moved to the definition of the turbulent viscosity, which can be done by defining transport equations for turbulent quantities. The present work only referres to two-equation models, which define the turbulence viscosity by introducing two transport equations. One of these equations, which is common among the models here considered, comes from the turbulence kinetic energy of the fluctuations, defined as:

$$k = \frac{1}{2}\langle u_i' u_i' \rangle = \frac{1}{2}\left(\langle u_x'^2 \rangle + \langle u_y'^2 \rangle + \langle u_z'^2 \rangle\right). \tag{1.28}$$

By contracting the free indices of Eq.(1.26) and using Eq.(1.28), we can define the transport equation for the turbulence kinetic energy as:

$$\frac{\partial k}{\partial t} + U_j \frac{\partial k}{\partial x_j} =$$

$$\frac{\partial}{\partial x_j}\left\{-\frac{1}{\rho}\langle p' u_i' \rangle \delta_{ij} - \frac{1}{2}\langle u_i' u_i' u_j' \rangle + \nu \frac{\partial k}{\partial x_j}\right\} - \langle u_i' u_j' \rangle \frac{\partial U_i}{\partial x_j} - \nu \langle \frac{\partial u_i'}{\partial x_j}\frac{\partial u_i'}{\partial x_j} \rangle \tag{1.29}$$

from which we can distinguish the same terms of Eq.(1.26), aside from the pressure-strain, eliminated by the continuity equation. By assuming that the sum of turbulence and pressure diffusion terms is:

$$\frac{1}{\rho}\langle p' u_i' \rangle \delta_{ij} + \frac{1}{2}\langle u_i' u_i' u_j' \rangle = \frac{\nu_t}{\sigma_k}\frac{\partial k}{\partial x_j} \tag{1.30}$$

we can rewrite the kinetic energy transport equation as:

$$\frac{\partial k}{\partial t} + U_j \frac{\partial k}{\partial x_j} = \frac{\partial}{\partial x_j}\left\{\frac{1}{\rho}\left(\mu + \frac{\mu_t}{\sigma_k}\right)\frac{\partial k}{\partial x_j}\right\} - \langle u_i' u_j' \rangle \frac{\partial U_i}{\partial x_j} - \varepsilon \tag{1.31}$$

where σ_k is the turbulent Prandtl number for the turbulence kinetic energy and ε is the turbulence dissipation rate.

The second transport equation depends on the turbulence model considered:

- *k-ε model*: originlly proposed by Jones and Launder [31], it defines the turbulent viscosity as:

$$\mu_t = \rho C_\mu \frac{k^2}{\varepsilon}. \tag{1.32}$$

The second transport equation for the turbulence dissipation rate is:

$$\frac{\partial \varepsilon}{\partial t} + \frac{\partial (\varepsilon U_j)}{\partial x_j} = \frac{\partial}{\partial x_j}\left[\frac{1}{\rho}\left(\mu + \frac{\mu_t}{\sigma_\varepsilon}\right)\frac{\partial \varepsilon}{\partial x_j}\right] + C_{\varepsilon 1}\frac{\varepsilon}{k}P_k - C_{\varepsilon 2}\frac{\varepsilon^2}{k}, \tag{1.33}$$

where σ_ε is the turbulent Prandtl number for the turbulence dissipation rate. The closure coefficients are shown in Table (1.1):

C_μ	σ_k	σ_ε	$C_{\varepsilon 1}$	$C_{\varepsilon 2}$
0.09	1.0	1.3	1.44	1.92

Table 1.1. *k-ε* model closure coefficients.

- *k-ω model*: originally proposed by Wilcox [30], it defines the turbulent viscosity in the same way as the previous model, Eq.(1.32), and the turbulence dissipation rate as:

$$\varepsilon = C_\mu \omega k \tag{1.34}$$

The second transport equation is, in this case, for the specific dissipation rate ω:

$$\frac{\partial \omega}{\partial t} + \frac{\partial (\omega U_j)}{\partial x_j} = \frac{\partial}{\partial x_j}\left[\frac{1}{\rho}\left(\mu + \frac{\mu_t}{\sigma_\omega}\right)\frac{\partial \omega}{\partial x_j}\right] + \alpha\frac{\omega}{k}P_k - \beta\omega^2, \tag{1.35}$$

where σ_ε is the turbulent Prandtl number for the specific dissipation rate. The closure coefficients are shown in Table (1.2):

C_μ	σ_k	σ_ω	α	β
0.09	1.0	1.3	1.44	1.92

Table 1.2. *k-ω* model closure coefficients.

By introducing the Boussinesq hypothesis we simplified the closure problem, making the models presented easy to compute. Its simple relationship linearly links the Reynolds stresses with the velocity gradients through a scalar,

the turbulent viscosity, which poses the assumption of isotropy. While this works very well for many flows of engineering interest, it may also lack accuracy in complex flows.

Non linear models

The equation governing turbulent phenomena are not linear. The linear hypothesis introduced in the previous models limits their applications on simple flows. Explicit Algebraic Reynolds Stress Models (EARSM), first introduced by Pope in 1975 [26], utilize a two-equation model along with a non-linear constitutive relation to overcome these limitations adopting a general cubic formulation as follows:

$$
\begin{aligned}
-\langle u_i' u_j' \rangle = & -\frac{2}{3} k \delta_{ij} + \frac{1}{\rho} \mu_t \langle S_{ij} \rangle - C_1 \mu_t \frac{k}{\varepsilon} \left[\langle S_{ik} \rangle \langle S_{kj} \rangle - \frac{1}{3} \delta_{ij} \langle S_{kl} \rangle \langle S_{kl} \rangle \right] \\
& - C_2 \mu_t \frac{k}{\varepsilon} \left[\langle \Omega_{ik} \rangle \langle S_{kj} \rangle + \langle \Omega_{jk} \rangle \langle S_{ki} \rangle \right] - C_3 \mu_t \frac{k}{\varepsilon} \left[\langle \Omega_{ik} \rangle \langle \Omega_{kj} \rangle - \frac{1}{3} \delta_{ij} \langle \Omega_{kl} \rangle \langle \Omega_{kl} \rangle \right] \\
& - C_4 \mu_t \frac{k^2}{\varepsilon^2} \left[\langle S_{ki} \rangle \langle \Omega_{lj} \rangle + \langle S_{kj} \rangle \langle \Omega_{li} \rangle \right] \langle S_{kl} \rangle \\
& + C_5 \mu_t \frac{k^2}{\varepsilon^2} \left[\langle \Omega_{il} \rangle \langle \Omega_{lm} \rangle \langle S_{mj} \rangle + \langle \Omega_{mj} \rangle \langle \Omega_{lm} \rangle \langle S_{il} \rangle - \frac{2}{3} \langle S_{lm} \rangle \langle \Omega_{mn} \rangle \langle \Omega_{nl} \rangle \delta_{ij} \right] \\
& + C_6 \mu_t \frac{k^2}{\varepsilon^2} \left[\langle S_{kl} \rangle \langle S_{kl} \rangle \langle S_{ij} \rangle \right] - C_7 \mu_t \frac{k^2}{\varepsilon^2} \left[\langle \Omega_{kl} \rangle \langle \Omega_{kl} \rangle \langle S_{ij} \rangle \right]. \qquad (1.36)
\end{aligned}
$$

where

$$
\langle S_{ij} \rangle \equiv \frac{1}{2} \left(\frac{\partial U_i}{\partial x_j} + \frac{\partial U_j}{\partial x_i} \right), \qquad \langle \Omega_{ij} \rangle \equiv \frac{1}{2} \left(\frac{\partial U_i}{\partial x_j} - \frac{\partial U_j}{\partial x_i} \right) \qquad (1.37)
$$

are the mean rate of strain and mean rate of rotation, respectively.

A third order, non linear formulation for the Reynolds stress tensor developed by the CFDLab at Politecnico di Milano [32], is used in this thesis. Its purpuse is to increase the range of applicability of the k-ε models and their capability for the design of engineering applications.

All turbulence models are required to satisfy the foundamental physics of turbulence through several physical and mathematical constrains such as:

- $\langle u_i' u_i' \rangle \geq 0$,
- $\langle u_i' u_j' \rangle^2 \leq \langle u_i'^2 \rangle \langle u_j'^2 \rangle$.

This process, introduced by Schumann in 1977 [33], goes under the name of *realizability*.

1.4.2 LES approach

The idea that stands behind a Large Eddy Simulation is that on one side we do not want to model everything, losing the details of all the scales of motion, but on the other, we do not want to spend years waiting for the results of a simulation that accounts for all of them. In light of this considerations, only the large energetic eddies, affected by the flow geometry and non universal, are simulated directly while the smaller eddies, more universal, are modelled. This, in turn, leads to a reduction of the degrees of freedom, since the grid required does not have to capture small structures, named Sub Grid Scales (SGS), as shown in Fig.(1.15).

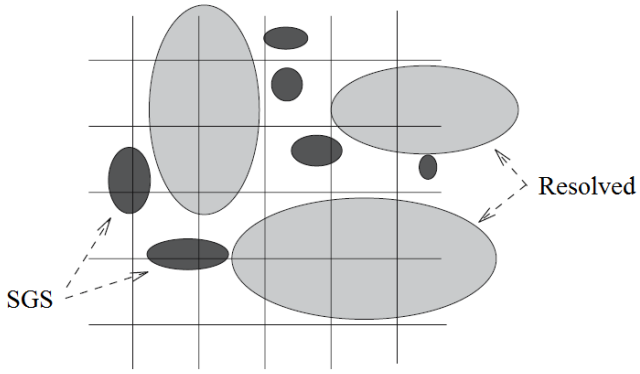

Figure 1.15. Resolved vs. SGS structures.

The first step for a LES approach consists in defining a function G that acts as a low-pass frequency filter. By defining a filtered velocity through a general filtering operation such that:

$$\bar{u}_i(\boldsymbol{x}, t; \Delta) = \int_{\mathbb{R}^3} G(\boldsymbol{r}, \boldsymbol{x}; \Delta) u_i(\boldsymbol{x} - \boldsymbol{r}) d\boldsymbol{r}, \tag{1.38}$$

we can decompose the instantaneous velocity as follows:

$$u_i = \bar{u}_i + u_i^*, \tag{1.39}$$

where $\bar{u}_i$ is the filtered velocity, which represents the motion of the large eddies, and u_i^* is the residual velocity. Figure (1.16) displays the effect of the filtering operation on the instantaneous velocity in one dimension.

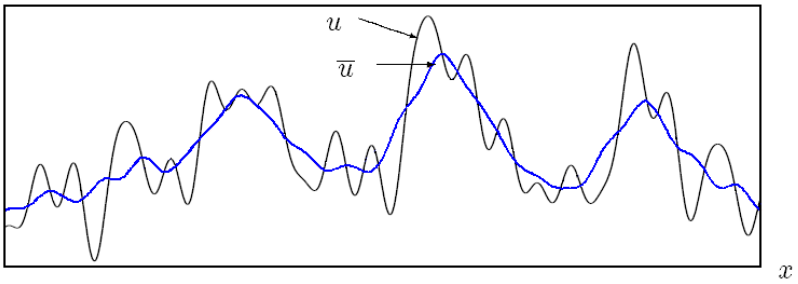

Figure 1.16. Filtering effect on the one-dimensional instantaneous velocity $\boldsymbol{u}(\boldsymbol{x})$.

The equations for the filtered velocity component can be derived by appliying the filtering operation Eq.(1.38) to the Navier Stokes equations. If we consider spatially uniform filters, so that filtering and differentiation commute, we can write:

$$\frac{\partial \bar{u}_i}{\partial x_i} = 0 \tag{1.40}$$

$$\frac{\partial \bar{u}_i}{\partial t} + \bar{u}_j \frac{\partial \bar{u}_i}{\partial x_j} = -\frac{1}{\rho}\frac{\partial \bar{p}}{\partial x_i} + \nu \frac{\partial}{\partial x_j}\left(\frac{\partial \bar{u}_i}{\partial x_j} + \frac{\partial \bar{u}_j}{\partial x_i}\right) - \frac{\partial \tau_{ij}^R}{\partial x_j} \tag{1.41}$$

where the non linearity of the convection term, as in the case of the Reynolds average, is the cause of the appearance of the residual-stress tensor:

$$\tau_{ij}^R \equiv \overline{u_i u_j} - \bar{u}_i \bar{u}_j \tag{1.42}$$

Again, there are more unknowns than equations, and we need to close the system. This time though, only the small scales (SGS), with a low energy level and hypothetically isotropic, need to be modelled. Therefore, a universal model suitable for all application is ideally possible. It is important to mention at this point that even if we do mathematically separate the large from the small scales of motion with a filtering function, they still physically influence one another, and this influence must be included in the SGS models.

The simplest and oldest model, the Smagorinsky model (1963), employs the same formulation used for the eddy viscosity models to define the residual-stress tensor:

$$\tau_{ij}^{R} = -2\nu_{SGS}\left(\frac{\partial \bar{u}_i}{\partial x_j} + \frac{\partial \bar{u}_j}{\partial x_i}\right) + \frac{1}{3}\tau_{ii}^{R}\delta_{ij}, \tag{1.43}$$

with the subgrid viscosity ν_{SGS} being now the parameter that needs modelling. Dimensionally we can express it as

$$\nu_{SGS} \propto l_{SGS}\, u_{SGS}, \tag{1.44}$$

where the characteristic length scale l_{SGS} and the characteristic velocity scale u_{SGS} of the unresolved motion can be expressed as:

$$l_{SGS} = C_s\Delta, \qquad u_{SGS} = l_{SGS}\sqrt{2\bar{S}_{ij}\bar{S}_{ij}}, \tag{1.45}$$

where $\bar{S}_{ij}$ is the filtered rate of strain and Δ is the filter width. The final expression for the subgrid viscosity can we written as:

$$\nu_{SGS} = (C_s\Delta)^2\sqrt{2\bar{S}_{ij}\bar{S}_{ij}} \tag{1.46}$$

Even though the energy cascade is an average process that transfers energy from the small to the large wavenumbers, the local and instantaneous transmition of energy could also backscatter, i.e. occur in the opposit direction. If we compare the rate of transferred energy from the filtered motions to the residual motions [26], defined as

$$\mathcal{P}_r \equiv -\left(\tau_{ij}^{R} - \frac{1}{3}\tau_{ii}\delta_{ij}\right)\bar{S}_{ij}, \tag{1.47}$$

with the residual viscous dissipation, expressed as

$$\varepsilon = \frac{q_{SGS}^3}{l_{SGS}}, \tag{1.48}$$

we can note that, using the equation introduced for the Smagorinsky hypothesis, the two terms are identical. This implies that the energy from the filtered motion is totally dissipated, without any backscattering.

Large Eddy Simulation is a powerful tool in the prediction of flow behavior, as it combines the advantages of the DNS, by solving even up to 80% of the energy spectrum, with the advantages of the URANS/RANS approaches, by reducing the degrees of freedom through modelling. Additional information on LES can be found in literature [26, 34].

1.4.3 Wall treatments

The presence of the no-slip and kinematic boundary conditions force a transition of the flow field from turbulent to laminar, creating the boundary layer regions of Fig.(1.4). The turbulent boundary layer can be differently predicted with the models previously introduced based on the characteristics of the models themselves.

Because of the way the k-ω models was formulated, it could be applied throughout the boundary layer if the near wall mesh resolution is adequate. On the other hand, the k-ε models and RSM are not valid in the near-wall region, but various approaches are available:

- *Wall Functions*: semi-empirical formulae are implemented to link the wall with the turbulent region. Only one node is necessary to describe the viscous sublayer, with the first grid centroid positioned at $30 < y^+ < 100$. In this case, turbulent transport equations do not need to be modified.
- *Two-Layer*: the domain is separated in two regions. In the turbulent region the transport equations are not modified, wheras in the viscosity affected region a simpler one-equation model is employed. While the momentum and k equations are retained, μ_t and ε equation are smootly blended between the two regions. The first grid centroid is typically at $y^+ \approx 1$.
- *Low-Reynolds*: damping functions are introduced in the transport equations to account for the influence of viscosity. In order to correctly resolve the gradients near the wall, the first grid centroid is at $y^+ \approx 1$.

Based on their grid requirement, it is evident that the wall functions approach is less computationally expensive than the two-layer and low-Reynolds approaches. However, its reliability is questionable when flow situations are different than the ones assumed for the derivation of the semi-empirical formulae.

In Large Eddy Simulation the choice of the near-grid approach is mainly influenced by the Reynolds number. From a physical point of view, when we move close to a surface the large scales assume the dimension of the boundary

layer thickness δ, and small scales exibith anisotropy and energy transfer mechanisms that are different than in turbulent regions. For these reasons the SGS models become inaccurate and if we want to capture the influence of the small scales we need a sufficiently fine grid, which means $0 \leq y^+ \leq 1$. An increse in the Reynolds number causes δ to decrease, which implies a higher grid resolution in all the domain. For these reasons, LES is resolved all the way to the wall, only when the Reynolds number is not excessive, otherwise wall functions are applied, and in this case the first point could be placed in the inertial sublayer $(20 \leq y^+ \leq 200)$.

Chapter 2

Experimental Facility

In the previous chapter, the main characteristics of the investigated physical phenomenon have been discussed. In this chapter the experimental facility specifically designed to assure the appropriate analysis of the chosen parallel jets configuration is described. The design of the facility is crucial for obtaining the characteristics of the flow field under consideration with the highest precision possible. What this chapter wants to convey are the steps that led to the construction of the facility, describing the layout of the system and its main components. In addition, the features of the instrumentation used for analyzing the velocity field are discussed. The facility is shown in Fig.(2.1).

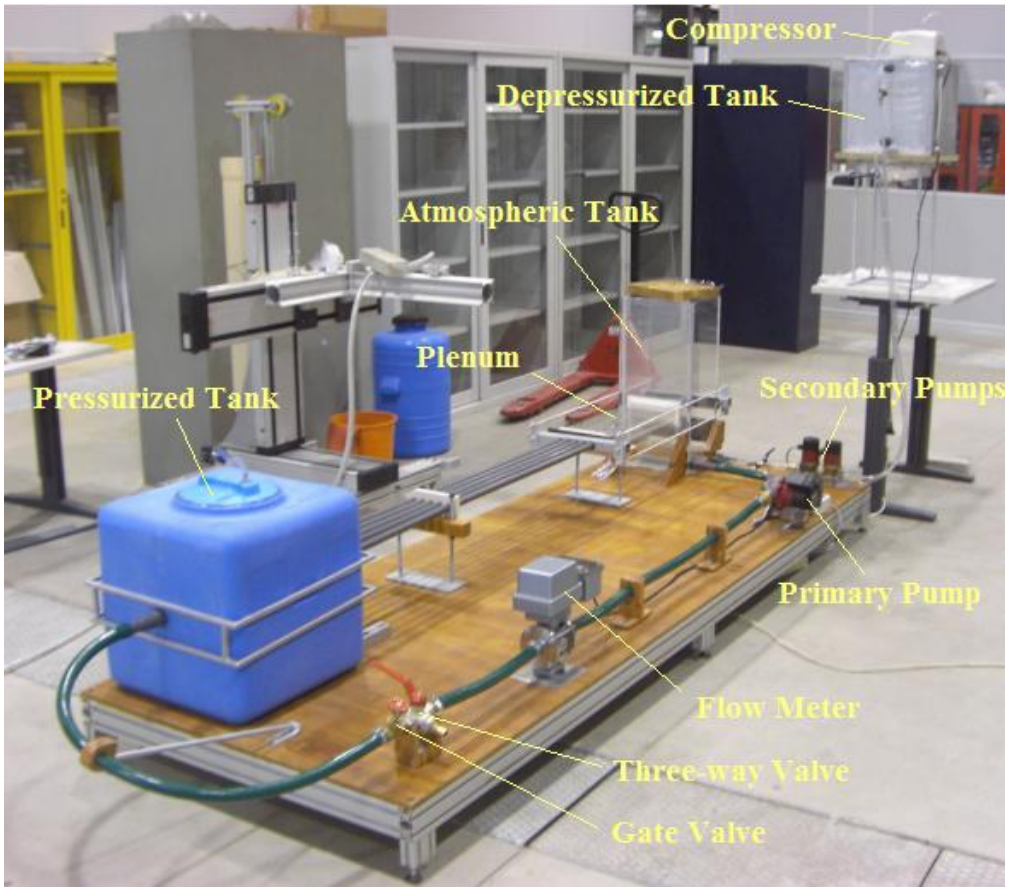

Figure 2.1. Experimental facility.

2.1 Description of the facility

The main components of the facility are here described, starting with the crucial description of the plenum, which represents the test section. The other components were selected and positioned in order to guarantee the optimal fluid dynamics of the confined jets.

2.1.1 Design of the test section

The objective behind the choice of the domain analyzed lies on the interest of studying a multiple confined jets configuration in which every single jet is subjected to the same "symmetrical forces" as the others, while undergoing a three dimensional expansion. Theoretically this could happen with an infinite number of jets in a row. Practically, its application can be found when jets expand into an annular confinement. Setting up an experimental facility to test annular jets is obviously challenging, not only from the construction point of view, but also for the measurements of velocity profiles and flow field with the available techniques, LDV and PIV respectively. The solution of this problem is in the design of a relatively simple facility aimed to extract enough details of the flow field to efficiently validate numerical models. A deep analysis of the jets behavior is then possible through experimental and numerical results, mainly LES, whereas the less computationally expensive URANS approaches, once validated, could be used for industrial applications of similar geometries.

Design Considerations

Jets are subjected to attractive forces when placed either adjacent or near a wall. The main cause of this attraction is in the subatmospheric region created by the fluid being entrained. The examination of Fig.(2.2), which is a summary of the literature mentioned in the introduction, is the first consideration for achieving the objective previously mentioned. Let us examine the case of equal momentum for each jet. If the two black free jets were considered separately, the forces F would cause the jets to combine and flap. By adding the blue jet between them, the flapping stops but the lateral jets still tend to join together, due to the asymmetrical forces of attraction applied on each of them. Since we know that the Coanda effect does generate attraction on a jet when placed near a surface, we can use this information to balance the forces acting on the jets by confining them (green lateral walls).

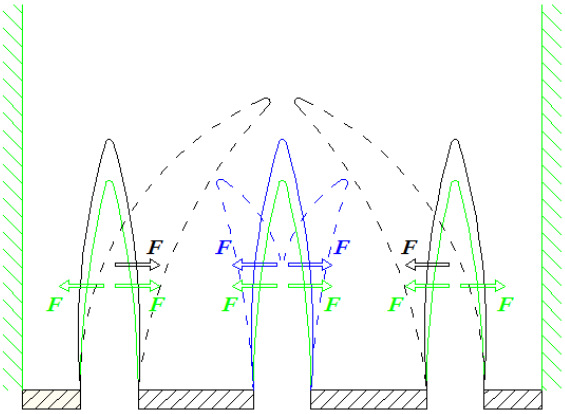

Figure 2.2. Forces acting on a confined three-jet configuration.

We also know that the deflection of a jet due to the presence of a wall depends on their relative distance. This distance was chosen in order for each jet to virtually have the same area *A* from which fluid can be entrained (Fig.(2.3)).

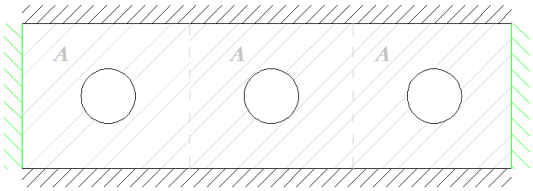

Figure 2.3. Front view of a confined three-jet configuration.

One last thought was given to the number of jets.With three jets, only the central one is not directly influenced by the lateral walls. For a more thorough analysis of multiple jets, two more jets were added.

With this configuration, we are trying to avoid the attraction on the three central jets and at the same time isolate them from the direct influence of the lateral walls with the presence of the two lateral jets. Ideally, we could be able to analyze the three central jets, in particular the central one, as if they were in an infinite row. Of course, this is a “first guess” configuration, since we have no a priori knowledge on how the forces acting on the jets could be properly balanced. However, this experimental campaign is important to validate the numerical models and used them, once approved, for further studies that could involve lateral wall distance, the use of periodic boundary conditions, and, eventually, a full annular parallel jets geometry.

The remaining dimensions of the test section were based primarily on space-saving. Since this facility was constructed specifically for this analysis, it seemd appropriate to make it as easy and accessible as possible.

Plenum structure

Based on the previous considerations, the geometrical parameters of the test section are summarized in Fig.(2.4). The jets issue into the plenum coming from five conduits with inner diameters of $D = 0.0212$ m.

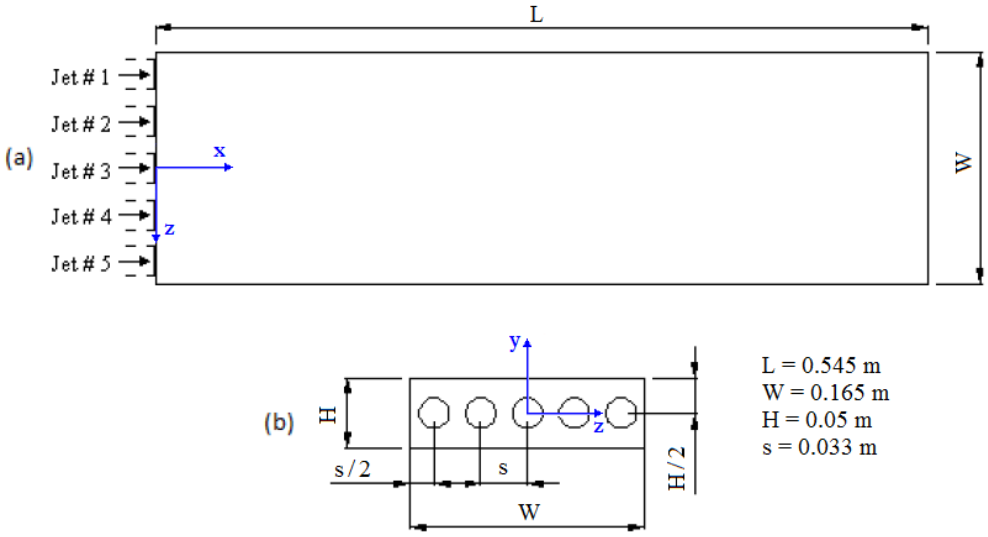

Figure 2.4. CAD design of the domain investigated. (a) top view, (b) front view.

The materials used for the construction of the plenum are important in terms of accuracy of the measurements. In particular, high quality measurements are guaranteed by using high quality optical glasses. Primary importance is given to the wall surface through which the reflected light of the laser sources passes, carrying the information about the velocity of the particles, for then being acquired by the instruments. Based on this consideration, the top wall is a transparent high-purity quartz glass, optically isotropic and homogeneous that avoids the possible alterations of the reflected laser light due to the cristalline structure of the glass itself. The remaining three walls of the plenum, which are less important, are made of basic transparent glass.

The two components that complete the assembly of the plenum are represented in Fig.(2.5). These two white PVC blocks represent the connetctive parts to the five pipes and the atmospheric tank. The one on the right was design to have a honeycomb-like geometry in order to isolate the plenum from the fluid instabilities that could occur in the atmospheric tank.

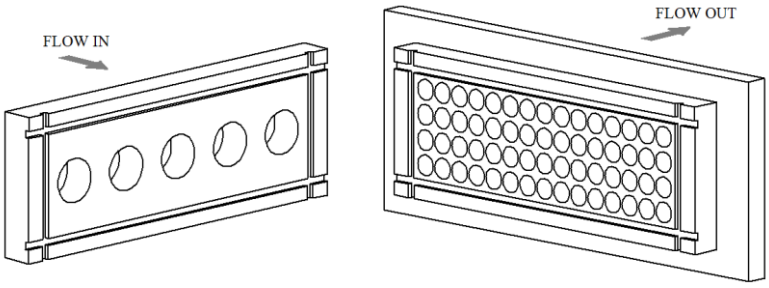

Figure 2.5. CAD design of the inlet (left) and outlet (right) section of the plenum.

The carved lines in both blocks represent the regions where the glass walls are inserted. The noticeable excessive width of the top and bottom transparent walls is due to the standard dimensions available for the quartz glass. A detail of the assambled plenum is shown in Fig.(2.6).

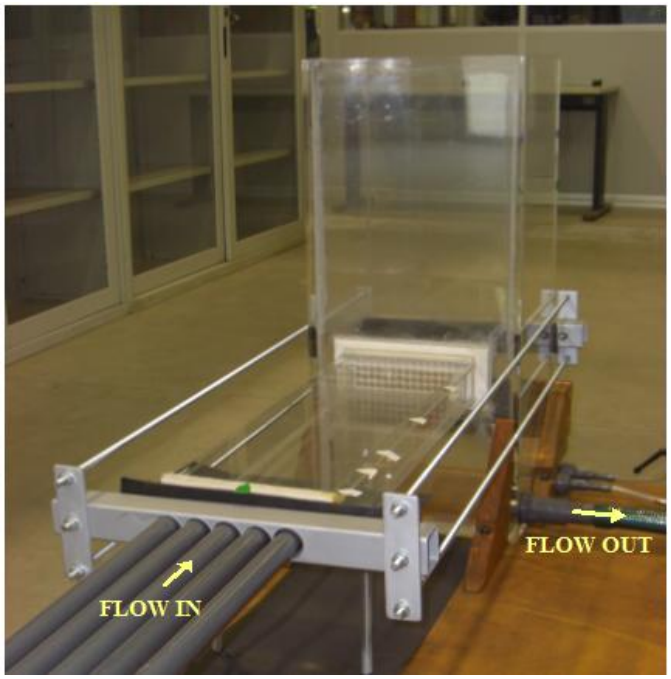

Figure 2.6. Detail of the plenum.

Any kind of vibration on the plenum could be problematic for two main reasons. First, all the components of the plenum were assembled with a special silicone adhesive for PVC, with the main purpose of avoiding any kind of leakage. The structure is consequently fragile. Secondly, during the measurements, small movements of the structure could influence the acquisition

of particles'velocities. As a result, screw tie rods were used to reinforce the plenum and keep it firmly connected to the atmospheric tank.

Flow parameters

The Reynolds number based on the inner pipe diameter is $Re_D = 10^4$. This value was found to match the need of studying turbulent jets, which are of industrial interest, without dealing with excessive fluid velocities or dimensions, and the necessity of limiting the computational requirement of the LES, considering that the whole three dimensional geometry is being numerically simulated.

The selection of water as working fluid restricted the value of the maximum velocity throughout the facility, specifically in the pipes, at $u < 1\ \mathrm{m/s}$. The operating conditions of the ambient pressure and temperature are equal to $1\ \mathrm{atm}$ and $293{,}15\ \mathrm{K}$, respectively. Neglecting the perturbation of water temperature due to small changes in the ambient temperature or the temperature raise caused by the fluid being continuously pumped in the primary loop during the measurements, the properties of the working fluid are:

Property	***Value***	***Unit [SI]***
p	101325	[Pa]
T	293,15	[K]
ρ	998	[kg m^{-3}]
μ	0.00101	[Pa s]

Table 2.1. Water properties for the primary and secondary loop.

With the help of the schematic CAD layout of the facility, shown in Fig.(2.7), we can better indicate where the test section is positioned with respect to the two main circuits of the facility:

- *Primary Loop*: This is where the jets are investigated. The working fluid, water, is pumped out of the atmospheric tank (D) into the pressurized tank (A) where it settles and separates through the 5 pipes (B) issuing into the rectangular plenum (C), and finally back to the starting point.

- *Secondary Loop*: Its purpose is to deaerate the working fluid. Water after being sucked up from the atmospheric tank (D), enters the depressurized tank (E) where it purifies from air removed by the compressor (F). The secondary pumps then inject the water back to the primary loop.

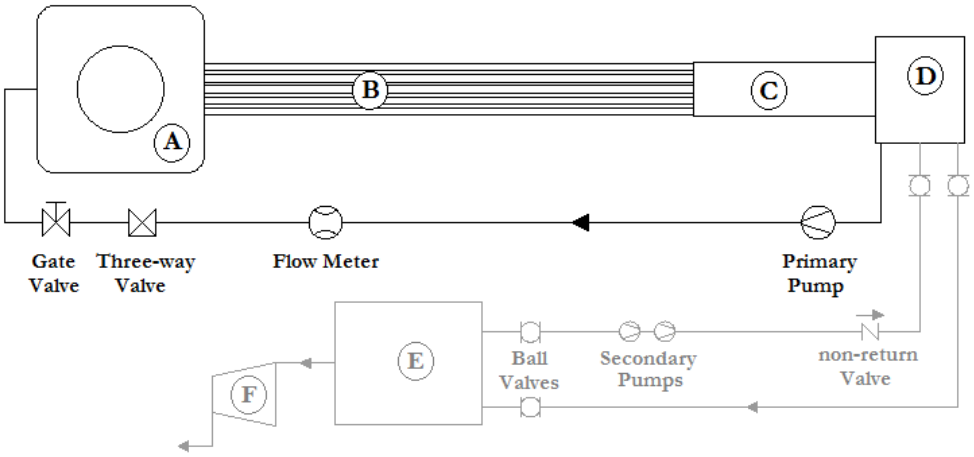

Figure 2.7. Schematics of the primary (black) and secondary loop (gray).

Let's now break down the facility to discuss the details of the remaining components.

2.1.2 Atmospheric and pressurized tanks

These two tanks play an important role in guaranteeing the correct mass flow rate and uniformity of the flow. Figure (2.8) is a schematic lateral view of the facility, with blue arrows representing the water direction, the dots indicating water out and the cross water in. Dimensions are expressed in meters with the width of tank (A) and (D) being 0.5 m and 0.32 m, respectively.

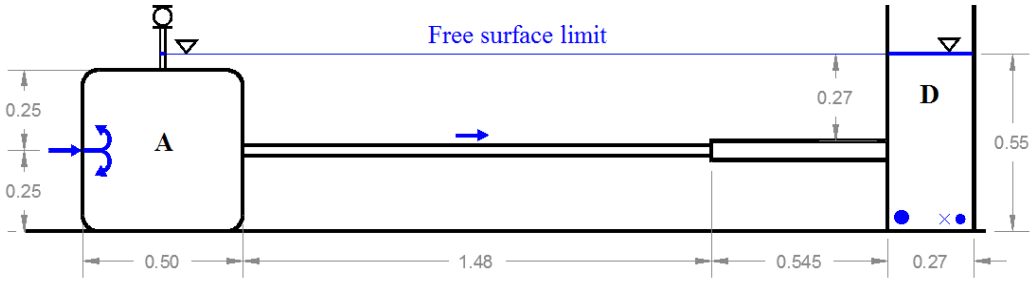

Figure 2.8. Schematics of the facility, lateral view. Dimensions in meters.

Uniformity

This parameter is particularly important for the pressurized tank. The fluid here must be as uniform as possible in order to guarantee the same mass flow rate in

each of the five pipes exiting the tank. In Fig.(2.9) a detail of the T-shaped conduits placed inside tank (A) in order to achieve this condition is shown. Water coming from the primary pump separates at the T-joint in two plastic conduits with blank union ends. Small holes were drilled to diffuse the fluid back toward the wall (see Fig.(2.8)). Due to the small velocities and the dimension of the tank, the flow is able to spread uniformly before reaching the five pipes.

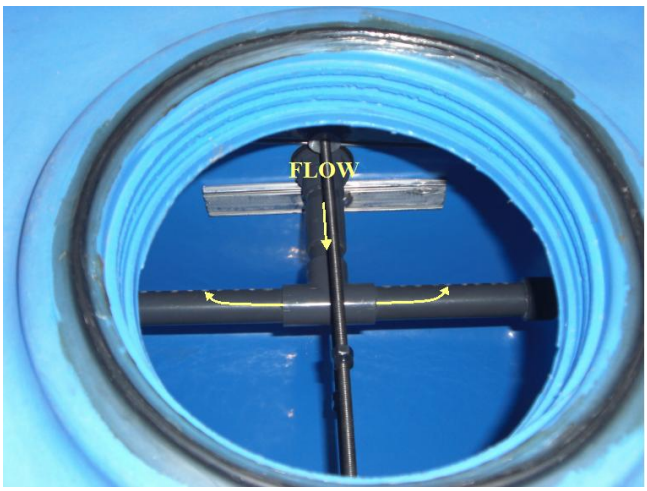

Figure 2.9. Inside detail of the pressurized tank.

When water exits the plenum, it settles in the atmospheric tank before being pumped back into the primary loop. Even in this tank the flow needs to be as uniform as possible. Aside from the honeycomb grid of the plenum, this condition is achieved by keeping the free surface limit away from the plenum outflow and the connections with the primary and secondary pumps at the bottom of the tank, as shown in Fig.(2.8).

Mass flow rate

The mass flow rate is kept constant inside the system. The primary loop is filled with water through the atmospheric tank until the free surface limit reported on Fig.(2.8). For the principle of communicating vessels, the free surface remains the same for both tanks. Tank (A) was purposely selected shorter than tank (D) in order to have its free surface, reached through a small connecting plastic pipe placed on the lid (Fig.(2.8)), above the top of the tank. Once the free surface limit is reached, the ball valve, that has been kept open during this process to maintain the same pressure in both tanks, is closed. The primary pump, having

ten speed levels, is then turned on to the level closer to the total mass of the primary circuit. The gate valve (Fig.(2.7)) is then used to adjust the mass flow rate to its specific value of $0.841\ \mathrm{kg/s}$, which guarantees the selected Reynolds number in each pipe. The reason for pressurizing tank (A) is the requirement to avoid an extended free surface that could create instabilities in the five-pipe inflow when the diffused water from the T-shaped conduits recirculates inside the tank, as previously described.

The five pipes are connected to tank (A) by five tank adaptors, whose inner discontinuities act as trip rings in forcing the transition to turbulence. In addition, the five pipes length, $70D$, is long enough to ensure the required fully developed turbulent condition when the flow enters the plenum.

For the reasons previously mentioned when describing the plenum structure, both tanks are firmly fixed to the wooden table to ensure a stable position during the measurements. Moreover, due to the deformability of tank (A), stainless steel screw tie rods connected to aluminum flat bars are inserted inside the tank (Fig.(2.9)) to prevent its eventual deformations caused by changes in fluid pressure.

2.1.3 Depressurized tank

Without deaerating the water, air dissolved in it would form bubbles in critical points of the loop, primarily the pump. In the kind of configuration analyzed, some of the bubbles issuing the confinement remain trapped in the top vortexes that generate during the expansion of the jets. Accumulated bubbles tend to join and form bigger and bigger air gaps that divert laser beams, interfering with the measurements.

Aluminum plates were welded together to create the depressurized tank of dimensions $44 \times 37 \times 37\ \mathrm{cm}$ (length x width x height) with a wall thickness of $1\ \mathrm{cm}$. This solid structure assured resistance to collapses caused by the pressure difference, along with avoiding rust that could flow in the primary circuit and keeping the tank relatively light.

Depressurization is realized with a $25\ \mathrm{W}$ Welch 2511 Dry Vacuum Compressor that removes air from the sealed aluminum tank keeping the pressure inside approximately around $0.3\ \mathrm{bar}$. This internal low pressure causes the water to flow into the tank and deaerate.

A detail of the deaerating tank is shown in Fig.(2.10). The red bouy inside the tank ensures the safety of the compressor. In fact, when the water rises too much, the buoy lifts as well and closes a valve, preventing excessive water to come into the depressurized tank. The secondary pumps then remove water from

the tank, lowering the free surface inside and allowing non-deaerated water to flow in again.

Once the water is purified from air, the secondary loop can be isolated and measurements can start without having to worry about bubble formation.

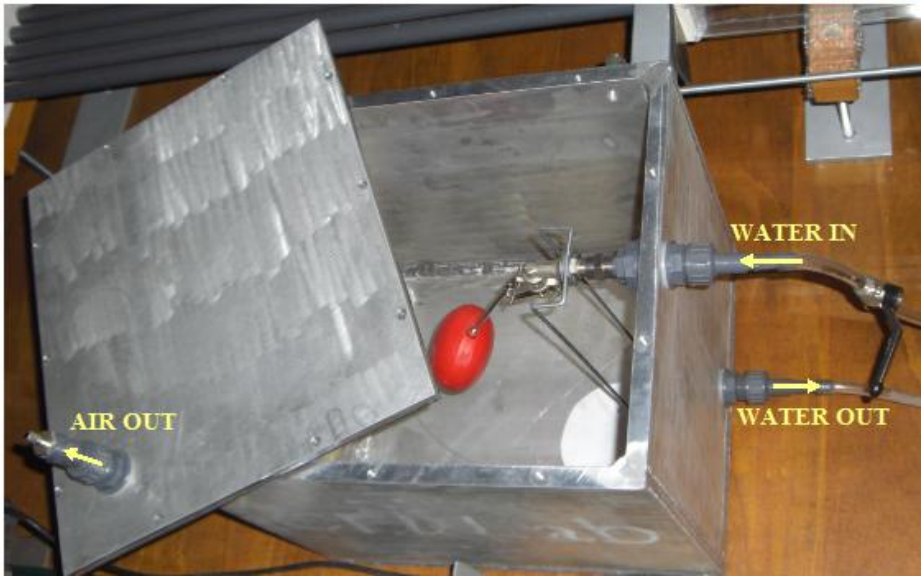

Figure 2.10. Detail of the depressurized tank.

The only part of the two loops that is in direct contact with the ambient air during the measurements is the atmospheric tank. For this reason, a floating lid is used, limiting the area of the free surface, hence the air absorbed by the deaerated water.

2.1.4 Primary and secondary pumps

The pumps used were selected to satisfy the required operating conditions: the primary pump permits the fluid to circulate in the primary loop with a constant mass flow rate, whereas the secondary pumps only need to extract the deaerated water from the depressurized tank and inject it into the primary loop. Both pumps are branded Grundfos, and have single-phase rotors electrically functioning at $50 \div 60$ Hz, $230 \div 240$ V for the primary pump and 50 Hz, 30 V for the secondary pumps.

Primary pump

The primary pump is a Grundfos MAGNA 25-100, with stainless steel shaft, plastic impeller and cast iron pump housing. This last component is the only one of the experimental facility that could rust and for this reason, the pump was tested before installation in order to assure that during its operation, rust does not form excessively. The possibility to easily empty the circuit via the three-way valve and the accessible pump housing, make it simple to clean when the pump is not operational. The primary pump is shown in Fig.(2.11) with its control panel, 1 1/2" pipe connections and the supporting structure firmly fixed to the wooden table.

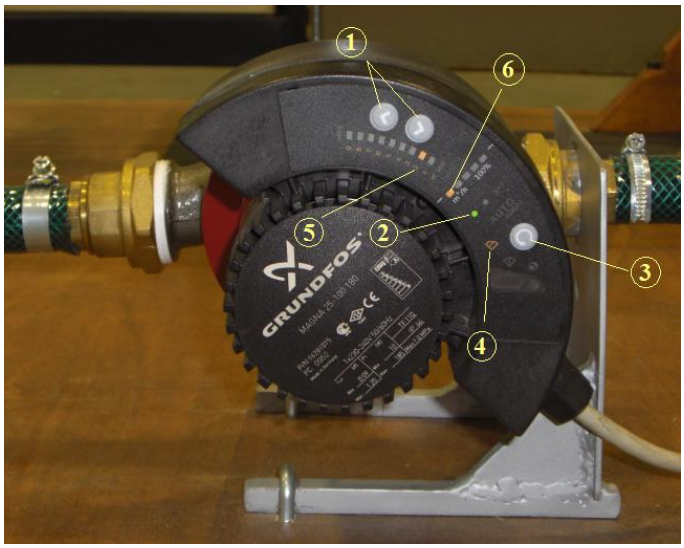

#	***Description***
①	Buttons for setting of head
②	Indicator light for operating indication
③	Button for selection of control mode
④	Light symbol of constant-pressure control mode
⑤	Light indication of head
⑥	Light indication of flow

Figure 2.11. Detail of primary pump.

The operating control mode of the pump was selected to be constant-pressure, which keeps the pump head constant. This mode is also recommended in systems with relatively small head losses, as in the analyzed configuration.

The operating curve of the pump working on constant-pressure mode is shown in Fig.(2.12), where the blue point indicates its operating condition during the measurements.

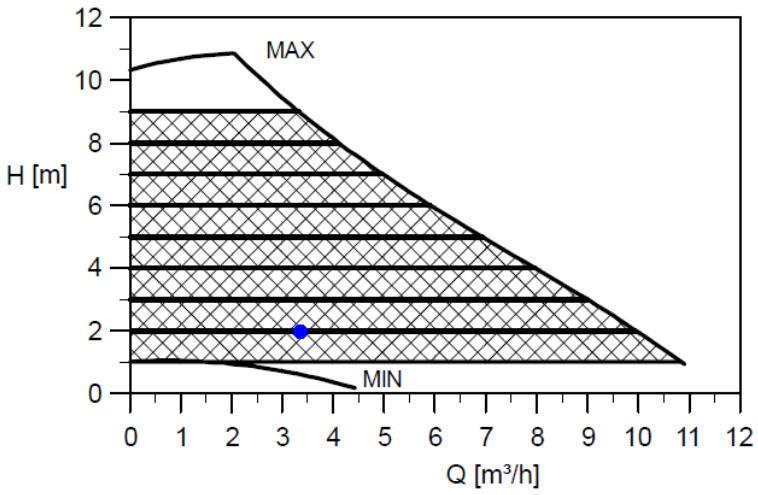

Figure 2.12. Primary pump operating curve.

The mass flow rate at the constant head value of two is an average registered from the digital indicator of the flow meter installed in the primary loop. This value, 0.948 kg/s, which is different from the mass flow rate needed, 0.841 kg/s, is adjusted by regulating the gate valve of Fig.(2.7). Several ten-minute tests, approximately the time used for measuring each velocity profile, were performed to verify that the average mass flow rate was respected, with variations of the order of 0.5%.

Secondary pumps

The secondary pumps are Grundfos UP 15-14B, with plastic impeller and brass pump housing. They are simply used to pump deaerated water from the depressurized tank to the atmospheric tank. A detail of the pumps mounted on the supporting table is shown in Fig.(2.13). The brass component between the pumps is a non-return valve, installed to avoid back flow due to the pressure difference in the two connected tanks. Each of them works at a power of 25 W with no possibility to change the operating conditions. The depressurized tank is positioned as high as possible (see Fig.(2.1)), within an accessible range, to facilitate the work of these two pumps.

Figure 2.13. Detail of the secondary pumps.

2.1.5 Flow meter

The flow meter used for mass flow rate measurements in this facility is a Toshiba electromagnetic flow meter, displayed in Fig.(2.14).

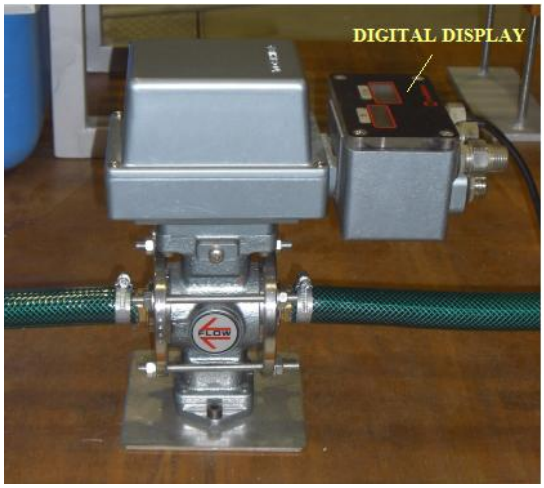

Figure 2.14. Detail of the electromagnetic flow meter.

On top of this device there are two digital indicators showing the instantaneous mass flow rate expressed in liter per second and the total liters measured. With this last indication it was possible to calculate the average mass flow rate during the measurements.

In order to fully take advantage of the accuracy given by an electromagnetic flow meter, it is necessary to maintain a sufficient distance from critical points of the loop that could generate turbulent instabilities. For this reason, this device

was installed 60 diameters downstream of the pump, without any abrupt change of direction in the connecting pipe, and 20 diameters upstream the three-way valve.

2.1.6 Supporting table

The whole facility is mounted on a wooden panel of dimensions 108 x 300 cm, painted with water-protective wax, supported by aluminum beams on which six adjustable feet allows a precise vertcal regulation. A spirit level was used to align the table horizontally, a preferable situation to facilitate the positioning of the measuring instrumentation. In addition, the height of the plenum from the floor, and as a consequence the table height, was selected in order to guarantee easy access for the jets analysis.

2.2 LDV set up

We briefly discussed about the physics of velocity measurements through a Laser Doppler Velocimetry in Par.(1.3) during the introduction of the different ways to investigate turbulence experimentally. This section begins with an overview of the LDV instrumentation followed by preliminary information on how to manage the laser's parameters. Finally, a description of measurement tests performed before analyzing the jets is proposed.

2.2.1 LDV instrumentation

The measuring instrumentation, which belongs to the Combustion Laboratory of Politecnico di Milano, is displayed in Fig.(2.15). The theoretical principles behind these components have been already explained in Ch.1. Here we simply define the characteristics relative to the specific apparatus adopted.

The laser source consists of a 2017 Spectra Physics Argon-Ion laser generator, capable of emitting a laser beam with a diameter of 1.4 mm with two main wavelengths of $\lambda = 488$ nm and $\lambda = 514.5$ nm. All the black flexible pipes coming in and out of the white boxes in Fig.(2.15) represent the connections with water and electricity. Electricity from the 50 Hz european grid is converted to 60 Hz through an autotransformer, before being used. The laser works at 208 V, 42 A with a nominal power of 5 W.

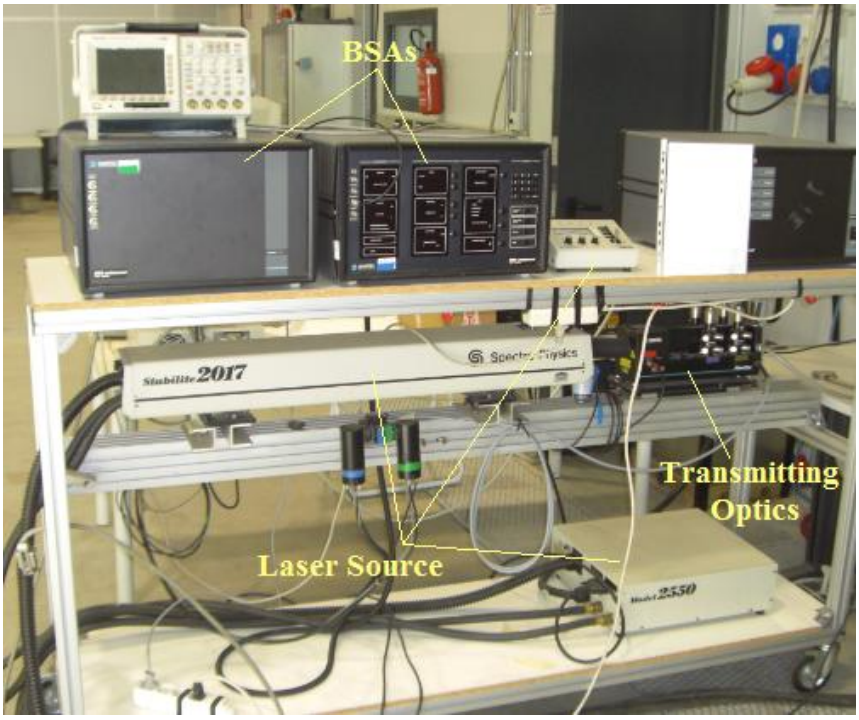

Figure 2.15. LDV instrumentation.

The transmitting optics, a Dantec Dynamics FiberFlow optical system designed for uses with Argon-Ion lasers, consists of a Bragg cell, fibre manipulators, optical fibres connections and a transmitting probe. Dantec Dynamics also provided for the Burst Spectrum Analyzers (BSA) used as signal processors for both the green and blue laser wavelengths.

A large amount of heat, approximately 15 kW, is to be removed to cool the components and therefore water must guarantee the requirements summarized in Tab.(2.2), otherwise the laser could shut down automatically.

Property	***Value***	***Unit [SI]***
Mass flow rate	$\min 1.4\ 10^{-4}$	[kg/s]
Pressure	$\max\ 6.9\ 10^{5}$	[Pa]
Inlet temperature	$283.15 \div 288.15$	[K]
pH	$7.0 \div 8.5$	$[-]$

Table 2.2. Water specification for the laser source.

Water is also filtered before entering the laser circuit to avoid possible obstructions caused by solid particulate matter.

2.2.2 Preliminary operations

The main parameters necessary to manage the instrumentation can be controlled by the software BSA Dantec installed in the computer. The following operations implemented in this software are the basic knowledge for a proper use of the LDV.

Moving the laser probe

The laser probe is easily maneuverable via the 5 m optical fibres cable that connects it to the FiberFlow. A high precision of its movements is achieved with a high resolution transverse system on which the laser probe is installed. Figure (2.16) represents an image of the laser probe mounted on the transverse system.

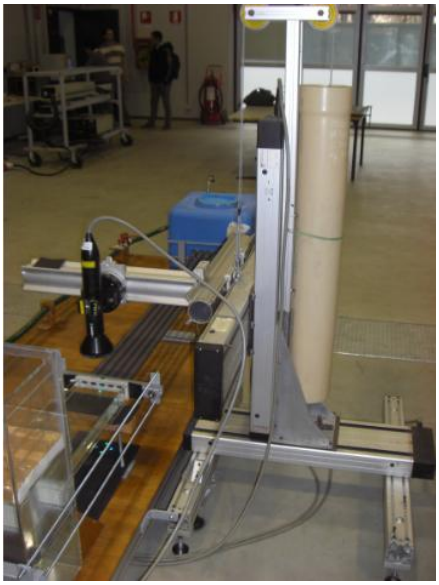

Figure 2.16. 3D transverse system.

The whole structure is firmly locked to the supporting table in order to avoid relative movements that could influence the measurements. Moreover, the laser was accurately positioned in a way that its movements are parallel to the coordinate system set on Fig.(2.4). The two components of the velocity measured are u_x and u_z, which correspond to the green and blue wavelength, respectively. The three dimensional axes of the transverse system, allow the investigation of the entire plenum, giving the possibility of analyzing the jets in several locations.

Setting optical parameters

Important optical parameters are represented by the fringe separation δ_f and number of fringes N_f, which can be evaluated as:

$$\delta_f = \frac{\lambda}{2\sin(\theta/2)}, \qquad N_f = \frac{8F\tan(\theta/2)}{\pi E D_L}, \tag{2.1}$$

where the former is used for the evaluation of the particle velocity, and the latter should be sufficiently high (usually $10 \div 100$) to obtain good results from the LDV equipment. Table 2.3 summerizes the optical parameters used throughout the measurements.

Optical Property	***Symbol***	***Value***		***Unit***
		Green	***Blue***	
Wavelength	λ	514.5	488	$[nm]$
Beam angle	θ	6.772		[deg]
Beam diameter	D_L	1.35		[mm]
Beam expander	E	1		$[-]$
Focal length	F	160		[mm]
Number of fringes	N_f	35		$[-]$
Fringe spacing	δ_f	2.182	2.069	[μm]
Probe volume	dx	0.078	0.074	[mm]
Probe volume	dy	0.658	0.624	[mm]
Probe volume	dz	0.078	0.074	[mm]

Table 2.3. Optical properties configuration.

Editing properties

The dynamics of fluids is well known to vary significantly according to the geometries investigated. Vortexes, streamline curvatures, swirls or even laminar flows are all situations in which fluid particles behavior changes considerably. The experimental technique used to analyze these flows must be able to adjust to every condition in order to be accurate. In particular, the kind of geometry here investigated experiences high velocity gradients in very limited regions, especially where the five jets expand and interact. The principal parameters to set, which are also the ones found to be most effective for the current

investigation, are the velocity range, voltage of the PhotoMultiplier (PM), and the laser power.

The Doppler frequency is not the only one carried along in the current pulse. There are several sources of unwanted light that may reach the photodetector and are then transformed in frequency noise [25], e.g. light reflection of windows. As we mention in the previous paragraph, the electric signal is filtered before being processed. Noise can be minimized by selecting, through the BSA software, a limited bandwidth in which the desired range of velocities is confined. A preliminary CFD analysis was performed to estimate the velocity field in the plenum for a better selection of the velocity range.

The second parameter that greatly influences data acquisition is the voltage of the photomultiplier. It is related to the detection threshold previously discussed since increasing the voltage means having more bursts that pass the minumum detection level, increasing both the noise and the data rate. Aside from the possibility of regulating the high voltage of the PM from the BSA software, it is also possible to turn it on or off.

Table (2.4) summarizes the previous parameters used during the analysis of the plenum, based on the distance in diameters along the x axis. Note that the hypothesized velocity range is represented in the BSA software as a Range-Center, which is the mean value, and a Range-Span corresponding to the amplitude.

Property		***1D***	***4D***	***7D***	***13D***	***20D***	***Unit***
High Voltage	*Green*	952	952	952	1000	1000	[V]
	Blue	952	952	952	952	952	
Range-Center	*Green*	0	0	0	0	0	[m/s]
	Blue	0	0	0	0	0	
Range-Span	*Green*	8.37	2.18	2.18	4.36	4.36	[m/s]
	Blue	4.14	4.14	2.07	2.07	2.07	

Table 2.4. Data acquisition properties.

While the previous parameters are to be specified at the beginning of the measurements and cannot be changed during it, the laser power, which is not controlled by the BSA, can be regulated at anytime. This regulation acts directly on the laser generator by increasing or decreasing the intensity of the laser source which, in turn, affects the data rate. The power of the laser source was kept constant through all the measurement at a value of 5 W.

Data sampling

Two last parameters to be defined before a measurement are the maximum number of bursts and the maximum measuring time per point. As previously mentioned, the fluid dynamic configuration of these five parallel jets makes it hard for the seeding particles to distribute uniformly through the plenum. Critical points for the seeding particles are in the regions between the jets, along the z axis, where the data rate significantly decreases with respect to the jet centerline. After a certain distance from the origin, the effect of the jets starts to diminish and the seeding particles are more uniformly distributed.

During the measurements, the number of bursts per point is, on average, around 2500, with the exception of few points in the critical regions in which this number is not less than 600. In Ch.4, these samples will be statistically analyzed to evaluate the precision of the measurements.

2.2.3 Opening measurements

Several measurements were performed before starting the data acquisition in the regions of interest, in order to set the position of the origin.

Tracer

In order to begin the measurements, the fluid must be seeded with some kind of reflecting particles that scatter light from the laser back to the receiving optics. It is appropriate to use particles whose density is similar to that of the working fluid to have them floating uniformly through the entire volume of the primary loop. Dantec Dynamics provides S-HGS hollow glass spheres with a diameter of 10 μm, with a thin silver coating for increased reflectivity, which are adequate when the working fluid is water.

Laser beams position and spatial references

Given the dimension of the seeding particles, the flux of light they reflect is very low. On the other hand, when the laser light is scattered from a large surface, such as the quartz glass of the plenum, the flux of light would increase significantly. If this happened during normal measuring conditions, when the laser intensity is high, the beam reflected could damage the photomultiplier. For this reason it is important to keep the laser beams at a safety distance from the top surface during measurements (Fig.(2.17)).

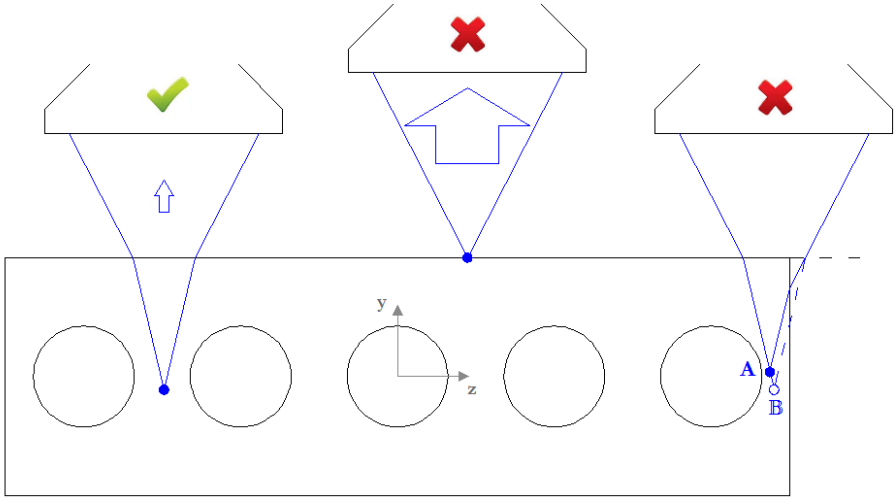

Figure 2.17. Dos and don'ts during LDV measurements.

Beams of light emitted in free space travelling through a different material, slightly change their speed and as a consequence their direction, a phenomenon called refraction. If we take a look at Fig.(2.17), laser beams coming from the left probe undergo a symmetrical refraction when entering the plenum filled with water. Approaching the lateral wall, one of the beam enters the plenum from a different position, forming the probe volume (A). The broken lines represent the same configuration as in the case of the left probe, where the probe volume (B) is obviously in a different position than (A). In addition, another risk with lateral walls is when the probe volume is moved through the lateral wall thickness, causing a possible increase of reflection and damage of the PM. Approaching lateral walls it is important to keep both beams inside the plenum. Based on these considerations, the first point near the wall is at a distance of 3.5 mm and 2.6 mm, for the z and y axis, respectively.

Another consequence of refraction is that, when the probe volume is inside the plenum, a displacement Δy of the laser probe corresponds to a movement of the probe volume of $\alpha \Delta y$, with α being a constant depended on the refraction. Establishing a new vertical coordinate y' that represents the displacements in the y direction of the probe volume, we can write:

$$\Delta y' = \alpha \Delta y \qquad (2.2)$$

The origin of this new coordinate is defined from the consideration that the maximum velocity along the y axis is coincident with the origin of the y axis itself. Measuring several points at $x = 0.0212$ m, $0.0106 < y < -0.0106$ m, $z = 0$ which is still in the core region, the u_x velocity profile

obtained and interpolated is used to set the origin of the y' coordinate at its maximum, as shown in Fig.(2.18).

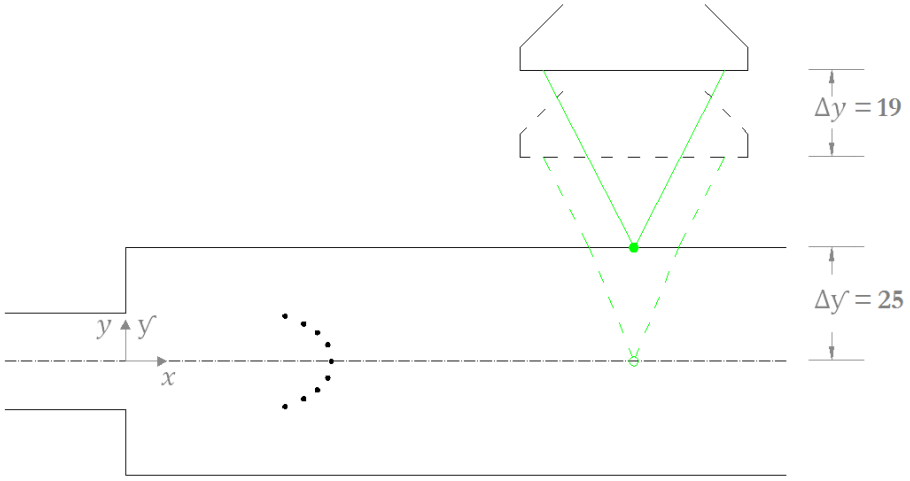

Figure 2.18. Coordinate system inside the plenum.

Starting from the origin of y', which is also the origin of y, the laser probe needs to move $\Delta y = 19$ mm to permit the probe volume to cover the entire plenum half-height $\Delta y' = 25$ mm. Given these values, the constant of proportionality becomes:

$$\alpha = \frac{\Delta y'}{\Delta y} = 1.3158, \qquad (2.3)$$

which is used to evaluate the position of the probe volume knowing the displacement of the laser probe. This test was performed with the PM off and the laser at its minimum power in order to avoid possible dangerous reflections from the top surface, as previously mentioned.

Chapter 3

Numerical Modelling

In this chapter, a description of the numerical parameters set up is proposed for both URANS and LES simulations. The domain meshed includes the five pipes and the whole three dimensional plenum with the dimensions of Fig.(2.4). For both URANS and LES models, unstructured meshes were generated with the Gambit 2.4.6 preprocessor for grid generation. Each model is described in the following paragraphs. A first look at the grid generation strategies gives an idea of the required computational resources, especially considering that the whole three dimensional domain is modelled. Secondly, the numerical models used in this thesis are first tested for the prediction of a single pipe flow, for which experimental and DNS data are available [35, 36], in order to guarantee a certain accuracy of the velocity and turbulence profiles of the five jets before entering the plenum and interacting. The numerical parameters that led to obtain these results are then used for the complete geometry.

3.1 URANS approach

This paragraph addresses the information about the parameters set for the URANS simulations, describing the discretization and numerical settings, ending with a periodic pipe test for the models.

3.1.1 Mesh parameters

The numerical domain represents the hole three-dimensional plenum including a $10D$-long pipe for each jet. Figure (3.1) shows the subdivision of the domain into three main volume-type:

① Defines all the ten pipe volumes, five of which are the continuation of the external pipes inside the plenum, colored in green;

② Bottom part of the plenum, colored in cyan;

③ Top part of the plenum, colored in magenta. Displayed transparent to show the extension of the pipes inside the plenum.

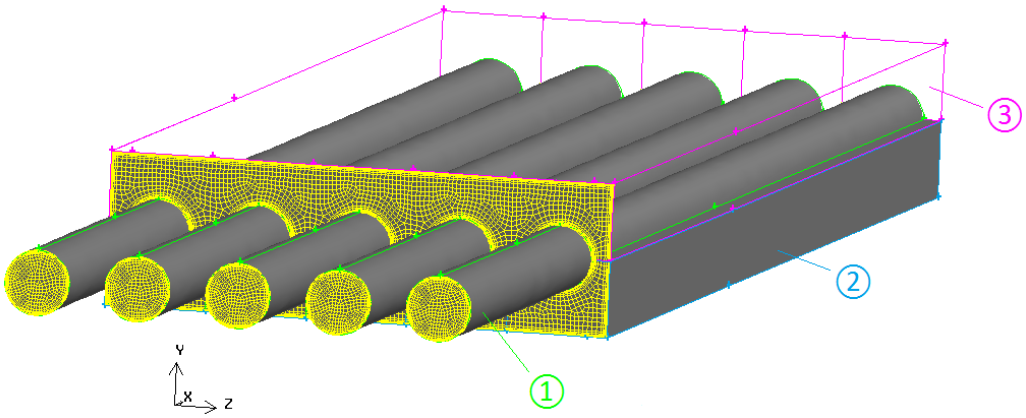

Figure 3.1. Subdivision of the three-dimensional domain into volumes.

The faces meshed in the figure, are then extruded through each volume-type respectively, with an axial spacing that is finer where the jets expand (approximately $10D$) and then coarsens in the rest of the plenum. The resulting mesh is composed of unstructured hexaedral cells, with a grid resolution at the walls, being it $y^+ \approx 1$, that allows for a two-layer boundary condition, which is a preferred choice considering the complexity of the flow and the necessity to better solve the vortexes caused by the expansion of the jets. The size ratio of the mesh is limited to values less than 10% with the vast majority of the domain and few exceptions in the boundary layers with values of 50%, and the equiangle skewness limited to a value of 0.3 for the 97% of the mesh cells. A detail of the mesh is shown at the end of this chapter, Fig.(3.5), where it is compared with the LES grid.

Based on this mesh scheme, three grid refinements are adopted in the next paragraph for a grid-convergence study, a common approach to quantify the numerical uncertainty.

3.1.2 Grid sensitivity analysis

Roache proposed the calculation of the Grid Convergence Index (GCI) as an indicator of how far away the solution is from the numerical asymptotic value [37]. Three levels of grid refinement are required to apply the GCI procedure. Hereafter, a description of the steps for the grid convergence study is treated.

Based on the objective of this thesis, it is appropriate to evaluate the GCI in a point of the domain interested by the expansion of a jet, $(0.2424; 0.0125; 0.033)$, which represents a point in the shear layer of the jet on the right side of the central jet, at $x = 2D$ from the plenum inlet. In this region, turbulence reaches higher levels with respect to the rest of the plenum,

and therefore the turbulent kinetic energy (k) is an appropriate physical parameter. Table (3.1) indicates the information regarding the three unstructured grids analyzed along with the results of the velocity computed from the solutions.

Grid	***Index***	***Cell Number***	$\boldsymbol{k}$ $[\boldsymbol{m^2\ s^{-2}}]$
Fine	1	$2.27\ 10^5$	0.01585
Medium	2	$1.27\ 10^5$	0.01579
Coarse	3	$7.07\ 10^4$	0.0157

Table 3.1. GCI grid parameters.

Based on these values, the grid refinement ratio is:

$$r = \left(\frac{N_1}{N_2}\right)^{1/\mathcal{D}} \approx \left(\frac{N_2}{N_3}\right)^{1/\mathcal{D}} \approx 1.21, \tag{3.1}$$

where N is the total number of cells used for the grid, and $\mathcal{D}$ is the dimension of the flow domain, which is $\mathcal{D} = 3$, for the three-dimensionality of the domain here considered.

The order of convergence p can be directly evaluated based on the results of Table (3.1) and Eq.(3.1) as:

$$p = \frac{\ln\left(\frac{f_3 - f_2}{f_2 - f_1}\right)}{\ln r} = 1.84, \tag{3.2}$$

where f_i are the values of the discrete solution. Applying now the Richardson extrapolation generalized for a p-th order method, neglecting the third-order and higher terms, we can calculate the continuum value of the solution, i.e. the value of f when the grid spacing h is equal to zero:

$$f_{h=0} \cong f_1 + \frac{f_1 - f_2}{r^p - 1} = 0.0159. \tag{3.3}$$

Knowing that the Grid Convergence Index can be computed as:

$$\mathrm{GCI}_{ij} = \frac{F_s \left|\frac{f_i - f_j}{f_i}\right|}{r^p - 1}, \tag{3.4}$$

and keeping into account that for a three-grid convergence study the safety factor is $F_s = 1.25$, we can check if the solution is in the asymptotic range of convergence by:

$$\frac{\mathrm{GCI}_{23}}{r^p \mathrm{GCI}_{12}} = 1.003, \tag{3.5}$$

whose value, approximately equal to one, means that the solutions are well within the asymptotic range of convergence.

Based on these results, the medium grid is used for the comparison of the numerical URANS models, halving the number of cells with respect to the fine grid while still preserving a good approximation of the Richardson extrapolation.

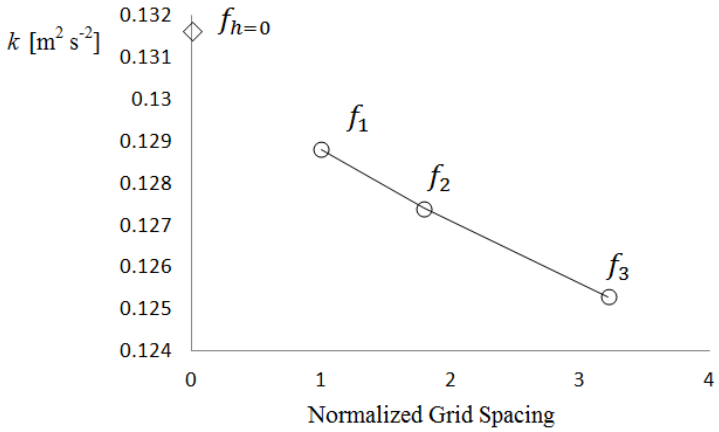

Figure 3.2. GCI graphical representation.

Figure (3.2) shows how the discrete solutions of the three grids converges to the Richardson extrapolation solution, based on a grid spacing equal to zero, as the refinement increases.

3.1.3 Computational settings

In addition to the numerical models introduced in Ch.1, several modifications of them, present in the solver ANSYS Fluent 12.1.2 [38], are added to the comparison. All the URANS models used can be summarized as follow:

- Linear Eddy Viscosity Models:

- k-ε Standard: proposed by Launder and Spalding in 1972 [39], it is the most used in practical engineering problems.
- k-ε RNG: derived by the instantaneous NSE using a statistical technique, it was proved more accurate and reliable than the previous one in flows featuring streamline curvatures and vortexes [40].
- k-ε Realizable: includes a new equation for the dissipation of energy in order to address the deficiencies of the round jet anomaly [41]; it is the only one that satisfies the realizability of the Reynolds stresses.
- k-ω SST: this variation unifies the accuracy of the standard k-ω near the wall with the robustness of the k-ε model in the far field [42].

- Linear Reynolds Stress Model: No longer part of the isotropic eddy viscosity hypothesis, it has more potential in predicting complex flows than the previous models by directly solving transport equations for the Reynolds stresses [43].

- Non-Linear Eddy Viscosity Model: A third order formulation for the Reynolds stresses implemented in the code via user-defined functions that improves the prediction of secondary motions and separation. This model is tested with two different damping functions [32]:

  - Damped E
  - Damped W

Numerical settings adopted for the previous models are essentially the same. The fractional step method, available when the non iterative time advancement scheme is selected, was chosen for the pressure-velocity coupling because of its much faster calculation of each time step, which reduces the computational time significantly, without compromising the accuracy of the calculation. Spatial discretization for the momentum, pressure and turbulent quantities is calculated with a second order accuracy, and so is the transient formulation. The flow was initialized as quiescent, except for the two non-linear models that required a developed flow field for stability reasons. Enhanced wall treatments implemented in the code are used for the near-wall region. Based on the refinement of the mesh, they select either the wall fuctions or the two-layer approach. Considering that in all the domain the condition of $y^+ \approx 1$ is respected at the walls, the latter is adopted. Since the unsteady equations are solved, a time step must be chosen. The Courant-Friedrichs-Lewy condition is used for the determination of a time step that limits the Courant number to one in the overall domain. Numerical settings for the URANS simulations are summarized in Table (3.2).

URANS Numerical settings	
Solver	Segregated
Temporal Discretization	Implicit – II Order
Spatial Discretization	
Pressure	II Order Upwind
Momentum	II Order
Gradient	Green-Gauss Cell-Based
Pressure-Velocity coupling	Fractional Step
Time Step	Unsteady, $\Delta t = 4\ 10^{-3}$ s

Table 3.2. URANS numerical settings.

It is important to point out that in the case of the non-linear models, their implementation did not allow the choice of the fractional step as the Pressure-Velocity algorithm, and the PISO algorithm was then used, with the only disadvantage of requiring a longer computational time for the convergence of the results.

Periodic pipe test case

With the settings previously mentioned, a periodic pipe is used to test how each model predicts the flow field before entering the plenum. Figure (3.3) shows the non dimensionalized velocity and turbulent kinetic energy profiles.

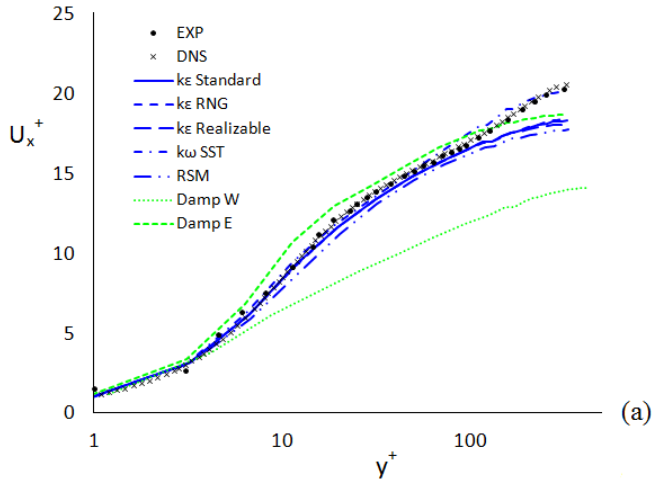

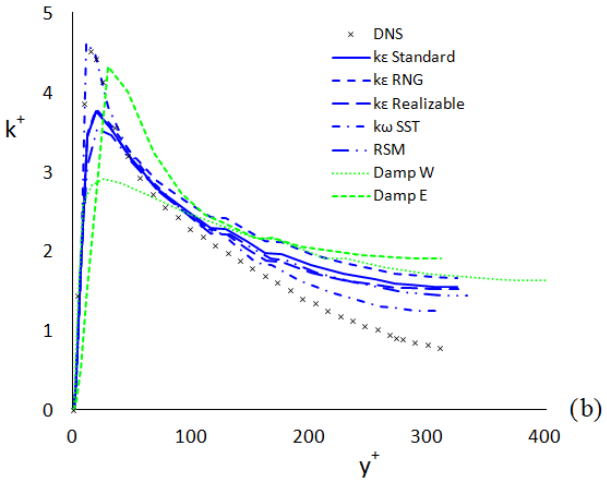

Figure 3.3. URANS single pipe velocity (a) and turbulence (b) profiles.

The k-ω SST is the most suited of all models for predicting the flow in a pipe, in fact, as results demonstrate, it represents experimental and DNS profiles better than all the other models. Models of the k-ε family and RSM all behave very similarly, especially for the velocity profiles, where they practically overlap. The unsadisfactory prediction of the non-linear model damped W respects the overestimation of the losses through the pipe, therefore influencing the friction velocity used for the nondimensionalization of the profiles. A change in the damping function, Damp E, seems to better represent both the velocity and turbulent profiles even though the results do not excel over the simpler linear models.

The fully developed velocity and turbulent profiles derived in each periodic test, are then set as inlet boundary conditions for the five pipes. As for the outlet condition, atmospheric pressure was selected, which is a reasonable approximation considering that the plenum in the experimental facility is connected to the atmospheric tank.

3.2 LES approach

The computational requirement necessary to run LES simulations is significant with respect to the URANS modelling. For this reason it is important to assess as well as possible the numerical parameters.

3.2.1 Mesh parameters

Contrary to the previous case, a refinement on the grid size in LES implies capturing smaller scales of turbulence, with the obvious outcome of modifying the results. Since the purpose of a LES is to reduce the computational requirement with respect to directly simulating the whole range of turbulence scales, the grid size does need not be too small. A set of parameters that were proved valid for a variety of cases [34] can be defined, for a pipe geometry, as:

$$\Delta x^+ = \frac{\Delta x}{D} Re_\tau < 50 \div 100, \tag{3.6}$$

$$\Delta \vartheta^+ = \frac{\pi}{N} Re_\tau < 15 \div 45, \tag{3.7}$$

$$\Delta y^+ = \frac{u_\tau \left(D/2 - r\right)}{D} Re_\tau < 1 \tag{3.8}$$

where N is the number of nodes along the pipe diameter, and Re_τ is the Reynolds number based on the friction velocity:

$$Re_\tau = \frac{u_\tau \rho D}{\mu}. \tag{3.9}$$

The friction velocity, Eq.(1.9), is determined from the evaluation of the wall shear stress as:

$$\tau_w = \frac{f}{2} \rho {U_{bulk}}^2, \tag{3.10}$$

where f is the friction coefficient. It is important to notice that the Re_τ used for the evaluation of the grid spacing is relative to the singular pipe for the whole geometry, which allows for a potentially higher resolution of the turbulent scales in the expansion region of the jets.

Figure (3.4) summarizes the dimensionless parameters used for meshing the LES numerical domain.

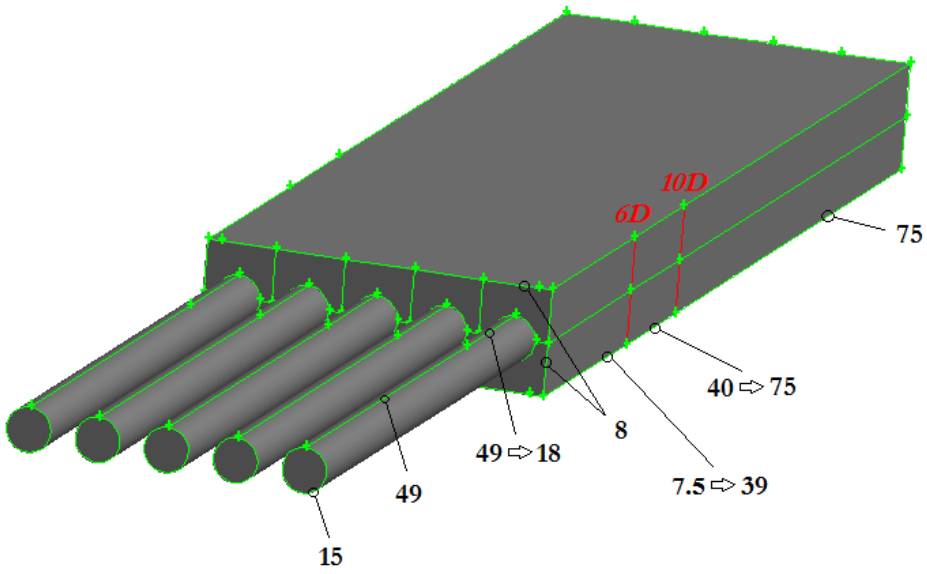

Figure 3.4. LES dimensionless meshing parameters.

The procedure for generating the grid is the same as the one followed for the URANS grids, with a total number of cells needed to mesh the entire geometry, five jets included, equal to $1.69\ 10^7$.

A comparison of the grids used for the numerical simulations, is shown in Fig.(3.5), which represents a cross section of the plenum at $x = 0$.

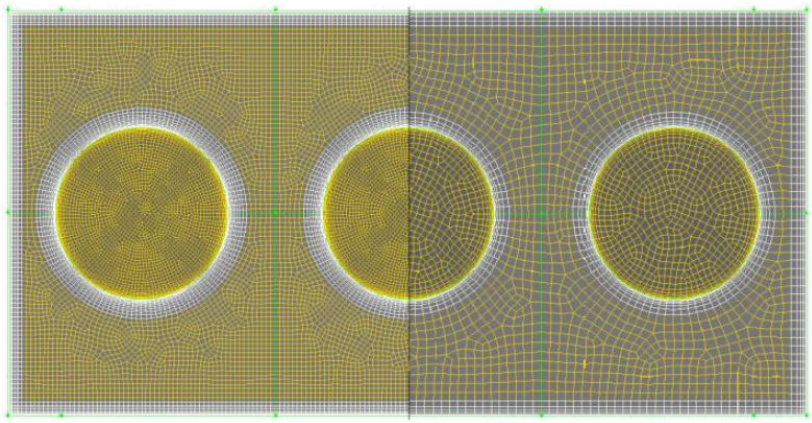

Figure 3.5. Comparison of the LES (left) and URANS (right) meshes

This comparison highlights the substantial increase in the computational need between a LES a URANS simulation.

3.2.2 Computational settings

Even in LES the outcome of the simulation is sensible to the computational settings, and in particular to the boundary conditions. Given the substantial increase of the computer power need to run a simulation, it is important to carefully evaluate the proper settings before starting the actual simulation.

Pipe flow test case

Based again on the idea that the flow in the pipes must be simulated as accurately as possible, a precursor analysis on the pipe flow via LES was performed. A first analysis on a five-diameter long periodic pipe configuration allowed to assess the influence of the mesh type, structure vs. unstructured, pressure interpolation scheme, PRESTO! vs. II Order, and gradient computation method, Green-Gauss Node-Based (GGNB) vs. Least Squares Cell-Based (LSCB) using the structure configured in Fig.(3.6):

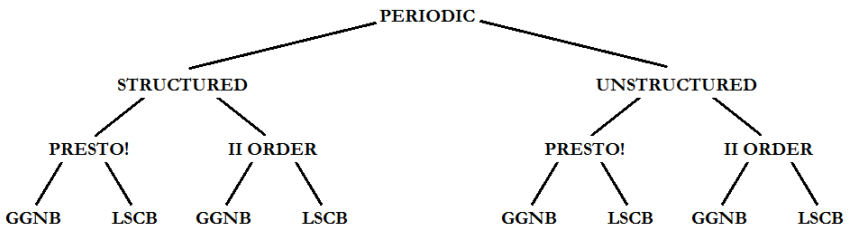

Figure 3.6. Structure of the precursor LES analysis.

Results showed a sensitivity on the pressure interpolation scheme solely. PRESTO! and LSCB were selected for the subsequent tests, where the subgrid scale models and mesh refinement, always on the periodic geometry, are investigated. On one side, the Smagorinsky dynamic model resulted to better solve the subgrid scales rather than the WALE and Dynamic Kinetic Energy models, also implemented in the code; on the other side, a refinement on the grid led to an improvement of the results that, however, was not worth the thrice computational effort when reflected on the five-jet domain.

A second analysis is performed to evaluate the influence of the inlet boundary conditions in a $20D$ long pipe. Fully developed turbulent profiles from the RSM model, which include the RMS turbulent profiles, are the ones used as inlet condition for the LES calculation. In addition, we also need to assess which method of generating inlet turbulent fluctuations associated with the inlet profiles is the most accurate, compared to the periodic case, and effective, requiring the minimum pipe length possible. Out of the two algorithms tested,

Vortex Method and Spectral Synthesizer, the former is found superior in both aspects required, with profiles matching the periodic case at $15D$. At the outlet, the outflow boundary condition was chosen out of the possible selections present in the solver, because is well suited for flows with constant density which appear to have an exiting flow close to a fully developed condition. Results of the precursur LES simulations are displayed in Fig.(3.7).

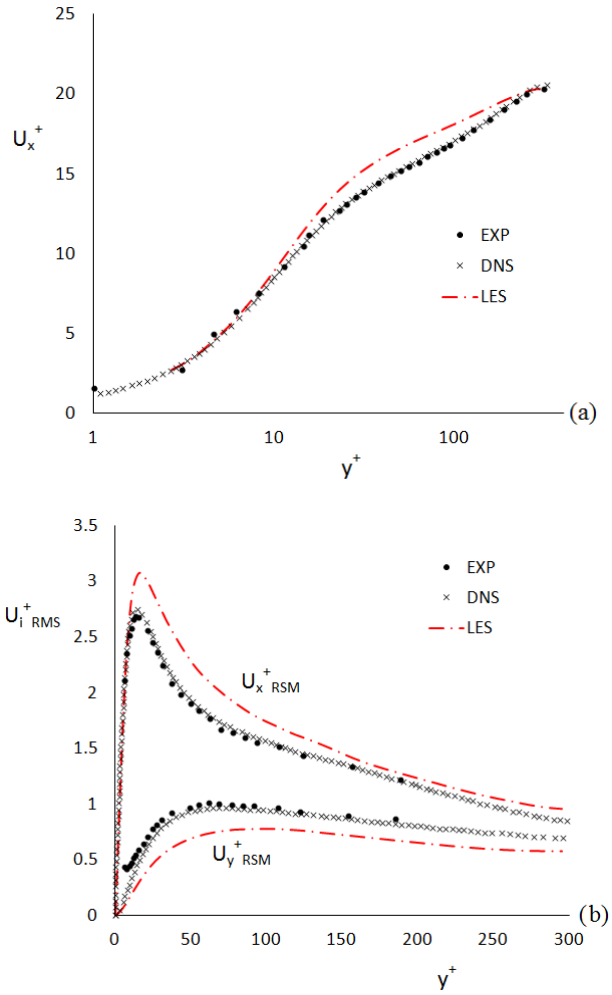

Figure 3.7. LES single pipe velocity (a) and turbulence (b) profiles.

The configuration selected out of this precursor LES analysis that offsets computational requirement and accuracy of the results is summarized in Table (3.3). These parameters are the ones set for the simulations of the whole five-jet geometry.

LES Numerical settings	
Solver	Segregated
Temporal Discretization	Implicit – II Order
Spatial Discretization	
Pressure	PRESTO!
Momentum	Bounded Central Differencing
Gradient	Least Squares Cell-Based
Pressure-Velocity coupling	Fractional Step
Time Step	Unsteady, $\Delta t = 6.5\ 10^{-4}$ s
Fluctuating velocity	Vortex Method

Table 3.3. LES numerical settings.

Additional information on this analysis can be found in [44].

Chapter 4

Results

This chapter is exclusively dedicated to the results of the experimental and numerical investigations on the parallel jets domain. The chapter is structured by introducing the methods for validation of both experimental and numerical data, and then carry on with the comparison of the results. Even in this case, validation will be separated in two different paragraphs concerning URANS and LES models.

4.1 Measurements validation

Before starting the analysis of the jets there are a couple of considerations that need to be taken into account, namely, assessing the statistical errors associated with the experimental results and mass flow rate in each pipe.

4.1.1 Experimental uncertainty

When approaching any kind of experiment, errors are inevitable. The two sources of uncertainties in measurements are the systematic and random errors. The former are associated with the instrumentation, while the latters are related to the fluctuating nature of a phenomenon, such as turbulence. With the information available from manifacturer's specifications and calibration reports, the systematic error was found to be $\sigma_{sys} \approx 1\%$. The standard error associated with the random uncertainty is defined as [45]:

$$\sigma_{ran} = \frac{a_{RMS}}{\sqrt{N}} \tag{4.1}$$

where N is the number of samples for each point, and a_{RMS} is the root mean square of the random variable being measured. Calculating the statistical error for the values obtained from the measurements in the plenum, we find that the maximum statistical error is positioned along the z axis profile at a distance of $x = 4D$, as shown in Fig.(4.1). Values are normalized by the mean velocity in the plenum $\overline{U}_{ch} = 0.102\ \mathrm{m/s}$, evaluated from the total mass flow rate, in order to have a value additionable to the systematic value found before.

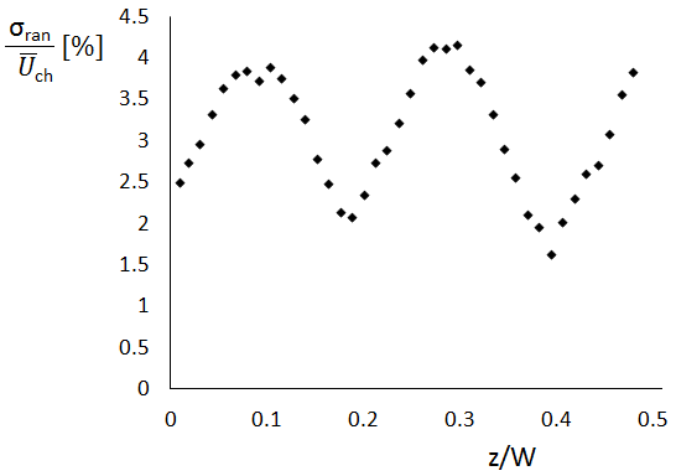

Figure 4.1. Normalized statistical error profile at $x = 4D$.

The peaks represented in this graph are influenced by the fact that being the jets so closely spaced, the regions in between them lack of seeded particles. This region is associated with the highest random error.

The two sources of errors are then combined with the law of propagation of uncertainty [46]:

$$\sigma = \sqrt{\sigma_{ran}^2 + \left(\frac{\sigma_{sys}}{\sqrt{3}}\right)^2} \tag{4.2}$$

where it was assumed a rectangular statistical distribution for the systematic uncertainty, and an equal contribution of the two sources of error in evaluating their summation. Assuming a normal distribution of the standard uncertainty σ, the confidence interval can be evaluated as:

$$CI = U \pm 2\sigma \tag{4.3}$$

where U is the mean velocity of a single measurement. Its meaning is to be interpreted as a velocity span in which the mean value will lie everytime the measurements are repeated in the 95% of the cases.

4.1.2 Mass flow rate distribution

A special consideration must be given to the distribution of the flow through the five jets. In Ch.3, we mentioned that the five pipes are connected to the

pressurized tank in which water is distributed uniformly. By measuring the streamwise velocity profiles at the location closest to the jets intake, specifically at $x = 1D$, we can somehow prove that the total mass flow rate is equally divided among the five jets. Figure (4.2) and Fig.(4.3) can fairly demonstrate this statement. The fact that the velocity peaks line up at the same level, and the very similar shape of the profiles when they are overlapped, as shown in Fig.(4.3), can be seen as an acceptable sign of the equal division of the mass flow rate through the five pipes.

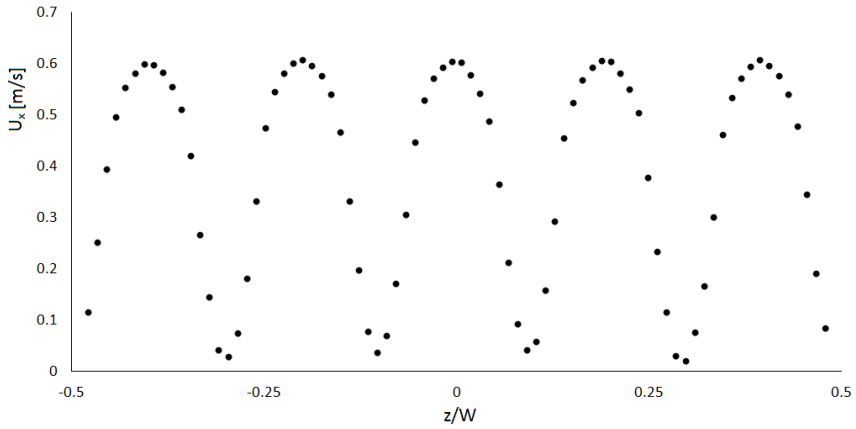

Figure 4.2. Measured velocity profile at $x = 1D$.

Additional information form Fig.(4.2) can be given considering that the maximum velocities of the centerline experimental values are in close accordance with the ones found in the periodic pipe, ≈ 0.603 vs. $0.589\ \mathrm{m/s}$, respectively, proof that at $x = 1D$ we are still in the potential core region of the jets.

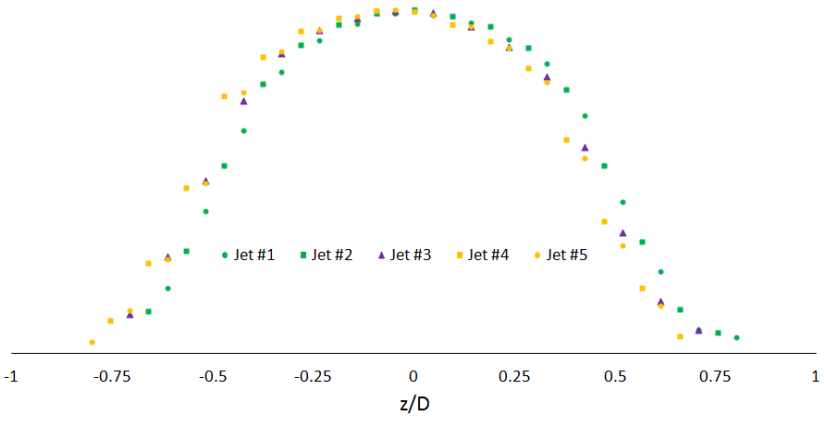

Figure 4.3. Measured velocity profile at $x = 1D$, overlapped.

Aside from the similarity of the profile, a noticeable shift of the lateral jets with respect to the central one also appears. In particular, Jet #4 and Jet #5 (Fig.(4.6)), which are on the right side of the central jet, tend to lean to the left whereas Jet #1 and Jet #2, on the left side of the central jet, tend to lean to the right. This phenomenon can be attributed to the attraction of the lateral jets to the central one due to entrainment, similar to the case of the three-jet discussed in the introduction [16].

4.2 Computational convergence

As in the case of experimental measurements, we need to validate the numerical results, assessing the convergence of the physical and numerical parameters. Once again both the URANS and LES cases will be considered separately.

4.2.1 URANS convergence

Numerical convergence was achieved for each URANS model used by keeping the residuals of both velocity and turbulence at a low value. In particular, the maximum continuity residuals are of the order of 10^{-5}, while for the turbulence residuals these order of magnitude is lower than to 10^{-7}. In addition, physical properties were evaluated in several points around the domain for both turbulence and velocity, and they all show a development like the one displayed in Fig.(4.4) for the U_x velocity in the point $(0.106; 0; 0)$ which is in the centerline of Jet #3 at $x = 5D$.

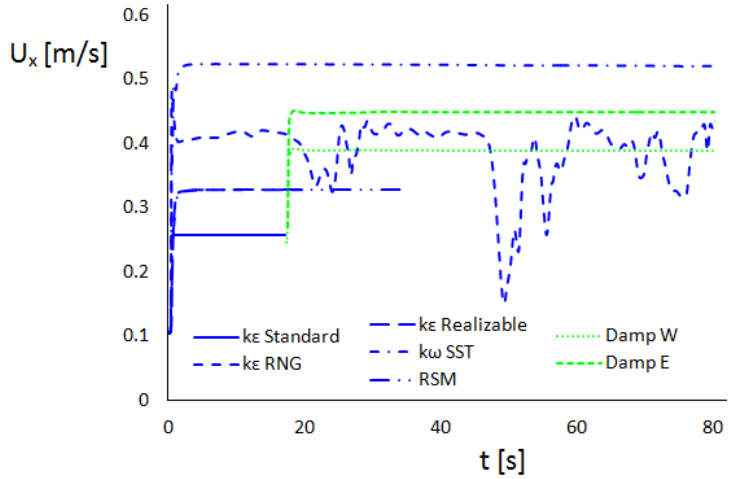

Figure 4.4. URANS physical convergence at $x = 5D$.

From the figure above it can be noticed that the non linear models, corresponding to the green lines, start from the ending point of the k-ε Standard model as part of their requirement of having a developed flow field as initial condition for the stability of the numerical methods. In addition, only one of the models, the k-ε RNG shows instabilities, primarily in the central jet. These are found to be unphysical, therefore this model will be omitted from now on from the comparison with experimental data.

4.2.2 LES convergence

In the case of LES, the numerical residuals correspond solely to the continuity and the instantaneous components of the velocity vector. The former experiences a residual in the order of 10^{-2} while the latters are three order of magnitude smaller.

Considering that the instantaneous components of the velocity vector are calculated at each time step, in order to compare the LES results with the experimental ones, data sampling must be included for the calculation of the mean and RMS velocity profiles. The parameter used to assess the proper starting point of the data sampling corresponds to the kinetic energy of the instantaneous velocity magnitude, averaged over the entire volume (Fig.(4.5)).

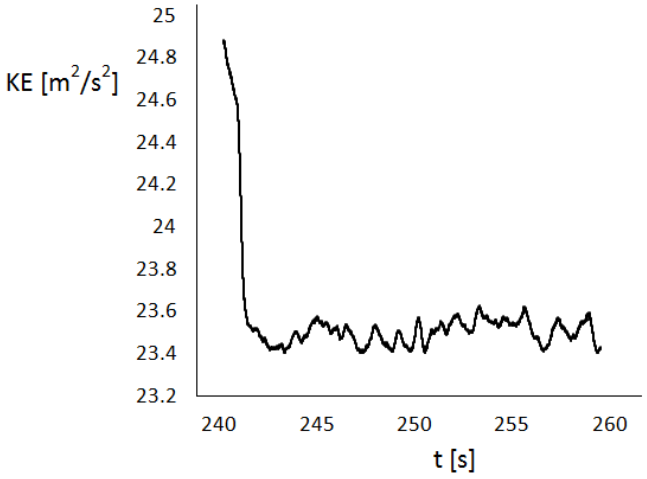

Figure 4.5. LES kinetic energy parameter for the data sampling.

This parameter can be expressed as:

$$KE = \frac{|u|^2}{2} \tag{4.4}$$

where $|u|$ is the velocity magnitude. When it stabilizes over a constant value, as showed in the previous figure, the flow field can be considered at convergence and statistical analysis may begin.

4.3 Comparison of experimental and numerical data

This paragraph is dedicated to the presentation of the numerical and experimental results used for the description of the jets behavior and models validation.

4.3.1 Domain investigated

The possibility to easily and precisely maneuver the laser probe through space, allows a thorough analysis of the plenum in several regions. Figure (4.6) describes in detail where the measurements are taken, with lines indicating the profiles in the xz-plane ($y = 0$) and dots indicating the ones along the y axis ($z = 0$). Considering the symmetrical configuration of the entire geometry, only half of the plenum was analyzed in the z axis, and only the central jet was considered for the investigation of the flow field for the case of y and x axes.

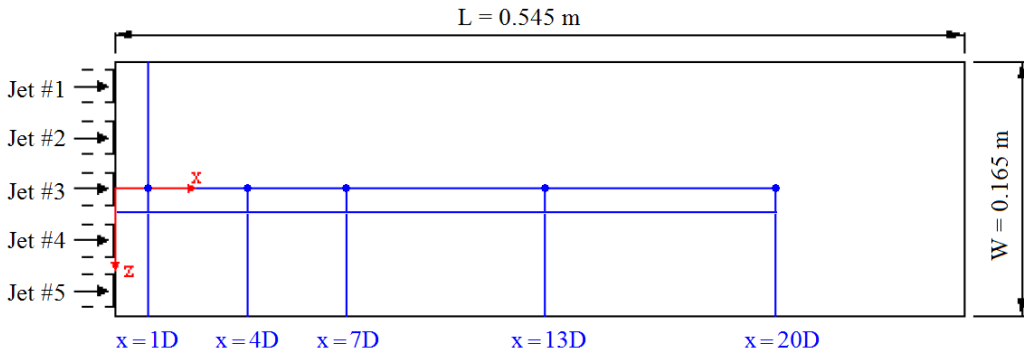

Figure 4.6. Measured profiles along the plenum.

Moving along the x axis we find the first measured points at $x = 1D, 4D$ and $7D$ as representative of the converging and merging regions (Fig.(I.3)), in which the expansion and interaction of the jets can be studied. Subsequently, the combined region is depicted from measurements at $x = 13D$. A last inquiry is focused on a search of a region away from the jets $x = 20D$, in which their

influence is not noticeable anymore. This general interpretation is backed up by streamwise and turbulence velocity profiles that are used for a detailed analysis of the flow and comparison with numerical data.

4.3.2 LES vs. Experimental results

This paragraph is further subdivided to first describe the behavior of the jets via experimental measurements solely, and then LES results will be discussed.

Just to point it out, the values $^{z}/_{L} = 0.2$ and $^{z}/_{L} = 0.4$ in the following figures represent the centerline of Jet#4 and Jet#5 respectively. Measurements are taken at $y = 0$ for the profiles of the xz-plane and at $z = 0$ for the profiles of the yx-plane.

Experimental data analysis

Figures (4.7) through (4.11) illustrate U_x velocity profiles along the z and y axes, nondimensionalized by the width and height of the plenum, respectively, in a series based on the distance from the jets inlet.

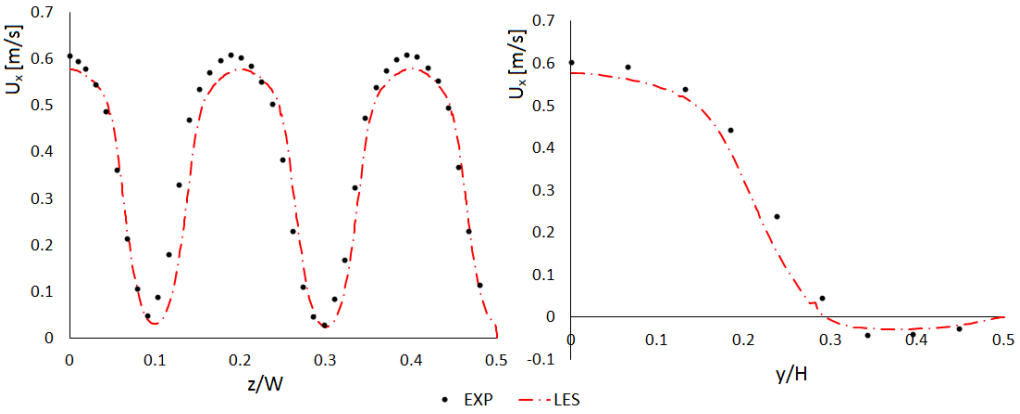

Figure 4.7. LES U_x velocity profiles at $x = 1D$.

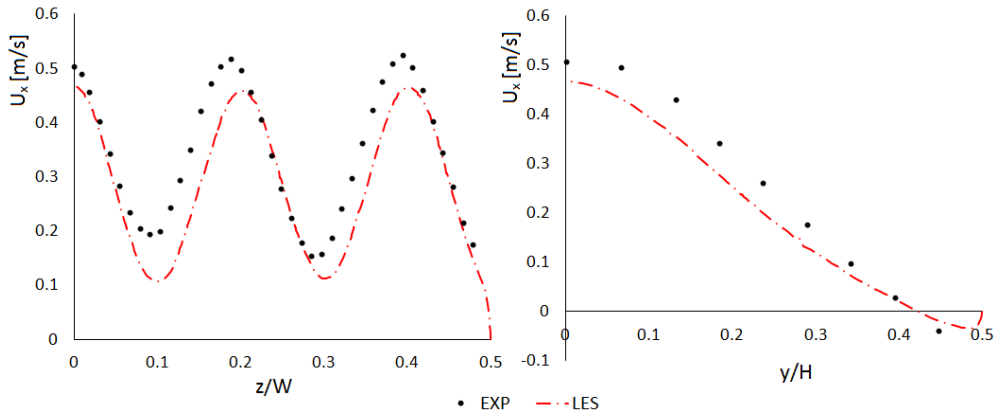

Figure 4.8. LES U_x velocity profiles at $x = 4D$.

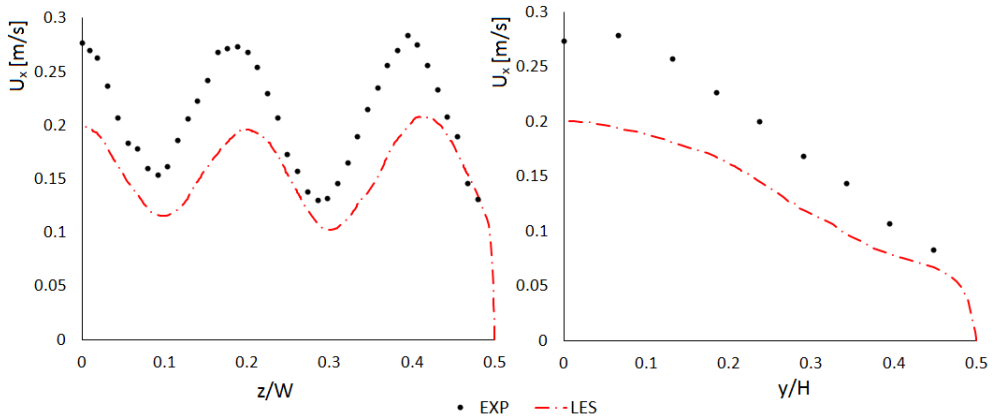

Figure 4.9. LES U_x velocity profiles at $x = 7D$.

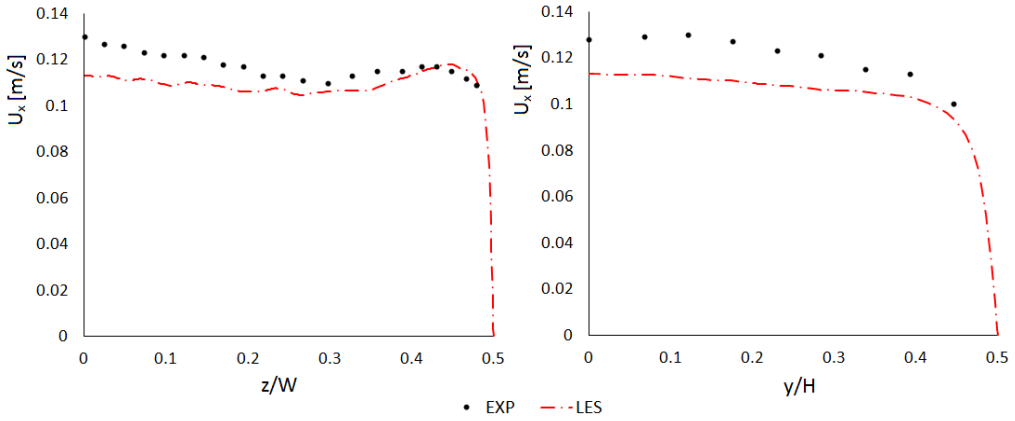

Figure 4.10. LES U_x velocity profiles at $x = 13D$.

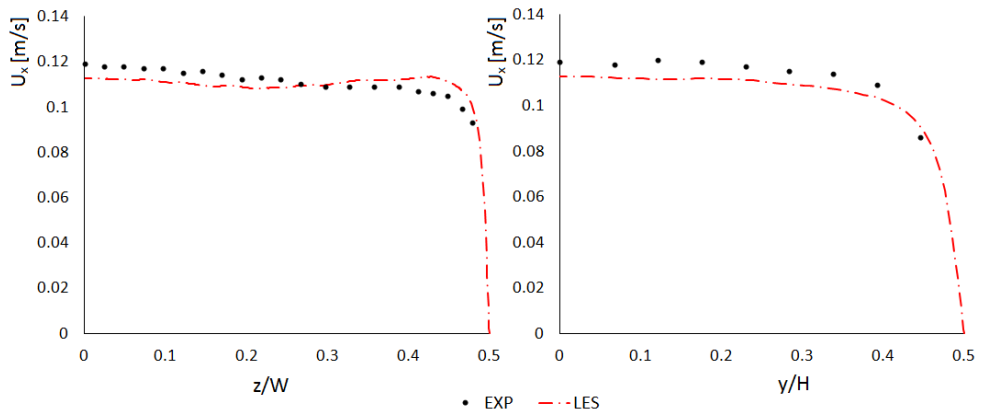

Figure 4.11. LES U_x velocity profiles at $x = 20D$.

Experimental data of the mean streamwise velocity profiles allow several considerations on the interaction of the jets to be made. As previously demonstrated, $x = 1D$ is close enough to the issuing of the jets to represent their core region and, for the configuration mentioned in the introducion we would expect a recirculation to take place between the jets. However, the jets here studied are so closely spaced that even after a single diameter downstream of the origin, this recirculation is already overcome by the jets expansion. Entrainment, the physical cause of the presence of recirculation, is indeed present and manifests its presence through the creation of a vortex on the top wall, which covers circa 37% of the half-height of the plenum (Fig.(4.7)).

Moving downstream the jets tend to expand more vigorously: the core region is substituted by the shear layer, the vortex in the xy-plane decreases significantly, vanishing in the region between $x = 4D$ and $x = 7D$, and the flow uniforms, with velocity peaks and dips, visible along z axis, coming together. The expansion of the jets influences the profiles form of Jet#3 along the y axis. Starting from $x = 7D$ downstream, we can notice that the peak of the mean velocity profile is not centered with respect to the plenum height. Its position moves from $^{y}/_{H} = 0.065$ on the right side of Fig.(4.9) to $^{y}/_{H} = 0.122$ in the two subsequent figures. In addition, when compared with rispect to the centerline velocity, its intensity decreases from 1.82% to 1.56 and 0.84% at $x = 7D, 13D$ and $20D$ respectively, indicating that the forces that vertically stretch the jet, are decreasing as the flow diffuses through the plenum. This lack of axial momentum in a parallel jet configuration is not uncommon. In fact, during his experiments on three bidimensional parallel jets, Tanaka discovered a similar behavior when the central jet separates as entrained by the lateral jets (Fig.(I.4b)), and in a totally different configuration, five parallel three-dimensional confined jets, Kunz et al. experimentally found the same separation, which they said to be in part attributed to turbulent diffusion.

At $x = 13D$, the U_x velocity profile along the z axis, assumes a non uniform distribution. Clearly this is not a distribution that would appear in a fully developed turbulent channel. An interpretation of this result lies in the assumption that Jet#2 and Jet#4 are more attracted to Jet#3 than they are to the jets close to the lateral wall, Jet#1 and Jet#5. This could also be noticed by the previous sections analyzed. In fact, at $x = 4D$ and $x = 7D$, even though the peaks all align at the same velocity, the peaks of Jet#4 and Jet#5 are moved to the left with respect to its centerline. If we normalize this displacement by the spacing s between the jets centerlines (Fig.(2.4)) we can find a value of 0.37 in the case of Jet#4 and 0.18 for Jet#5. Moving to $x = 13D$, the peak closer to the lateral wall is, contrary to the previous displacement, tilted to the right with respect to the centerline of Jet#5 by a normalized value of 0.6, which can be interpreted as influence of the Coanda effect.

Coming next, Fig.(4.12) through Fig.(4.16) are the experimental and LES $U_{x\,RMS}$ turbulence profiles along the z and y axes, nondimensionalized by the width and height of the plenum, respectively, again in series based on the distance from the jets inlet.

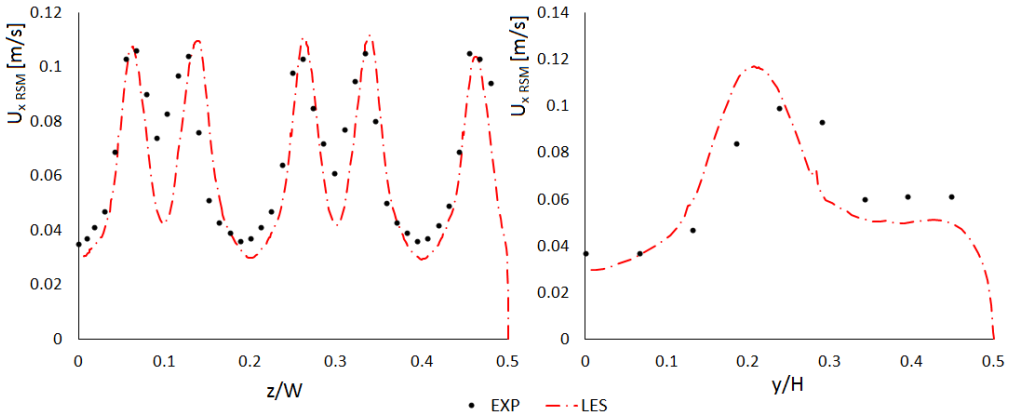

Figure 4.12. LES $U_{x\,RMS}$ profiles at $x = 1D$.

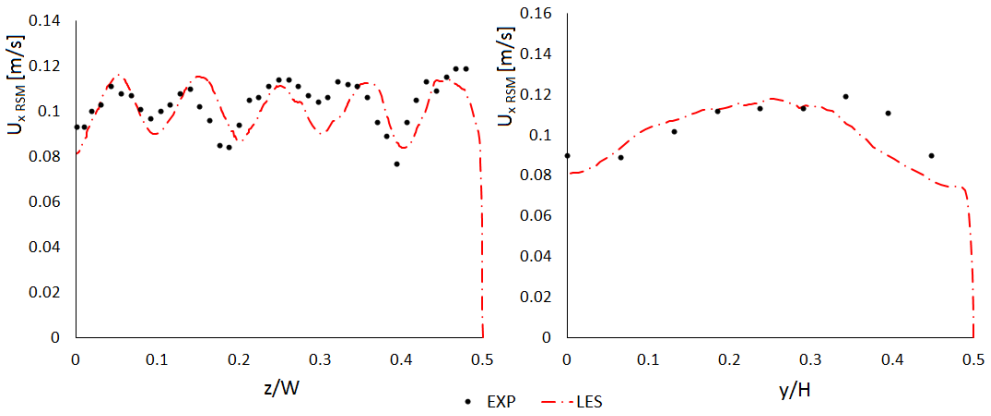

Figure 4.13. LES $U_{x\,RMS}$ profiles at $x = 4D$.

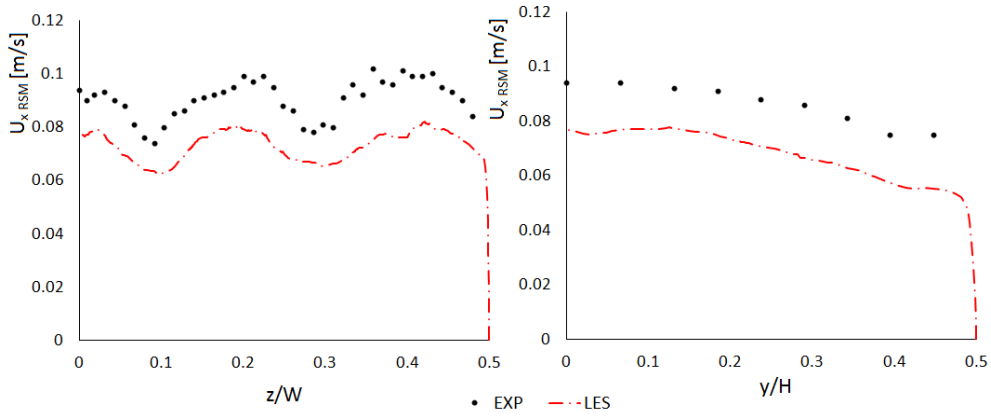

Figure 4.14. LES $U_{x\,RMS}$ profiles at $x = 7D$.

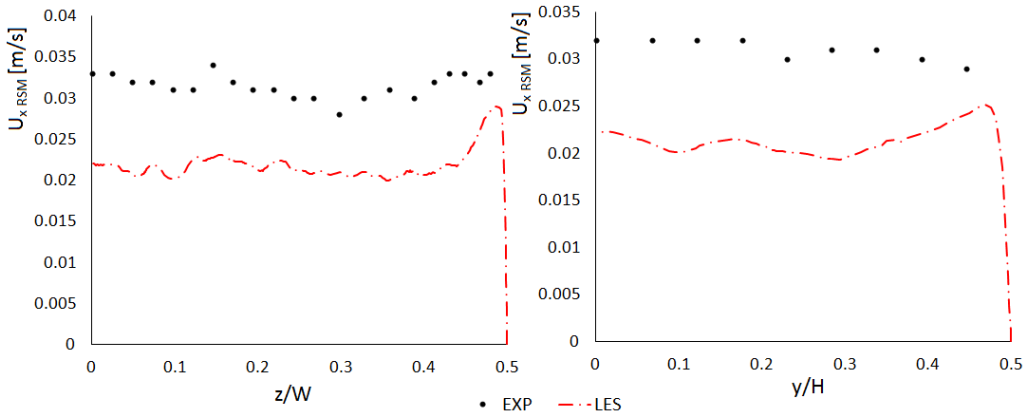

Figure 4.15. LES $U_{x\,RMS}$ profiles at $x = 13D$.

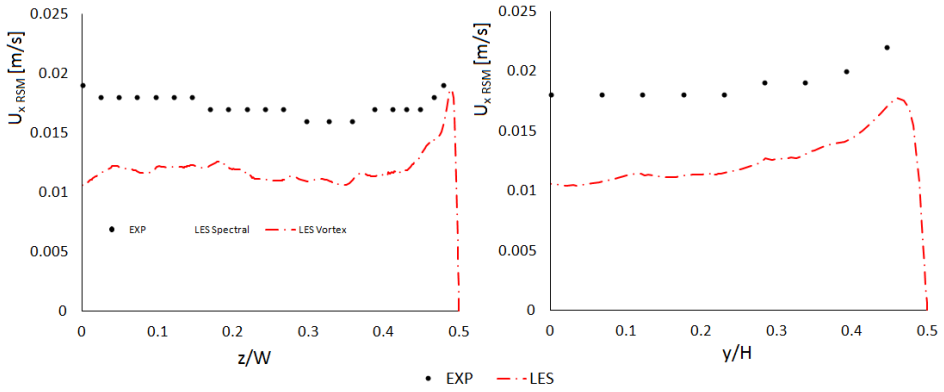

Figure 4.16. LES $U_{x\,RMS}$ profiles at $x = 20D$.

The measured turbulence fluctuations can add several information about the parallel jet configuration. The five peaks in the profiles at $x = 1D$ and $x = 4D$ now represent the shear layer of the jets that at $x = 7D$ it can be noticed to be fully merged. Turbulent fluctuations decreases significantly as we move downstream, with a reduction, with respect to the values at $x = 7D$ where the jets are still clearly noticeable, of $\approx 64\%$ and $\approx 77\%$ at $x = 13D$ and $x = 20D$, respectively. Combining the information of the mean velocity and turbulent profiles, the turbulence intensity can be calculated as:

$$I = \frac{U_{x\,RMS}}{U_x} \tag{4.4}$$

which can be interpreted as the magnitude of the fluctuations with respect to the mean velocity. This parameter is plotted in Fig.(4.17)

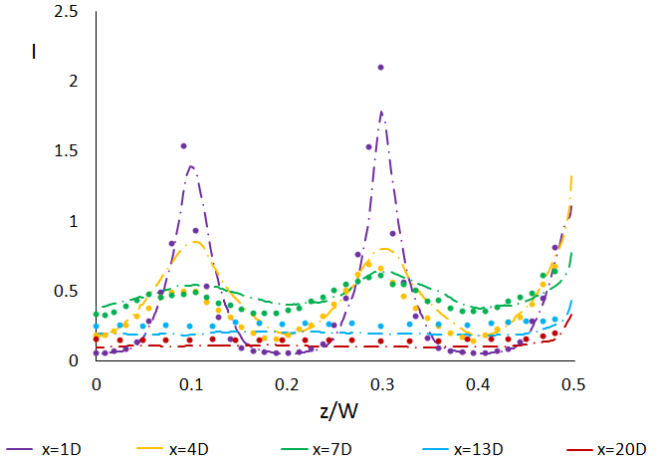

Figure 4.17. Turbulent intensity of experimental data (dots) and LES (dotted lines).

Considering that the turbulent intensity measured at the centerline of the pipe is $I = 0.05$, a value also found in the centerline of the jets at $x = 1D$, turbulence intensity increases significantly during the expansion of the jets, and it settles as their influence slowly disappears.

One final parameter that could be extrapolated from the measurements is the spreading ratio of the central jet, evaluated using the $U_x$velocity along the x axis as:

$$SR = \frac{U_{jcl} - U_{mcl}}{U_{jcl}} \tag{4.5}$$

where U_{jcl} is the centerline velocity and U_{mcl} is the velocity in the region between two adjecient jets. This parameter is useful in determining two important physical characteristics of parallel jets:

- *Jet deflection*: If we find a solution with a SR that becomes negative, it means that averagely, in the case of prallel jets, we are in the presence of deflecting jets, as it happens for the three free jets discussed in the introduction [16].

- *Entrainment*: When the SR is higher than one, it means that the velocity between jets is negative, a situation that signs the presence of a recirculating vortex caused by entrained fluid.

Figure (4.18) illustrates the spreading ratio of the Jet#3 for experimental and LES data.

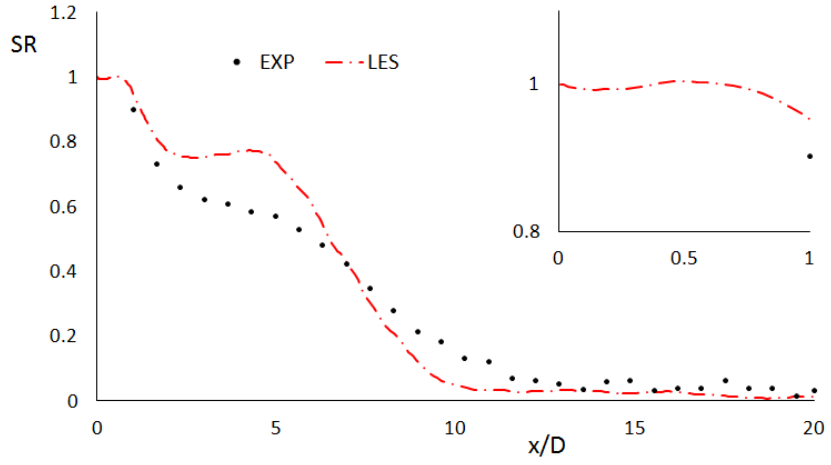

Figure 4.18. LES Spreading Ratio of the $U_x$velocity, central jet .

From the above figure it can be deduced that if there are vortexes between jets in the xz-plane at $y = 0$, they are located in a limited area before $x = 1D$. This result was expected due to the close vicinity of the jets, which limits the formation of vortexes in the plane previously mentioned. The SR ubruptly drops in the first couple of diameters because of the increase of the velocity U_{mcl}, which reaches it maximum at $x \approx 3D$. Subsequently, the decrease of the SR is more gradual untill it approaches zero at $x \approx 14D$, meaning that the influence of the jets has desappeared. The positive values of this parameter through the plenum, indicate that Jet#4, and symmetrically Jet#2, are not entrained by Jet#3 as in the case of the free three jets even though as previously seen, there is still a slight tilt toward the central jet.

Along the x axis we can also analyze how turbulence develops (Fig.(4.19)).

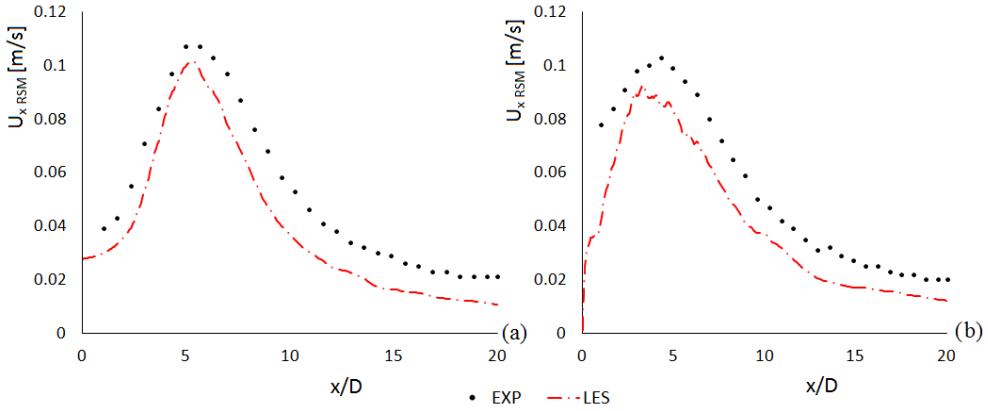

Figure 4.19. LES $U_{x\,RMS}$ profiles, $y = 0$ and (a) z= 0, (b) z= 0.0165 m.

The two peaks in the previous figures are representative of shear layer merging region. For the case of the centerline turbulence of Jet#3, Fig.(4.19a) the peak represents the merging of the shear layers that surround the central jet. For the other case, Fig.(4.19b), the shear layers that merge together come from different jets, particularly Jet#3 and Jet#4. It is important to notice that even though at $x \approx 14D$ mean velocities have already reached their asymptote, at the same distance the RMS values are still decreasing, indicating that turbulence generated from the interference of the jets, still needs to settle. This settling seems to be reached at $x = 20D$.

Large Eddy Simulation results

As mentioned in Ch.2, Large Eddy Simulation is a powerful tool in analyzing a flow field since its formulation also allows for a statistical analysis of the

results, rather than a mere comparison of mean quantities, such as in the case of URANS models. The instantaneous physical values, after the flow field converged, were averaged over $5.5\ 10^4$ samples, which is enough to define the trend of the LES, but not enough to have smooth profiles, especially for the fluctuations.

Out of all the analysis of the experimental measurements, LES can predict this parallel jets configuration with a general underestimation of both the mean velocities and turbulence profiles. The qualitative prediction of this parallel jets configuration is globally correct, but quantitatively there are discrepancies with respect to the experimental measurements that reach values of $\approx 27\%$ for the mean velocities and $\approx 30\%$ for the turbulence profiles. Moving downstream from the origin, we see a good agreement of the result right when the jets issue into the plenum, noticeable from the U_x, $U_{x\,RMS}$, and SR. The subsequent interpretation of the results depends on the profiles considered. The critical region for the U_x profiles is around $x = 7D$, which can be considered the zone of the full jets expansion, while when approaching $x = 13D$ we start to see an improvement in the comparison, with good agreement in the last profile considered. The case of the $U_{x\,RMS}$ profiles is different, with a level of agreement with experimental results decreasing from $x = 1D$ to $x = 20D$, showing a strong underestimation of the turbulence. Results improve when the turbulent intensity is considered, Fig.(4.17), in which all of the LES results, aside from $x = 4D$, show reasonably good agreement. The last parameter analyzed, the Spreading Ratio, is another demonstration of the inaccuracy in the representation of the jet expansion. In addition, when considering the nearly plenum-inlet zone, LES simulation do not seem to predict any recirculation in the xz-plane, a result that can be considered acceptable confirming that near the inlet of the plenum LES demonstrated to be accurate.

Figure (4.20) and Fig.(4.21) give an indication of how LES replicates the flow field in the xz-plane and xy-plane at $y = 0$ and $z = 0$ respectively.

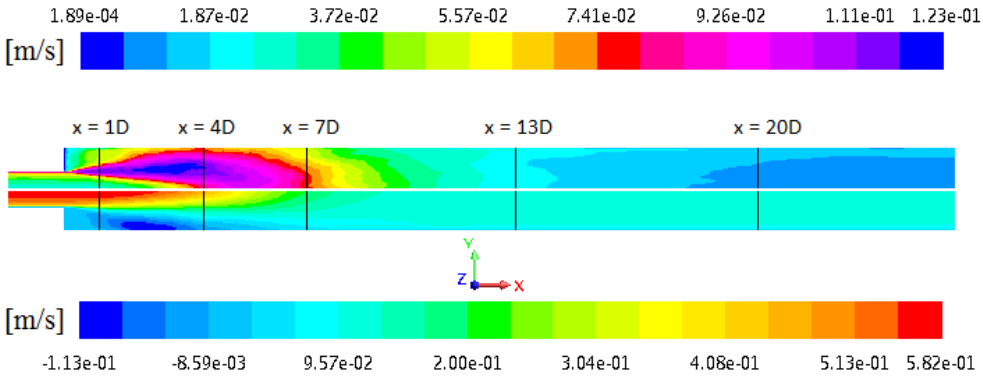

Figure 4.20. LES contours of $U_{x\,RMS}$ (top), and U_x (bottom) on the xy-plane, $z = 0$.

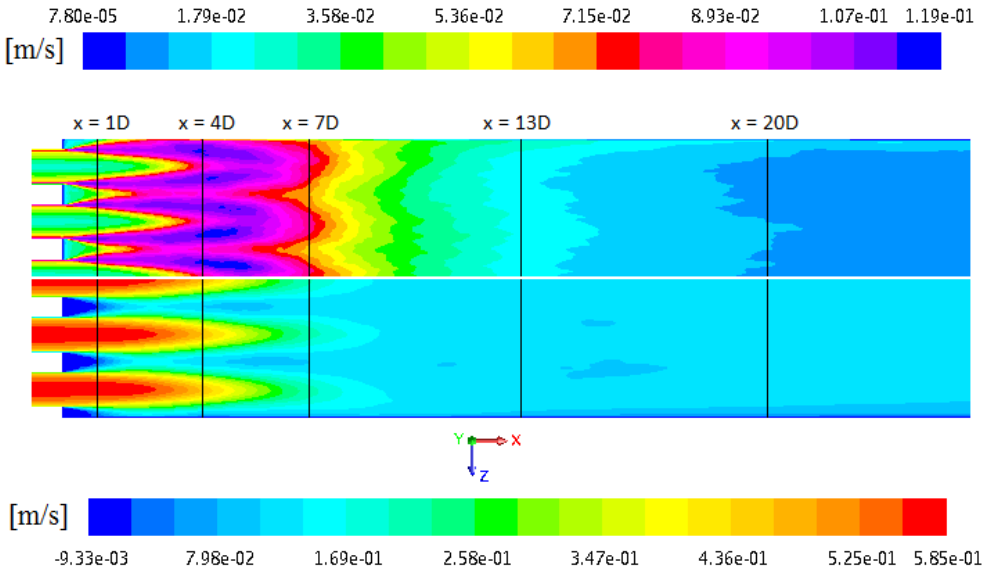

Figure 4.21. LES contours of $U_{x\,RMS}$ (top), and U_x (bottom) on the xz-plane, $y = 0$.

In each figure, half domain is colored with U_x velocities and the other half with $U_{x\,RMS}$. The contours representation gives a better view of the flow field in the planes where experimental measurements were taken.

Turbulent fluctuations are shown to be concentrated in the first 7 diameters from the origin. They reach values one order of magnitude higher than the flow in the pipes, concentrating these peaks in the shear layer of the jets. At approximately 10 diameters turbulent fluctuations decrease back to the values in the pipes and, continuing downstream, they keep decreasing. It is important to notice that the reproduction of turbulent fluctuation by LES approach starting at $x = 7D$, is 10 to 25% lower than the experimental results.

Mean velocity contours highlight the presence of the vortex in the xy-plane and the almost-quiescent region, in terms of U_x, between jets in the xz-plane. Jets appear straight, and the small deviation of Jet#4 toward the central jet, demonstrated from Fig.(4.10), is barely noticeable. What is more apparent is the attraction of Jet#5 to the lateral wall, which seems to continue, according to LES, even at $x = 20D$ (Fig.(4.11)).

In addition to mean velocities and turbulent profiles, instantaneous coherent structures present in the domain can be displayed when the LES approach is adopted. The way of identifying these turbulent structures is achieved with the q-criterion, defined as [47]:

$$Q = \frac{1}{2}\left(\Omega_{ij}\Omega_{ij} - \mathrm{S}_{ij}\mathrm{S}_{ij}\right) \tag{4.6}$$

where Ω_{ij}, S_{ij} are the anti-symmetric and symmetric part of the velocity gradient, defined in Eq.(1.37) for the case of mean velocities. Based on this definition, this parameter is an indication of the balance between the rate of vorticity and the rate of strain. Regions with positive q-criterion values correspond to vortical structures. The coherent structures of the geometry analyzed are displayed in Fig.(4.22) and Fig.(4.23).

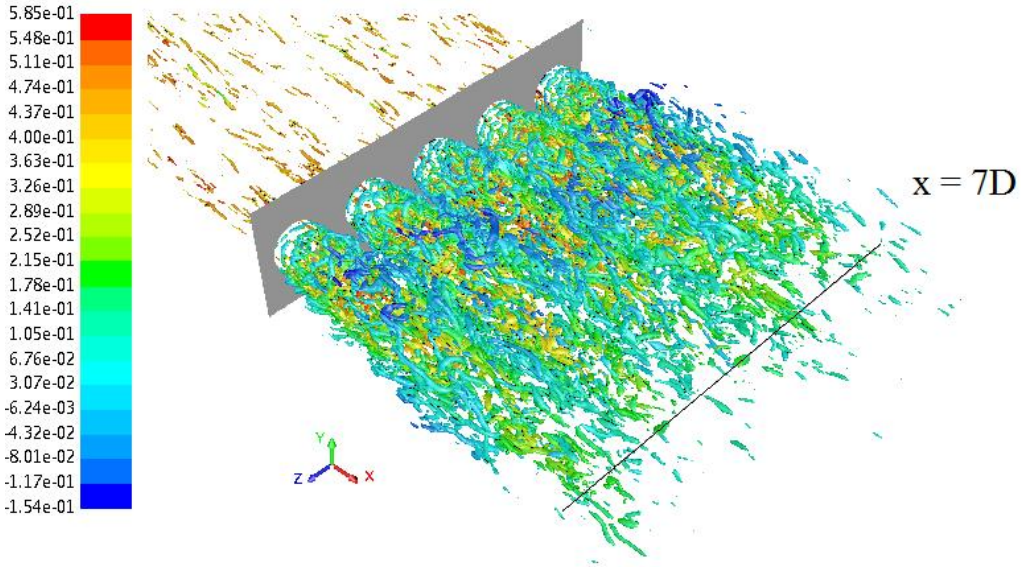

Figure 4.22. LES q-criterion colored by mean streamwise velocity, Q = 5000.

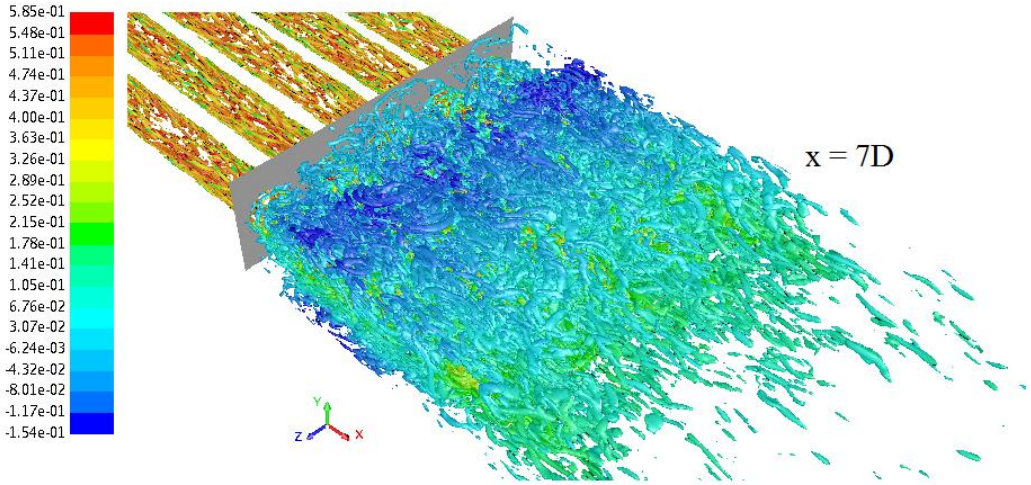

Figure 4.23. LES q-criterion colored by mean streamwise velocity, Q = 1000.

Figure (4.22), demonstrates that the majority of turbulent structures generate inside the plenum, where the jets interact. Decreasing the q-criterion value, leads to an increase in the number of coherent structures visible. Even so, after approximately $x = 10D$, all the structures disappear. This behavior, will be further analyzed in future studies through a refinement of the grid.

4.3.3 URANS vs. Experimental results

Mean streamwise velocity profiles of the models mentioned in Par.(3.1.3), except for the k-ε RNG which shown unphysical results, are compared with experimental measurements in Fig.(4.24) to Fig.(4.28). Figures are organized as in the previous paragraph.

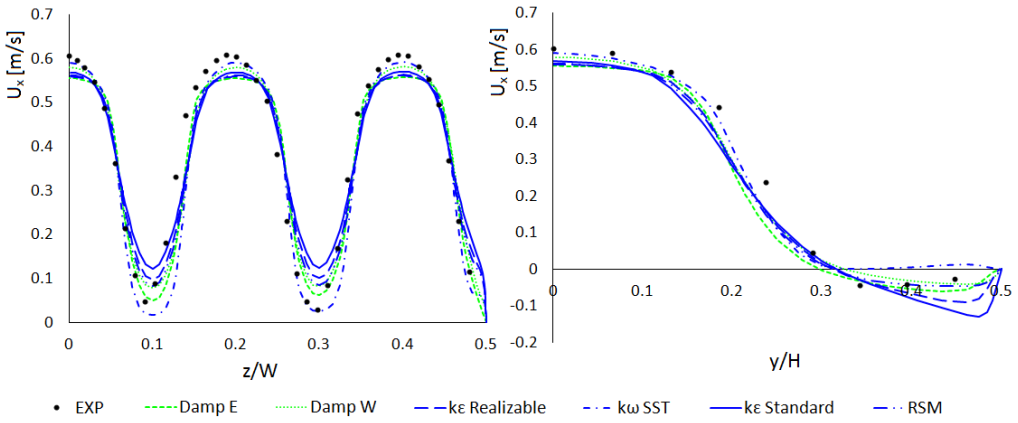

Figure 4.24. URANS U_x velocity profiles at $x = 1D$.

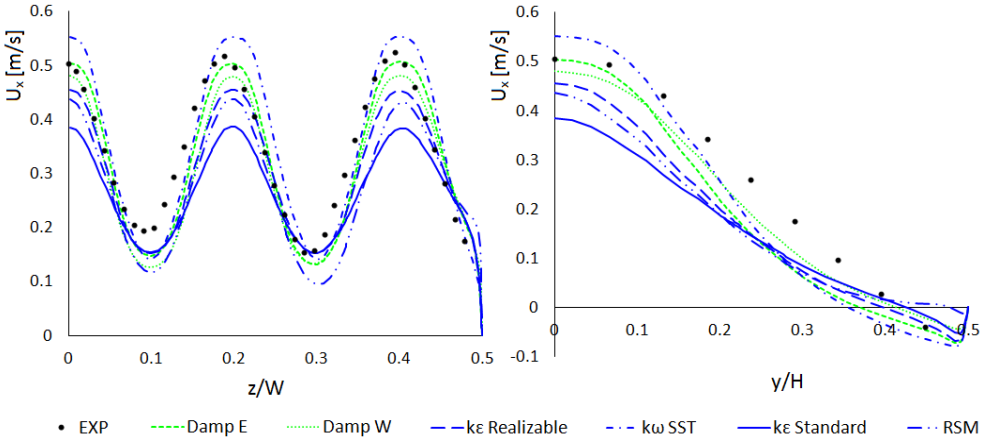

Figure 4.25. URANS U_x velocity profiles at $x = 4D$.

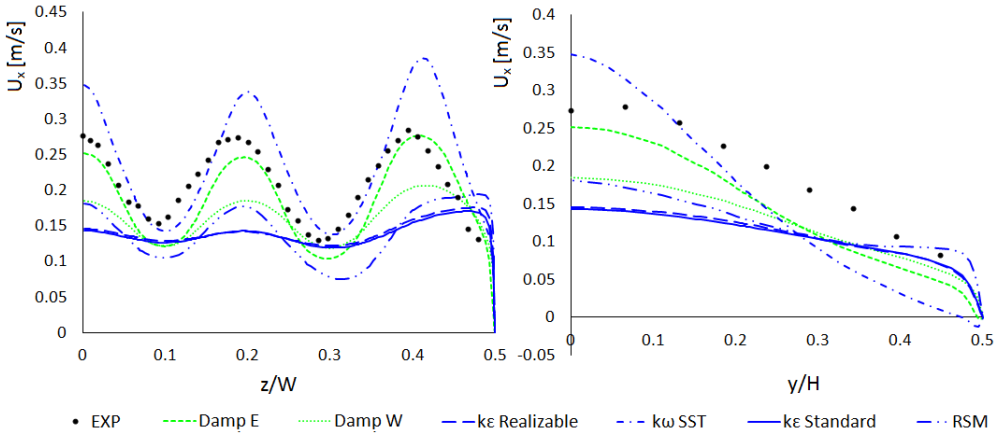

Figure 4.26. URANS U_x velocity profiles at $x = 7D$.

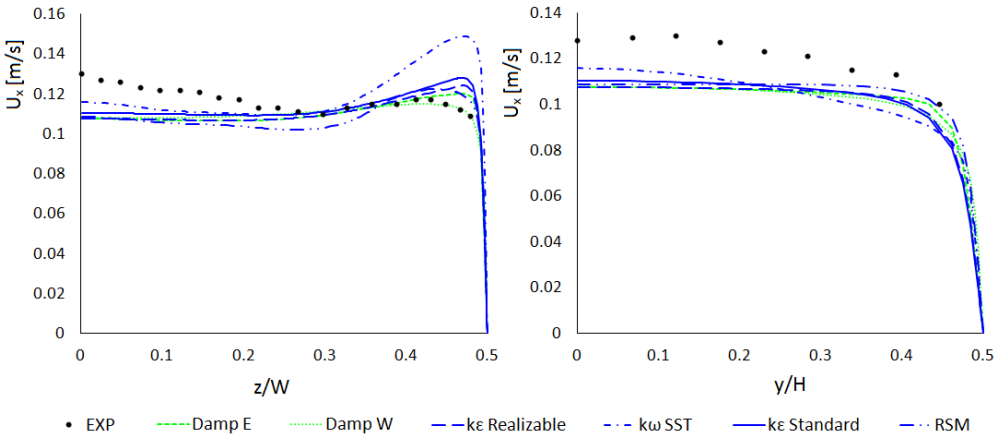

Figure 4.27. URANS $U_x$velocity profiles at $x = 13D$.

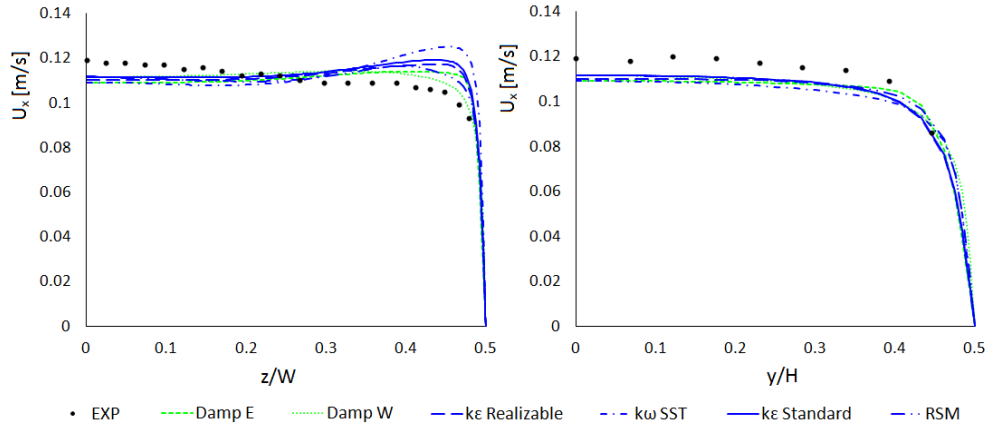

Figure 4.28. URANS $U_x$velocity profiles at $x = 20D$.

The first thing that can be noticed is the similarity of the solutions in the regions very close to the jets inlet and far from it, which is basically where the jets have the least influence on the mechanics of the flow field. In particular we find the most discrepancies between the models at $x = 4D$, and $x = 7D$.

Among the linear eddy viscosity models the k-ω SST, that was found to be the best model for the prediction of the pipe flow, is overestimating the jets as they expand. Even if the core region is fairly well predicted, the vortex in the xy-plane seems to be shifted downstream, which causes the velocities peaks at $x = 4D$ and $x = 7D$ to be greater than all the other models. In the case of the eddy viscosity k-ε family models, the Standard and Realizable models appear to predict the flow similarly, with significant differences only at $x = 4D$. Switching to the Non-Linear models, which are implemented from the k-ε Standard, improvements are significant especially when the Damp E formulation is adopted. Finally, the RSM demonstrates a general underestimation of the results with respect to the more accurate Non-Linear Damp E model and experimental data.

The next parameter analyzed is the spreading ratio shown in Fig.(4.29).

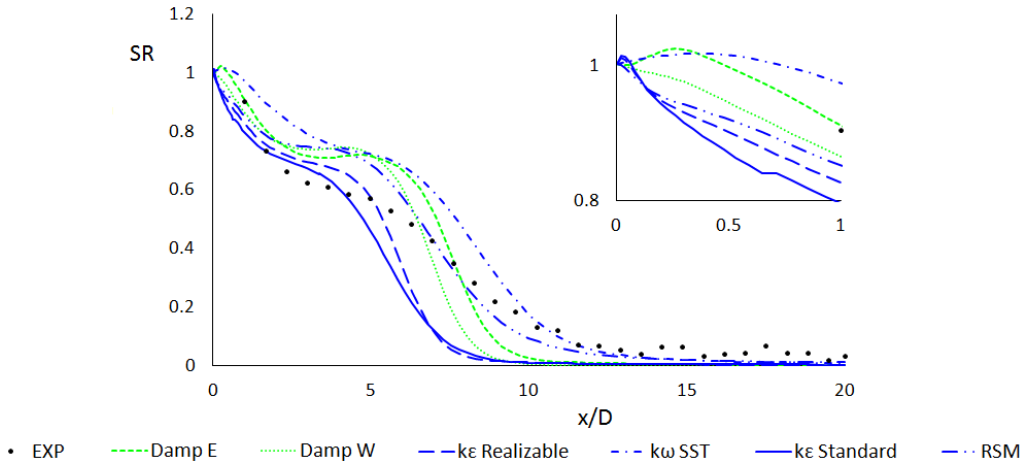

Figure 4.29. URANS Spreading Ratio of the $U_x$velocity, central jet.

Models only have a qualitative agreement of the spreading ratio, whereas quantitatively there are strong general descrepancies. Regarding the two physical interpretations of the SR, it is noticeable from the small box in Fig.(4.29) how the Damp E, k-ω SST and k-ε Standard are the only models that detect a recirculating region between the jets. Moreover, the asymptote at $SR = 0$, which indicates the uniformity of velocities, is underpredicted for most of the models, especially the linear k-ε. Proof of this last statement is also clear from Fig.(4.26), where these models strongly underpredict the velocity profiles along the z axis.

Experimental results of turbulence, include only RMS velocity profiles, and the only model capable of reprodicing them is the RSM model. All the others only have the turbulent kinetic energy and dissipation rate as an indication of the turbulence level, and for this reason Fig.(4.30) through Fig.(4.34) will compare solely the results of the RSM model with experimental data.

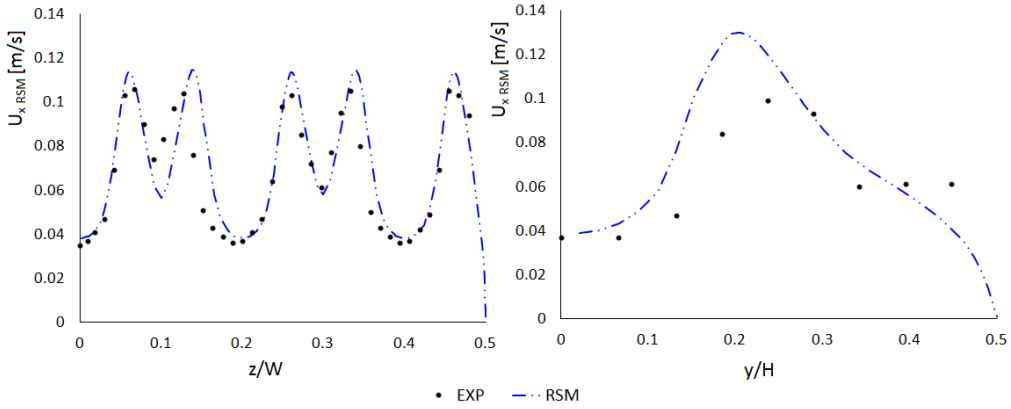

Figure 4.30. URANS $U_{x\,RMS}$ profiles at $x = 1D$.

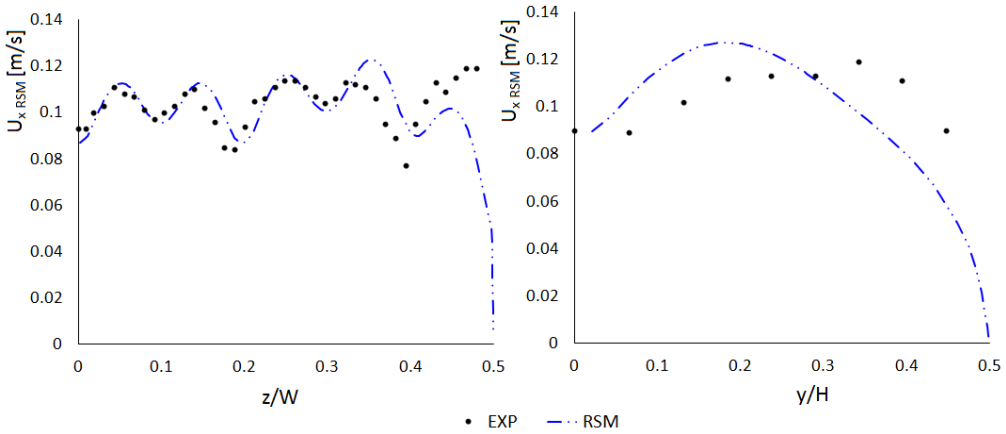

Figure 4.31. URANS $U_{x\,RMS}$ profiles at $x = 4D$.

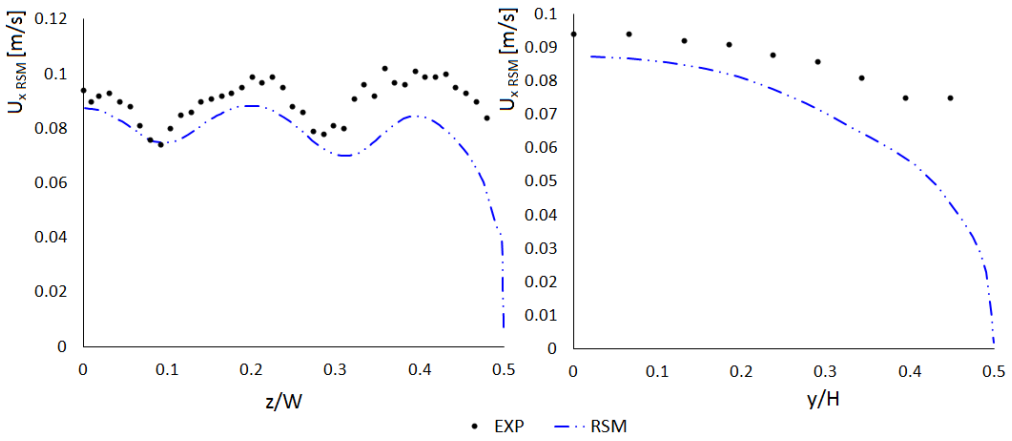

Figure 4.32. URANS $U_{x\,RMS}$ profiles at $x = 7D$.

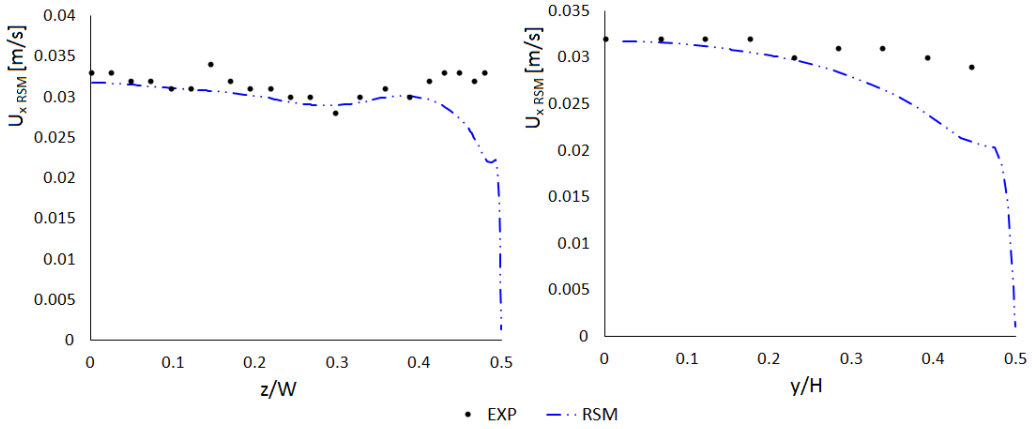

Figure 4.33. URANS $U_{x\,RMS}$ profiles at $x = 13D$.

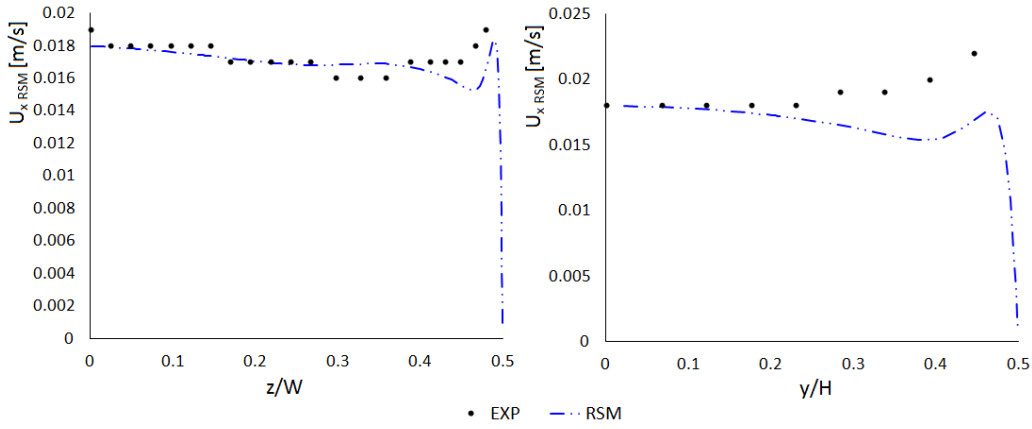

Figure 4.34. URANS $U_{x\,RMS}$ profiles at $x = 20D$.

Despite not being the best model for capturing the U_x velocity field, the behavior of the RSM model in representing the RMS profiles of the U_x velocity is fairly accurate, especially in along the z lines, where good agreements with experimental data can be noticed at several distances from the origin. In addition an good match is noticeable in Fig.(4.35), where turbulence is represented in its development along the x axis.

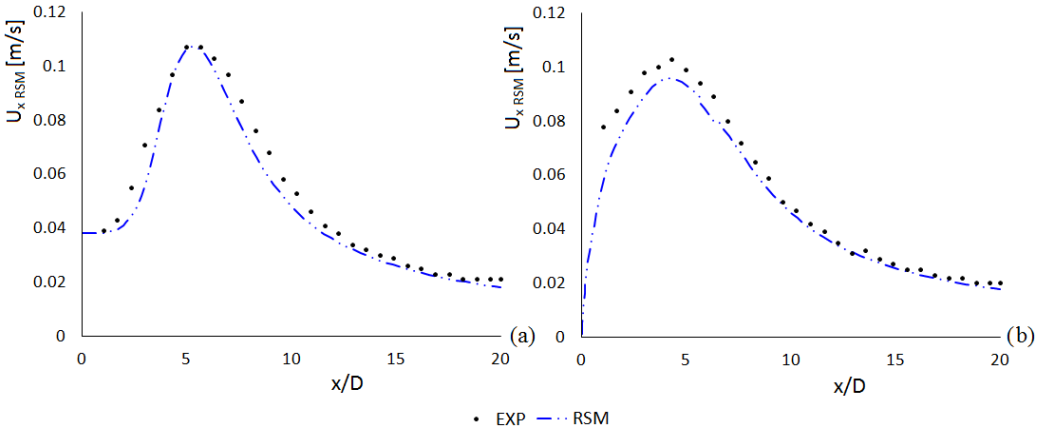

Figure 4.35. URANS $U_{x\,RMS}$ profiles, $y = 0$ and (a) z= 0, (b) z= 0.0165 m.

The different behavior that all the models here analyzed exhibit, can be exploited to draw some additional considerations on the flow distribution of the jets. We have seen that out of all the profiles analyzed, certainly at $x = 7D$ there seem to be the most discrepancies between numerical, LES included, and experimental results. In particular, all the models except for the k-ω SST underestimate the mean velocitiy profiles with respect to the experimental measurements. Since the mass flow rate must be conserved, the streamwise velocities must redistribute in other areas of the zy-plane at $x = 7D$, as demonstrated in Fig.(4.36). From top to bottom we find the k-ω SST, which overestimates the U_x profiles at $x = 7D$, the Non-Linear DampE model, which most closely resembles experimental data, and LES, with an underestimation of the results. Using the same range of velocities for the three cases, the comparison shows how the shorter peaks of the LES profiles are compensated with the almost complete absence of recirculation regions surrounding the jets. The experimental flow field can be interpreted to be a configuration, in terms of recirculating regions at this particular plane, between the DampE models and k-ω SST. Considering that the former slightly underestimates the mean velocities profiles, stronger recirculation regions should also be part of the real behavior of the jets as a consequence of mass conservation.

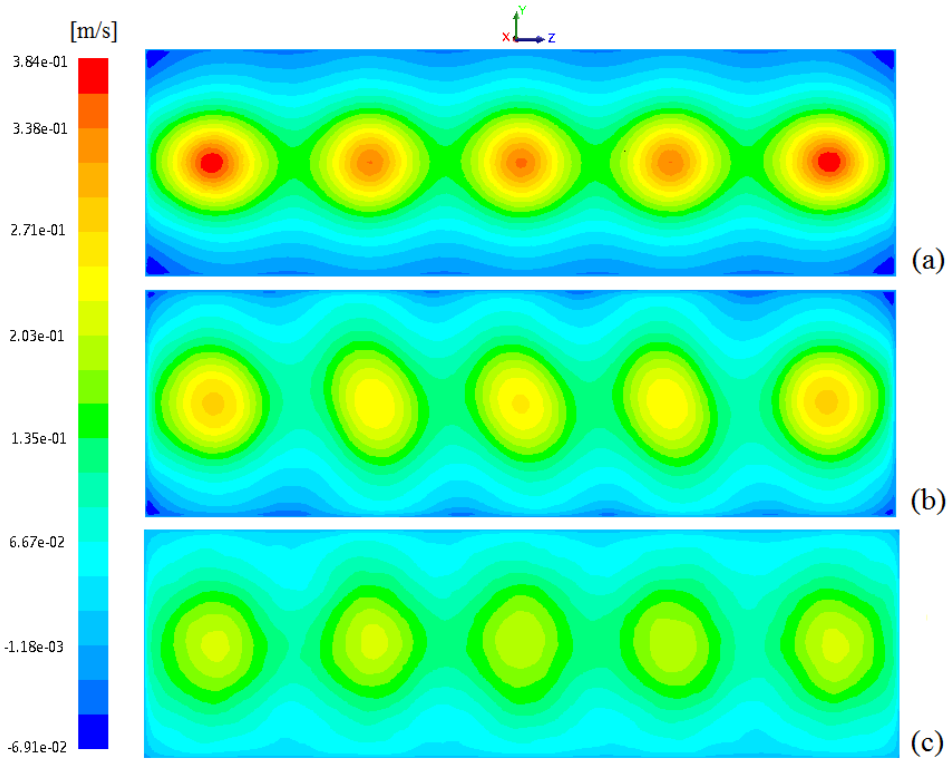

Figure 4.36. Contours of U_x, zy-plane at $x = 7D$: (a) k-ω SST, (b) Damp E, (c) LES.

We have seen how the different URANS models behave in the prediction of the flow field of the parallel jets configuration studied in this thesis. These models are more interesting in an engineering point of view than the LES due to the limited need of computational resources. Since many different URANS approaches have been examined so far, one last parameter that could be useful for the selection of he most suited in representing a parallel jets configuration, is the computational time. Table (4.1) summarizes computational times of the three different classes of modelling the Reynolds stress tensor. The values in the last column are the indication of the computational time nondimensionalized with respect to the slowest model, i.e. the computational needier, in terms of seconds necessary to compute each time step Δt. This comparison was performed at the same computational conditions in terms of machines utilized, and number of iterations for each time step, for the case of the PISO scheme. For the case of linear eddy viscosity models, simulation time is the same and the k-ε Standard is selected as representative. Even though the only simulations that used PISO as the pressure-velocity coupling scheme are run in the case of Non-Linear models, the table also shows the difference between the PISO and Fractional Step, when this last non iterative method is available. This latter

scheme was proved to be approximately four times faster than the PISO scheme, leading to a substantial reduction of computational time without compromising the results.

	Models	**PV-Coupling**	**s/Δt**
Linear Eddy Viscosity	$k\varepsilon$ Standard	Fractional Step	0.104
		PISO	0.413
Non Eddy Viscosity	RSM	Fractional Step	0.156
		PISO	0.578
Non-Linear Eddy Viscosity	Damp E	PISO	1

Table 4.1. URANS Computational time comparison.

For the calculations performed in this thesis we can see from Table (4.1) that the non-linear eddy viscosity model, in particular the Damp E formulation, is indeed the most accurate one in predicting the flow field, but it also requires the longest computational time.

4.4 Experimental anomaly

In Ch.2, the LDV instrumentation was mentioned to be composed of two different laser wavelengths, meaning that two components of the velocity can be measured. Previous results show the streamwise velocity profiles U_x and the fluctuating velocity profiles $U_{x\,RMS}$. The other measured component include velocity profiles along the z axis, in particular U_z. If we considered the z axis at $x = 1D$, which is in the core region, given the symmetrical configuration of the domain, we would expect these velocities to behave symmetrically with respect to the jets centerline, meaning that the jets are expanding symmetrically as they enter the plenum. This expectation does not match the results. Symmetry is indeed present, but it seems to be positively shifted as shown in Fig.(4.38), red dots. This behavior leads us to evaluate the possible misalignement of the laser probe, hence the fringes in the probe volume, with respect to the coordinate system, as displayed in Fig.(4.37). As we mentioned in Par.(1.3), the velocity of a particle measured is perpendicular to the direction of the fringes. Therefore, if they are not perfectly aligned with the coordinate system of interest, the velocity components are misleading.

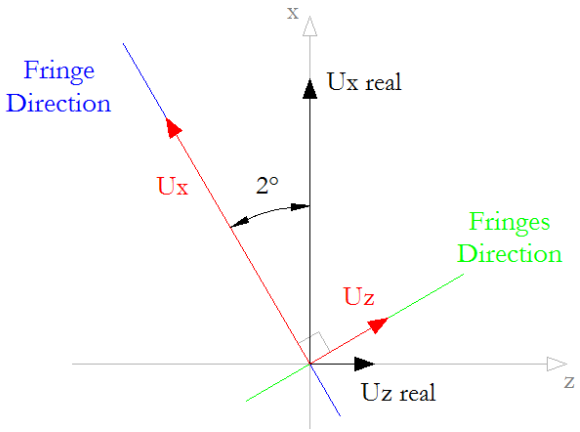

Figure 4.37. Hypothesised misalignment of the laser probe.

Hypothesising a deviation of two degrees from the plenum coordinate system, and calculating the differences in the velocity components, we obtain the values in Tab.(4.2), where U_x, U_z represent the values from the measurements (vectors shown in Fig.(4.37)), $U_{x\,\mathrm{real}}$, $U_{z\,\mathrm{real}}$ are the previous velocities projected on the axis and summed, and $U_{x\,\mathrm{Error}}$ is the misalignment error on the streamwise component with respect to $U_{x\,\mathrm{real}}$.

x location	$\boldsymbol{U_x}$ **[m/s]**	$\boldsymbol{U_z}$ **[m/s]**	$\boldsymbol{U_{x\,\mathrm{real}}}$ **[m/s]**	$\boldsymbol{U_{z\,\mathrm{real}}}$ **[m/s]**	$\boldsymbol{U_{x\,\mathrm{Error}}}$ **[%]**
1D	0.607	0.025	0.6075	$3.8\ 10^{-3}$	0.08
4D	0.504	0.024	0.5045	$6.4\ 10^{-3}$	0.1
7D	0.277	0.014	0.2773	$4.3\ 10^{-3}$	0.11
13D	0.13	0.007	0.1302	$2.4\ 10^{-3}$	0.12
20D	0.119	0.006	0.119	$1.8\ 10^{-3}$	0.11

Table 4.2. Experimental anomaly values.

Calculations in the previous table are referred to the centerline velocity of Jet#3 at the different location specified. It is evident that the error of the streamwise components of the velocity U_x, in the eventuality of the misalignment hypothesised, is negligible. These percentages of error are similar in all the profiles analyzed, and therefore the profiles plotted in the previous paragraphs are not affected by the eventual misalignment. On the other hand, Fig.(4.38) clearly shows a difference in the U_z velocity profiles in which the black dots, representing what U_z the profiles would be in case of a correct alignment ($U_{z\,\mathrm{real}}$ values), are considered a more correct behavior of the jets in this region. In fact, if we consider the centerline of Jet#4, $^{z}/_{W} = 0.2$, we can notice positive U_z

velocities on the right side and negative on the left, indicating a symmetrical expansion of the jet itself. The same behavior is also noticeable in case of Jet#5.

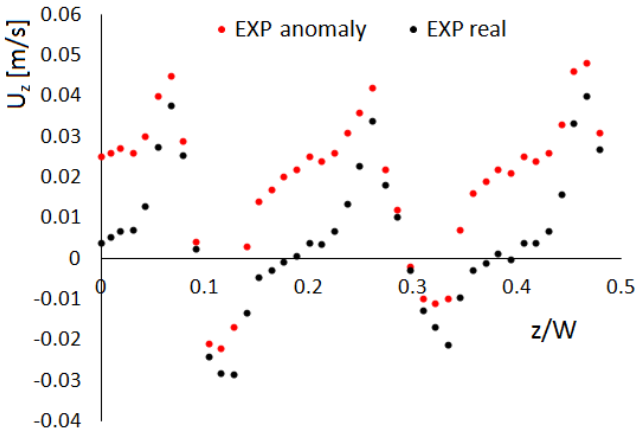

Figure 4.38. Experimental U_z profiles anomaly, $x = 1D$.

To better notice the supposed anomaly, the U_z velocity profiles at $x = 20D$ are displayed in Fig.(4.39). Even in this case, the values of the velocities of the red dots, which are approximately 5% of the streamwise velocity, and their distribution, indicating a continuation of positive U_z velocities even in the left side of the plenum, could be anomalous. Instead, more believable is the profile of the black dots, where velicities are closer to zero, especially in the origin, and with a distribution that could become negative, indicating that the three central jets, which we have demonstrated are merging (Fig(4.10) left), tend to expand toward a more uniform velocity distribution.

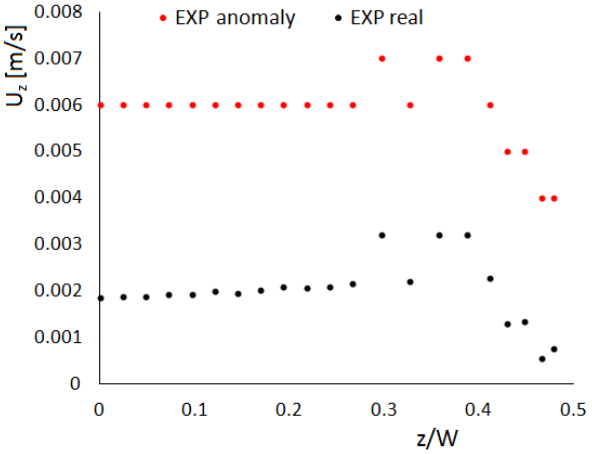

Figure 4.39. Experimental U_z profiles anomaly, $x = 20D$.

The previous anomaly could have also been interpreted as a misalignment of the five pipes with respect to the x axis. However, results of the streamwise profiles, especially Fig.(4.2) and Fig.(4.3) prove this theory wrong. The velocity peak of Jet#3 is aligned with the its centerline, and overlapping all the U_x profiles at $x = 1D$ we notice a symmetrical, even if slight, merging of the four lateral jets, toward the center jet.

For the reasons explained in this last paragraph, velocitiy and turbulent profiles along the z axis were not considered in the analysis. Further studies on the same geometry will include the use of the PIV for the flow field visualization, which can verify the anomaly noticed with the LDV.

Conclusions

In this thesis, turbulent parallel jets interactiong into a confinement are investigated. This configuration is of industrial interest for fluid and thermo dynamics, mixing and other phenomena associated with it. The present study is focused on the complex fluid dynamics of this configuration and it is investigated via experimental and numerical approaches. In particular, the geometrical features of the domain studied in this work were designed aiming at finding a configuration that could represent an infinite row of confined parallel jets or, in terms of real configurations, an annular confinement. The goal is to investigate the physics of the parallel jets configuration via experimental and numerical analysis, which are also compared for the validation of the turbulence models adopted. The experimental campaign started with the design of the domain of interest, five closely spaced parallel jets issuing into a rectangular confinement, each with a Reynolds number based on the pipe diameter of $Re_D = 10^4$. The facility was subsequently assembled at the Combustion Laboratory of Politecnico di Milano. LDV measurements were taken in several locations inside the plenum to allow the visualization of the interaction of the jets as clear as possible. An identical domain was numerically modelled with two grid sizes used for the URANS and LES numerical approaches. Considering the importance of the former in engineering applications, due to the less computational requirement with respect to the latter, several URANS linear eddy viscosity models implemented in the code were compared. In addition, a non-linear formulation, developed at the CFDLab of Politecnico di Milano for the purpose of better reproducing complex flows, was added to the comparison. The advancement of computational resources makes LES gain popularity in industrial applications. For this reason, and the additional information that it can carry, this numerical approach was also used.

Results demonstrate a combination of several behaviors of jets that are commonly found in different configurations. First of all, even though the present configuration was originally designed to keep the jets as straight as possible, they seem to slightly merge toward the center. This is a natural outcome especially in free jets, where the forces of reciprocal interaction initiate flapping, in case of two jets, or entrainment of the lateral jets into the central one, when three jets interact. In the present case, up to a distance from the plenum inlet of $x = 7D$, the four jets at the sides of the central one tend to merge, a conclusion derived from the displacement of the streamwise velocity peaks with respect to their centerlines. Downstream of this distance, the two lateral jets experience a greater attraction to the lateral walls that makes them stick to the surfaces while the remaining three still appear to merge. This effect can be interpreted as presence of the Coanda effect, a very noticeable phenomenon when single jets

expand near a wall. One last characteristic, also not unusual when jets interact, can be noticed in the present geometry when the central jet splits in two as it vertically expands. This effect, experimentally confirmed only in the case of the central jet, is noticeable starting at approximately $x = 7D$, as in the previous cases.

Numerical results show some limits on the predictino of the complex phenomena observed on the experimental data at $x = 4D$ and $x = 7D$. At this location, the interaction of the jets, limited in a confinement, causes recirculating vortexes between jets near the top and bottom walls which poses a strong challenge for the turbulence models. Out of all the models analyzed, we can conclude that there is a underestimation of the results of the streamwise mean velocity profiles U_x, with the linear eddy-viscosity $k\varepsilon$ models showing the largest diffusion. Results improve when the eddy-viscosity hypothesis for the evaluation of the Reynolds stress tensor is substituted with relative transport equations of the terms in the tensor, which is the case of the RSM model. This model, the only one that can represent the RMS streamwise fluctuations $U_{x\,RMS}$, even if it is not the more accurate found for the representation of the U_x profiles, shows good agreement with experimental results in terms of the turbulent fluctuations. Finally, the non linear models tested appear to be the most accurate of the models analyzed, especially the implementation with the damping function Damp E. The only URANS model that does not exhibit an underestimation of the velocity profiles is the $k\omega\ SST$, whose results appear to be less diffusive.

Even the LES exhibits a stronger diffusivity with respect to the experimental data. Like the URANS models, accuracy for the U_x profiles is higher in the regions close to the plenum inlet and far from it, which are considered the less significant in terms of the jets interaction. The profiles at $x = 7D$ still remain the worst predicted in terms of mean streamwise velocities. When turbulent fluctuations are compared with experimental measurements, there is a gradual decay of $U_{x\,RMS}$ from the profiles closer to the jets entrance, where good agreements are noticed, to the furthest profiles. Reasons of this global inaccuracy of the LES in predicting this flow field could be associated with the refinement of the cells in the plenum. Future studies include the use of the remap approach for inlet boundary conditions, that will reduce the number of cells used to generate a fully developed turbulent flow inside the pipes, and the numerical representation of a shorter plenum. These additional cells will then be redistributed in the plenum to increase the resolution in the critical regionso of the domain, such as where the shear layer is present.

One common consideration between URANS and LES lies in the lack of representation of two of the experimentally noticeable characteristics of interacting jets: merging and splitting. Only the Coanda effect seems to be predicted, with level of accuracy depending on the model considered.

In conclusion, the design details of the current geometry have been demonstrated to isolate fairly well the central jets, with the non linear numerical model being the most accurate in predicting their behavior. A further investigation on the same domain in order to better represent the flow structure will be performed with the Particle Image Velocimetry technique, which can visualize the entire flow field in a plane with respect to the punctual analysis of the LDV. An additional investigation with this latter technique, will be performed to evaluate the presence of eventual instabilities. Future variations in the configuration here studied include jet spacing and distance from the lateral walls, which may influence the attraction of the central jets and their detachment, respectively.

Nomenclature

Symbol	*Description*	*Unit [SI]*
κ	wavenumber	$[\mathrm{m}^{-1}]$
V	characteristic velocity of the flow	$[\mathrm{m\ s}^{-1}]$
L	characteristic length of the flow	[m]
l	characteristic size of turbulence eddies	[m]
u_l	characteristic velocity of turbulence eddies	$[\mathrm{m\ s}^{-1}]$
τ_l	characteristic timescale of turbulence eddies	[s]
l_0	large scale eddies size	[m]
u_0	large scale eddies velocity	$[\mathrm{m\ s}^{-1}]$
ν	kinematic viscosity	$[\mathrm{m}^2\mathrm{s}^{-1}]$
ε	Rate of dissipation of turbulent kinetic energy	$[\mathrm{m}^2\mathrm{s}^{-3}]$
η	small scale eddies size	[m]
u_η	small scale eddies velocity	$[\mathrm{m\ s}^{-1}]$
τ_η	small scale eddies timescale	[s]
Re	Reynolds number	$[-]$
u_i	*i*-th instantaneous velocity	$[\mathrm{m\ s}^{-1}]$
x_i	general Cartesian coordinate	[m]
ρ	density	$[\mathrm{kg\ m}^{-3}]$
p	static pressure	[Pa]
T_{ij}	viscous stress tensor	[Pa]
x	Cartesian coordinate vector	[m]
μ	dynamic viscosity	[Pa s]
u_τ	friction viscosity	$[\mathrm{m\ s}^{-1}]$
τ_w	wall shear stress	[Pa]
y^+	dimensionless wall distance	$[-]$
δ	boundary layer thickness	[m]
U_∞	free stream velocity	$[\mathrm{m\ s}^{-1}]$
U^+	dimensionless velocity	$[\mathrm{m\ s}^{-1}]$
a	generic random variable	$[-]$
A	mean value of the random variable	$[-]$
a'	fluctuation around the mean value	$[-]$
a_{RMS}	generic root means square variable	$[-]$

δ_{ij}	Kronecker delta	$[-]$
μ_t	turbulent/eddy viscosity	[Pa s]
k	turbulent kinetic energy	$[\mathrm{m^2\ s^{-2}}]$
ω	specific dissipation rate	$[\mathrm{s^{-1}}]$
S_{ij}	rate of strain	$[\mathrm{s^{-1}}]$
Ω_{ij}	rate of rotation	$[\mathrm{s^{-1}}]$
$\tilde{a}$	dimensionless properties	$[-]$
$\langle a \rangle$	averaging operator	$[-]$
$\bar{a}$	filtered properties	$[-]$
a^*	residual properties	$[-]$
τ_{ij}^R	residual stress tensor	[Pa]
ν_{SGS}	subgrid kinematic viscosity	$[\mathrm{m^2 s^{-1}}]$
l_{SGS}	characteristic subgrid length scale	[m]
u_{SGS}	characteristic subgrid velocity scale	$[\mathrm{m\ s^{-1}}]$
Δ	filtered width	[m]
λ	wavelength	[m]
δ_f	distance between fringes	[m]
θ	angle between laser beams	[°]
f_D	Doppler frequency	$[\mathrm{s^{-1}}]$
$\delta_x, \delta_y, \delta_x$	probe volume	[m]

Bibliography

[1] Szegö G.G., Dally B.B., Nathan G.J., *Operational characteristics of a parallel jet MILD combustion burner system,* Combustion and Flame, Vol.156 (2), pp. 429-438, 2009.

[2] Oriani L., Conway L.E. et al., *Overview of computational challenges in the development of evaluation models for safety analyses of the IRIS reactor.* Nuclear Mathematical and Computational Sciences: A century review, a century anew. Tennessee, IL, 2003.

[3] Hawley J.G., Veganas A., Brace C. J., *On-vehicle controllable cooling jets,* SEA 2004 World Congress & Exibition, Detroit, MI, USA, March 2004.

[4] Leboeful F., Sgarzi O., *The detail structure and behavior of discrete cooling jets in a turbine,* Annals of the New York Academy of Science, Vol. 934, pp. 95-109, 2001.

[5] Chung, Yongmann M., et al., *Unsteady heat transfer analysis of an impinging jets,* Journal of Heat Transfer, Vol.124, pp. 1039-1048, 2002.

[6] Hao L., Sonny H.W., Dilip A.S., *Velocity measurements whithin confined turbulent jets: Application to cardiovascular regurgitation.* Annals of Biomedical Engineering, Vol.25, pp. 939-948, 1997.

[7] Grimes R.Y., Burleson A., et al. *Quantification of cardiac jets: theory and limitations.* Echocardiography, Vol.11 (3), pp. 267-280, 1994.

[8] Yoganathan A.P., Cape E.G., Sung H.W., et al., *Review of hydrodynamic princeples for the cardiologist: applications to the study of blood flow and jets by imaging techniques*. JACC, vol.12, pp.1344-53, 1988.

[9] Blevins R.D., *Applied Fluid Dynamics Handbook*, Van Nostrand Reinhold Co., New York, 1984.

[10] Tanaka E., *The interference of two-dimensional parallel jets (1st report, experiments on dual jet),* Bull JSME Vol.13, pp.272-280, 1970.

[11] Bunderson E. N., Smith B. L., *Passive mixing control of plane parallel jets,* Experiments in Fluids, Vol.39, pp.66-74, 2005.

[12] Anderson E.A., Snyder D.O., Christensen J., *Experimental investigation of periodic behavior between parallel planar jets,* 40th AIAA aereospace science meeting and exhibition, Reno, Nevada 2002.

[13] Bunderson E. N., *Enhanced mixing of plane parallel jets,* Master's thesis, Utah State University, Utah.

[14] Lai J.C.S., Nasr A., *Two parallel plane jets: comparison of the performance of three turbulence models.* Proc Instn Mech Engrs, Vol.212, Part G.

[15] Tanaka E., *The interference of two-dimensional parallel jets (2nd report, experiments on dual jet).* Bull JSME Vol.13, pp.272-280, 1974.

[16] Tanaka E., *The interference of two-dimensional parallel jets (3rd report, the region near the nozzle in triple jets),* Bull JSME, Vol. 18, No. 124, 1975.

[17] Miozzi M., Lalli F., Romano G.P., *Experimental investigation of a free-surface turbulent jet with Coanda effect,* 15th Int Symp on Applications of Laser Techniques to Fluid Mechanics, Lisbon, 2010.

[18] Pope S. B., *An explanation of the turbulent Round-Jet/Plane-Jet anomaly*, AIAA Journal 16, 3, 1978.

[19] Smith E. J., Mi J, Nathan G. J., Dally B. B., *Preliminary examination of a "round jet initial condition anomaly" for the k-ε turbulence model,* 15th Australasian Fluid Mechanics Conference, Sydney, Australia, December 2004.

[20] Pellegrini M., Colombo E., Inzoli F., Dzodzo M., *Unsteady CFD analysis of parallel jet mixing as a support of the IRIS steam generator outlet design*, The 13th International Topical Meeting on Nuclear Reactor Thermal Hydraulics, Kanazawa City, Japan, 2009.

[21] Kunz R. F., D'Amico S. W., Vassallo P. F., Zaccaria M. A., Aksoy H., So R. M. C., *LDV measurement and Navier-Stokes computation of parallel jet mixing in a rectangular confinement*, 26th AIAA Fluid Dynamic Conference, San Diego CA, U.S.A., June 19-22, 1995.

[22] Mereu R., Colombo E., Inzoli F., Merzari E., Ninokata H., *Numerical study of parallel jet interaction*, ASME-ATI-UIT Conference on Thermal and Environmental Issues in Energy Systems, Sorrento, Italy, May 16-19, 2010.

[23] Cao Q., Lu D., Lv J., *Numerical investigation on temperature fluctuation of the parallel triple-jet*, The 8th International Topical Meeting on Nuclear Thermal-Hydraulics, Operation and Safety, Shanghai, China, October 10-14, 2010.

[24] Babu P. C., Mahesh K., *Upstream entrainment in numerical simulations of spatially evolving round jets*, Physics of Fluids, Vol.16, No.10, 2004.

[25] William K. George, *Lectures in Turbulence for the 21st Century*, Department of Applied Mechanics, Chalmers University of Technology, Gothenburg, Sweden.

[26] Pope S. B., *Turbulent Flows*, Cambridge University Press.

[27] Jensen K. D., *Flow measurements*, J. Of the Braz.Soc. of Mech. Sci. & Eng, Vol. 26, No. 4, pp. 400-417, 2004.

[28] Coghe A., *Laser Doppler and phase Doppler velocimetry*, Lecture notes, Politecnico di Milano.

[29] Dantec Measurement Technology, *BSA Installation & User's guide*.

[30] Wilcox D.C., *Turbulence modeling for CFD,* DCW Industries, Inc., La Canada, California, 1998.

[31] Launder B.E., Jones W. P., *The prediction of laminarization with two-equation model of turbulence,* Int. J. of Heat and Mass Transfer, Vol.15, pp. 301-314, 1972.

[32] Mereu R., *Non linear eddy viscosity RANS-based models in the framework of complex flows*, PhD dissertation, Politecnico di Milano, 2009.

[33] Schuman U., *Realizability of Reynolds stress turbulence models,* Physics of Fluids, Vol.20, pp. 721-725.

[34] Sagaut P., *Large Eddy Simulation for incompressible flows. An introduction*, 3rd Ed., Springer, 2009.

[35] Wagner C., Hüttl T. J., Friedrich R., *Low-Reynolds number effects derived from direct numerical simulations of turbulent pipe flow,* Computer & Fluids, Vol.30, pp. 581-590, 2001.

[36] J.M.J de Toonder, Nieuwstadt F.T.M., *Reynolds number effects in a turbulent pipe flow for low to moderate Re,* Phys. Fluids, Vol.9 (11), 1997.

[37] Roache P.J., *Quantification of uncertanty in computational fluid dynamics,*Annu. Rev. Fluid. Mech. Vol. 29, pp. 123/160, 1997.

[38] ANSYS Fluent, *"Fluent 12.1.2 Theory Guide"*, ANSYS Inc, 2009.

[39] Launder B. E., Spalding D.B., *Lectures in mathematical models of turbulence,* Academic press, London, England, 1972.

[40] Orszag S.A., Yakhot V. et al, *Renormalization group modelling and turbulence simulations.* In international conterence on near-wall turbulent flows, Tempe, Arizona, 1993.

[41] Shih T.H., Liou W.W. et al, *A new k-ε eddy-viscosity model for high Reynolds number turbulent flows – model development and validation*, Computers Fluids, Vol.23 (3), pp.227-238, 1995.

[42] Menter F.R., *Two-equation eddy-viscosity turbulence models for engineering applications*, AIAA Journal, Vol.32 (8), pp.1598-1605, 1994.

[43] Launder B.E., Reece G.J., Rodi W., *Progress in the developlent of a Reynolds-Stress turbulence closure*, J.Fluid Mech, Vol.68 (3), pp.537-566, 1975.

[44] Viaro S. Lampitella P., Mereu R., Colombo E., Inzoli F., *Large Eddy Simulation of a turbulent pipe flow: a sensitivity analysis on computational parameters,* XXX UIT Heat transfer conference, Italy, 2012.

[45] Deakin R. E., Kildea D.G., *A note on standard deviation and RMS,* The australian surveyor, Vol.44 (1), pp.74-79, 1999.

[46] Kechagioglou I., *Uncertainty and confidence in measurement, E.Σ.I. Πρακτικα 18ου Πανελληνιου Συνεδριον Στατιστικηζ*, σελ.441-449, 2005.

[47] Dubeif Y., Delcayre F., *On coherent-vortex identification in turbulence*, Journal of Turbulence, Vol.1 (11), pp.1-22, 2000.